THE UNIVERSITY *of* EDINBURGH

Multiphase Dynamics in Liquid Mixtures: Thermocapillary Propulsion of Bubbles and Instabilities in Evaporating Layers

Robson Kalata Nazareth

Thesis submitted for the degree of
Doctor *of* Philosophy
at
The University *of* Edinburgh

October, 2018

Declaration

I declare that this thesis was composed by myself, that the work contained therein is my own except where explicitly stated otherwise in the text and that this work has not been submitted for any other degree or processional qualification.

Robson Kalata Nazareth
Edinburgh, October 2018

To my family ...

Acknowledgements

I'd like to say thank you to my first supervisor Prashant Valluri for all the life long lessons that you thought me in the hard way. I also would like to say thank you to second supervisor Khellil Sefiane for sharing your wisdow with me. I also would like to say thank you to George Karapetsas and Pedro Sáenz for sharing your knowledge with me. I also would like to say thank you to Gustavo Rabello dos Anjos, Jungho Kim and Yasuyuki Takata for their whole hospitality and support during my secondments. Many thanks also to Sivasankaran Harish, Danié Orejon and Alexandros Askounis for all the discussions and for helping me with my experiments.

It was an inmense pleasure to have made so many good friends during these four years. Thanks Rohan, Adam, Arunn, Erich, Jamie, Steve, Pei, Abel, Hikaru, Patrick, James, Alessio, Dimitrious, Martin, Sofwan, Davide, Charles, Coinneach, Emmanuel, Adeel, Sofia, Nelly, Ares, Charithea, Ilka, Chiara, Mia, Dimitra, Erik, Rodrigo, Apoena, Ananda, Vicent, Alex, Hussain, Dam, Caleb, Yutaku, Zhang, Masahiro, Biao, Qin-Yi, Hideaki, Chen 冠廷, Tiago, Yuhong, Zhenying and Yoko.

Finally, I would like to thank my family especially my parents José and Ana, my sister Joseane and my brother Patricio for their constant support and encouragement and last but not least I'd like to thank my wife Graziela for her nurturing and enlightening powers.

Abstract

Liquid mixtures are ubiquitous in industry and in nature, and demonstrate remarkably more complex behaviour than pure fluids, which is still to be revealed. Particularly, commercial coolants are mixtures and the complexity in their flow behaviour is due to the interplay between phenomena driven by thermal and concentration gradients. This thesis considers predominantly binary mixtures wherein one component is more volatile than the other. The thesis focuses on multiphase dynamics presented in liquid mixtures. Given the volatility difference, there is always phase-change under temperature gradients. A bubble generated in that mixture has dynamics which will be subjected to the surrounding flow, temperature and concentration fields. The bubble will eventually grow until it occupies the entirety of the tube leaving behind a thin evaporating layer of the mixture. Thus the thesis work focusses on i) investigations of the bubble dynamics (during its slow growth phase) and ii) the instabilities in the evaporating layer (once the bubble occupies the whole cross section of the tube). The first part of this thesis investigates the counter/co-current thermocapillary propulsion of bubbles in the so-called self-rewetting liquids by means of direct numerical simulations (DNS) and validated by experiments. In self-rewetting liquids, surface tension presents a peculiar non-monotonic dependence on temperature. A DNS model based on the volume-of-fluid method is developed to study the dynamics of bubbles inside of a horizontal channel with constant flow rate and constant temperature gradient in the flow direction. A parametric study is performed

to investigate the influence of the viscous drag and thermocapillary forces on the bubble motion. Four distinct regimes of bubble migration are determined: counter-current propulsion, damped oscillations, sustained oscillations and co-current migration. A map is provided in the parameter space of Reynolds and capillary numbers showing these regimes. Each regime is discussed in detail and the mechanism that leads to sustained oscillations at low capillary numbers is discussed. The results are compared against the theoretical prediction for the bubble equilibrium position and frequency of the oscillations reported in the literature. Next, experiments are performed to investigate the thermocapillary migration of bubbles in self-rewetting liquids inside of a horizontal circular channel with constant flow rate and constant temperature gradient in the flow direction. The motion of the bubbles is recorded with a CCD camera from the top while the temperature at the channel wall is recorded with an IR-camera from the side. The influence of the flow rate and the temperature gradient on the bubble motion is investigated. It has been observed that the flow rate has a decreasing linear relationship with the bubble velocity while the temperature gradient has an increasing linear relationship with the bubble velocity during the counter-current motion. The experiments validate the numerical findings and these are presented in the flow-regime map. The third part of this thesis is devoted to the study of the stability of the evaporation of a horizontal thin liquid layer which consists of a binary mixture of volatile liquids heated from below by means of linear stability analysis and transient numerical simulations. The effect of vapour recoil, thermo- and solute-capillarity and the van der Waals interactions are considered. The long-wave approximation is used to derive the evolution equations for the free interface and the concentration of the components. A linear stability analysis is performed to derive the growth rate of the instabilities for the case of quasi-equilibrium evaporation and non-equilibrium evaporation. The developed linear theory describes two modes of instabilities: i) a monotonic instability

mode where the perturbations simply grow until the liquid layer is ruptured if the thermo-capillary and the solute-capillary force enhance each other and ii) an oscillatory instability mode where perturbations oscillate if the thermo-capillary and the soluto-capillary forces compete with each other. A parametric study is performed to investigate how these modes depend on the ratio between the thermal and solutal Marangoni numbers and on the volatility ratio of the components. The mechanisms of the instabilities are discussed in detail. The linear theory is validated against transient simulations and show a good agreement in the comparison of the growth rates. Lastly, the evolution of the interface for the two instability modes is analysed by means of transient simulations.

Contents

Acknowledgements **V**

Abstract **VII**

Contents **XI**

Nomenclature **XV**

List of Figures **XXIII**

List of Tables **XXIX**

1 Introduction **1**

1.1 Organization of this Thesis 4

2 Literature Review **7**

2.1 Thermocapillary Migration 7

2.1.1 Experiments 7

2.1.2 Theoretical approaches 9

2.1.3 Numerical modelling 9

2.1.4 Self-rewetting fluids 11

2.2 Instabilities in Liquid Layers 13

2.2.1 Heating without phase-change 13

2.2.2 Effect of long-range molecular forces 15

2.2.3 Effect of phase-change 16

2.2.4 Non-equilibrium effects 17
2.2.5 Surfactant laden Layers 17

3 Numerical investigation of thermocapillary propulsion of bubbles in self-rewetting liquids 19

3.1 Mathematical modelling 20
3.1.1 Problem statement 20
3.1.2 Scaling 21
3.1.3 Governing equations 22
3.1.4 Boundary and initial conditions 23
3.1.5 Numerical method 24
3.1.6 Tangential component of surface tension and validation . . 25
3.2 Theoretical prediction 27
3.3 Results and Discussion 28
3.3.1 Regime map 30
3.3.2 Flow regimes 32
3.3.3 Transition regions 34
3.3.4 Equilibrium position 37
3.3.5 Sustained oscillations 38
3.4 Conclusion 39

4 Experiments on thermocapillary propulsion of bubbles in self-rewetting liquids 41

4.1 Experimental Set-up 42
4.2 Results 45
4.2.1 Typical thermocapillary propulsion 45
4.2.2 Effect of temperature gradient 50
4.2.3 Effect of flow rate 52
4.3 Conclusions 53

5 Evaporation of liquid layers comprising binary mixtures 55

5.1 Problem formulation 56

5.2 Scaling 60

5.3 Base state 63

5.4 Long-wave approach 67

5.5 Linear stability analysis 71

5.5.1 Quasi-equilibrium evaporation ($K = 0$) 71

5.5.2 Non-equilibrium evaporation ($K \neq 0$) 74

5.5.3 Mechanisms of the instability 77

5.5.4 Parametric analysis 79

5.6 Linear regime: validation with numerics 84

5.7 Non-linear regime: analysis and numerical results 86

5.8 Conclusions 90

6 Conclusions and Future Work 93

6.1 Conclusions 93

6.2 Future Work 95

A Linear stability analysis 97

B Weak formulation 99

Bibliography 101

Nomenclature

Ca Capillary number

DNS Direct Numerical Simulations

FDM Finete Difference Method

FEM Finite Element Method

M_T Thermal Marangoni number

M_c Solutal Marangoni number

Ma Marangoni number

Pe Peclet number

Pr Prandtl number

Re Reynolds number

VOF Volume of Fluid

Chapter 3

A_r Bubble aspect ratio

B Dimensionless temperature gradient

$\tilde{D}$ Diameter of the tube

$\tilde{H}$ Radius of the tube

$\tilde{L}$ Length of the tube

$\tilde{R}_o$ Initial radius of the bubble

$\tilde{T}$ Temperature field

T_{in} Inlet temperature

$\tilde{T}_o$ Surface tension minimum temperature

$\tilde{U}_o$ Reference vecolity

c Volume fraction of the liquid phase

c_p Arithmetic average of specific heat capacity

$\tilde{c}_{pg}$ Specific heat capacity of the gas phase

$\tilde{c}_{pl}$ Specific heat capacity of the liquid phase

c_{pr} Specific heat capacity ratio

k Arithmetic average of thermal conductivity

$\tilde{k}_g$ Thermal conductivity of the gas phase

$\tilde{k}_l$ Thermal conductivity of the liquid phase

k_r Thermal conductivity ratio

$\hat{\mathbf{n}}$ Unit vector normal to the interface

$\tilde{p}$ Pressure field

$\tilde{r}$ Radial coordinate

$\tilde{t}$ Time

$\tilde{u}$ Longitudinal velocity

u_b Bubble velocity

$\tilde{u}_f$ Average flow velocity

$\tilde{v}$ Radial velocity

$\tilde{z}$ Longitudinal coordinate

z_b Bubble position

$\tilde{z}_e$ Bubble equilibrium position

$\tilde{z}_o$ Surface tension minimum position

Δ Smallest mesh size

$\Delta\tilde{T}$ Difference between inlet temperature and the surface tension minimum temperature

$\tilde{\beta}$ temperature gradient

δ Dirac delta

$\tilde{\kappa}$ Interface curvature

μ Arithmetic average of dynamic viscosity

$\tilde{\mu}_g$ Dynamic viscosity of the gas phase

$\tilde{\mu}_l$ Dynamic viscosity of the liquid phase

μ_r Viscosity ratio

∇ Gradient operator

∇_s Gradient operator tangent to the interface

ρ Arithmetic average of density

$\tilde{\rho}_g$ Density of the gas phase

$\tilde{\rho}_l$ Density of the liquid phase

ρ_r Density ratio

$\tilde{\sigma}$ Surface tension

$\tilde{\gamma}$ Second order temperature coefficient of surface tension

σ_{ref} Dimensionless reference surface tension

A Amplitude of the monotonic instability

A Hamaker constant

$\mathcal{A}$ Non-dimensional parameter related to the Hamaker constant

Chapter 5

A_{max} Maximum amplitude of the oscillations of the oscillatory instability

D Ratio of vapour to liquid densities

$\tilde{D}_i$ Diffusion coefficient of component $i = A,\ B$

E Evaporation rate

$2\tilde{H}$ Mean curvature of the interface

$\tilde{H}_o$ Initial thickness of the liquid layer

$\tilde{J}$ Total evaporative flux

$\tilde{J}_i$ Evaporative flux of component $i = A,\ B$

K Measure of the degree of non-equilibrium

$\mathcal{L}$ Measure of the latent head of component A

$\tilde{L}_o$ Width of the liquid layer

$\tilde{L}_{v,i}$ Specific internal latent heat of vaporization of component $i = A,\ B$

M_i Molecular weight of component $i = A,\ B$

R_g Universal gas constant

$\tilde{T}$ Temperature of the liquid phase

$\tilde{T}_g$ Equilibrium vapour temperature

$\tilde{T}_g$ Temperature of the vapour phase

$\tilde{T}_v$ Temperature of the vapour phase

$\tilde{T}_w$ Temperature of the heated solid substrate

$\tilde{c}$ Concentration of the component A

$\tilde{c}_p$ Specific heat capacity of the liquid phase

$\tilde{h}$ Height of the liquid layer

k Wave number

k_M Most unstable wave number

$\mathbf{n}$ Outward unit normal vector on the interface

$\tilde{p}$ Pressure field of the liquid phase

$\tilde{p}_i^o$ Vapour pressure of component $i = A,\ B$

$\tilde{p}_{v,i}$ Partial vapour pressure of component $i = A,\ B$

r Growth rate

r_{mon} Growth rate of the monotonic instability

r_{osc} Growth rate of the oscillatory instability

$\mathbf{t}$	Unit tangential vector on the interface
$\tilde{\mathbf{u}}$	Velocity field of the liquid phase
$\tilde{u}$	x-component of the velocity field
$\tilde{u}_s$	Velocity of the interface
$\tilde{u}_\tau$	Tangential component of the velocity
$\tilde{u}_v$	Velocity field of the vapour phase
$\tilde{w}$	z-component of the velocity field
$\tilde{x}$	x-coordinate of the Cartesian system
$\tilde{z}$	z-coordinate of the Cartesian system
Γ	Ratio of the temperature coefficient of surface tension
Γ_i	Non-dimensional temperature coefficient of surface tension of component $i = A,\ B$
Λ	Latent heat ratio
$\tilde{\Pi}$	Disjoining pressure
α	Volatility ratio
β	Molar ratio
δ	Ratio of the reference surface tension
ε	Ratio between the thickness and the width of the liquid layer
$\tilde{\gamma}_i$	Temperature coeficient of surface tension of component $i = A,\ B$
$\tilde{\kappa}_A$	Thermal diffusivity of component A
$\tilde{\lambda}$	Thermal conductivity of the liquid phase

λ_r Thermal conductivity ratio

$\tilde{\lambda}_v$ Thermal conductivity of the vapour phase

$\tilde{\mu}$ Dynamic Viscosity of the liquid phase

μ Dynamic Viscosity ratio

$\tilde{\nu}_A$ Kinematic viscosity of component A

$\tilde{\rho}$ Density of the liquid phase

$\tilde{\rho}_v$ Density of the vapour phase

$\tilde{\sigma}$ Surface tension of the mixture

$\tilde{\sigma}_i$ Surface tension of component $i = A,\ B$

$\tilde{\sigma}_{i,o}$ Reference surface tension of component $i = A,\ B$

$\underline{\underline{\tilde{T}}}$ Stress tensor

List of Figures

1.1 a) Chapters 3 and 4: counter-current propulsion and migration of small bubbles in early stages (in this regime, phase change is ignored), studied via Direct Numerical Simulations and experiments. b) Chapter 5: Bubble has grown to occupy most of the tube (late stages) due to phase change. Instabilities in evaporating binary fluid layer are studied via stability analysis and transient simulations. 3

2.1 Schematic of the Young's experimental apparatus. This figure has been obtained from Young *et al.* [1]. 8

2.2 Schematic representation of Shanahan & Sefiane's experiment showing the variation of surface tension along the channel. This figure has been obtained from Shanahan & Sefiane [2]. 13

3.1 Schematic of the mathematical model and, on top, the surface tension coefficient related to the temperature along the channel wall. 21

3.2 The temperature field at the moment that the bubble is introduced. The red line corresponds to the temperature referring to the surface tension minimum and the black circle is the interface of the bubble. . . 24

3.3 The variation of surface tension through the channel for a strong temperature gradient $B = 0.1$ and $\sigma_r = 5.732$. 25

3.4 Schematic of the domain for the 2D problem used for the validation. . 26

3.5 Validation of the numerical model. a) Comparison against the results presented in Ma & Bothe [3] for the set of parameters $Re = Ma = 0.72$ and $Ca = 0.0576$ and a domains size of $L = H = 4R$. b) Comparison against the results presented in Nas & Tryggvason [4] for the set of parameters $Re = 5$, $Ma = 20$ and $Ca = 0.01666$ and domains size of $L = 8R$ and $H = 4R$. 27

3.6 Time evolution of (a) the center of mass z_b and (b) velocity u_b of the bubble for the set of base parameters with $Re = 16$ and $Ca = 1.15 \times 10^{-2}$. At the right the panels showing the bubble motion with the streamlines (black lines), the bubble interface (blue line) and the isothermal line for $T = 1$ corresponding to the minimum in surface tension (red line). 30

3.7 Map with the four bubble behaviours in the $Re\ vs\ Ca$ parameters space. Region (i) is the counter-current propulsion, region (ii) the damped oscillations, region (iii) the sustained oscillations, and region (iv) the co-current migration. 31

3.8 Time evolution of (a,b) the center of mass, z_b, and (c,d) the aspect ratio of the bubble for different capillary numbers with $Re = 8$ (left) and $Re = 800$ (right). 33

3.9 Time evolution of the bubble center of mass, z_b, showing the transition from region (I) to region (II) increasing the Reynolds number for $Ca = 5.73 \times 10^{-3}$. 34

3.10 Time evolution of the bubble center of mass, z_b, and the aspect ratio A_r at the equilibrium position, showing the transition to region (IV) increasing the capillary number for (a) $Re = 8$ and (b) $Re = 800$. . . . 35

3.11 Time evolution of the bubble center of mass, z_b, showing the transition to region (III) decreasing the capillary number for (a) $Re = 8$ and (b) $Re = 800$. 35

3.12 The vector field and the isothermal line corresponding to the surface tension minimum showing the transition to sustained oscillations for $Re = 8$. (a) and (b) are stable equilibrium positions showing how z_e moves in direction to the surface tension minima by decreasing Ca and (c) and (d) are the right most (top) and the left most (bottom) position during the oscillation around z_e that arise and increase their amplitude by decreasing Ca. 36

3.13 Comparison between the numerical bubble equilibrium position for $Re = 8$ and $Re = 800$, and the theoretical prediction. 37

3.14 Bubble shape at the equilibrium position for different values of Re and $Ca = 5.73 \times 10^{-2}$. 37

3.15 (a) Frequency and (b) amplitude of the oscillations in function of the Reynolds number for $Ca = 5.73 \times 10^{-4}$. 38

4.1 Schematic diagram of the test section. 43

4.2 The experimental apparatus designed to analyse the motion of bubbles inside a heated circular channel with constant flow rate. 44

4.3 Sequence of images taken at every 5 s showing the motion of a bubble with initial diameter of 0.25 mm through a heated circular channel with constant flow rate, $Q = 1.5\ ml/min$, from left to right and constant temperature gradient, $\beta = 1.15\ K/mm$ ($\Delta T = 46\ ^oC$), in the same direction. On top it is shown the temperature along the channel wall taken by the IR-camera before the injection of the bubble. 47

4.4 Time evolution of the bubble position (left) and temperature along the wall (right) for different flow rates and temperature gradients, where D_b/D_{CH} is the ratio between the bubble diameter and channel diameter and ΔT is the temperature difference between the inlet and outlet. The experimental error in the position is $\pm 0.02\ mm$ and in the temperature is $\pm 1\ ^oC$. 49

4.5 Experimental points for different flow rates and temperature gradients on the map generated via simulations with the different regimes of bubble motion: counter-current propulsion (balck), damped oscillations (blue), sustained oscillations (red), and co-current migration (gray). . . 50

4.6 Bubble average velocity, v_b as a function of the temperature gradient, β, for $Q = 1\ ml/min$ ($v_f = 1.3\ mm/s$) and $Q = 1.5\ ml/min$ ($v_f = 2\ mm/s$), where v_f is the average flow velocity. 51

4.7 Bubble average velocity, v_b, as a function of the flow rate (average flow velocity, v_f) for two temperature gradients, $\beta = 0.75k/mm$ and $\beta = 1K/mm$. 52

5.1 Schematic of the physical system describing an evaporating thin liquid film on top of a horizontal heated solid substrate in a periodic domain. 56

5.2 Time evolution of a) the height of the flat interface, b) the evaporative flux of components A and B, and c) the temperature difference between the solid substrate and the interface of the liquid layer, for $K = 0$ and $K \neq 0$. 67

5.3 Behaviour of growth rates r_+ and r_- versus the wavenumber k, for $K = 0$, with a) $E = 0$ and b) $E = 10^{-5}$. Other parameters are the set of base parameters given in Table 5.2. 75

5.4 Behaviour of growth rates r_+ and r_- versus the wavenumber k, for $K \neq 0$, with a) $E = 0$ and b) $E = 10^{-5}$. Other parameters are the set of base parameters given in Table 5.2. 78

5.5 a) Schematic of the oscillatory instability for the case where component A is less volatile than B and has higher surface tension. b) Schematic of the monotonic instability for the case where component A is more volatile than B and has higher surface tension. 78

5.6 Growth rates r_+ and r_- versus the wavenumber k for $K \neq 0$. Oscillatory instability mode for a) $M_T = 10$ and b) $M_T = 100$. Monotonic instability mode for c) $M_T = 1000$. 79

5.7 Growth rates r_+ and r_- versus the wavenumber k for $K \neq 0$. Monotonic instability mode for a) $M_c = 10$. Oscillatory instability mode for b) $M_c = 100$ and c) $M_c = 1000$. 80

5.8 Growth rates r_+ and r_- versus the wavenumber k for $K \neq 0$. Monotonic instability mode for a) $\alpha = 0.5$. Oscillatory instability mode for b) $\alpha = 1$ and c) $\alpha = 2$. 81

5.9 Regions of the map with respect to the volatility ratio and surface tension ratio in the parameter space of α versus M_c/M_T. 82

5.10 Map showing the regions of monotonic instability mode (crosses) and oscillatory instability mode (bullets) in the parameter space of α versus M_c/M_T for a) $E = 10^{-4}$, b) $E = 10^{-5}$ and c) $E = 10^{-6}$. 82

5.11 Map showing the regions of monotonic instability mode (crosses) and oscillatory instability mode (bullets) in the parameter space of α versus M_c/M_T for a) $\Lambda = 0.1$, b) $\Lambda = 1$ and c) $\Lambda = 2$. 83

5.12 a) Growth rate versus the wavenumber derived from the linear stability analysis for the case of monotonic instability mode with $\alpha = 0.5$. b) Growth rate of the amplitude of the initial perturbation over time derived from the transient simulation. 85

5.13 a) Growth rate versus the wavenumber derived from the linear stability analysis for the case of oscillatory instability mode with $\alpha = 2.28$. b) Growth rate of the maximum amplitude of the oscillations over time derived from the transient simulation. 85

5.14 Time evolution of the interface for $\alpha = 0.5$ showing the monotonic instability mode. 87

5.15 Time evolution of the interface for the parameters in Table 5.2 showing the oscillatory instability mode. 88

5.16 Time evolution of the interface for the parameters in Table 5.2 showing the oscillatory instability mode. 88

5.17 Modes of the Fourier transform of a) the interface ($s_1 = 2.21e-4$, $s_2 = 7.20e-4$, $s_3 = 9.92e-4$), b) the temperature ($s_1 = 2.44e-4$, $s_2 = 7.36e-4$, $s_3 = 1.04e-3$) and c) the concentration ($s_1 = 2.57e-4$, $s_2 = 7.40e-4$, $s_3 = 1.07e-3$). d) First mode of the Fourier transform of the interface (H), temperature (T) and concentration (C). 89

List of Tables

3.1 Properties for 5 wt.% butanol/water mixture at 70 ^oC. 21

4.1 Uncertainty of the equipments. 44

4.2 Experimental conditions. 46

5.1 Properties for water and ethanol at 80 ^oC. 62

5.2 Dimensionless quantities for a 50% water/ethanol mixture. 63

Chapter 1

Introduction

Liquid mixtures are ubiquitous in industry and in nature, and demonstrate remarkably more complex behaviour than pure fluids. The complexity in their flow behaviour is due to the interplay between phenomena driven by thermal and concentration gradients. Essentially, variations in temperature and concentration lead to surface tension gradients that can drive bubble motion and cause instabilities in liquid films. These phenomena are investigated in this thesis.

The variation in surface tension along a liquid-gas interface due to variations in temperature and/or concentration is know as Marangoni effect [5]. Surface tension gradients induce shear stresses along the interface that result in fluid motion from low to high surface tension regions. When the surface tension gradients are due to temperature this phenomena is refereed to as thermal Marangoni effect or as thermocapillary effect, and when it is due to concentration it is refereed to as solutal Marangoni effect or as solutocapillary effect.

The thermocapillary effect is particularly important on the motion of bubbles inside liquids subject to temperature gradients. Any mixture flowing in a microchannel or a microtube when subjected to heating or temperature gradients, at early times, will experience phase-change resulting in formation of bubbles. For instance, in evaporative cooling micro-devices the evaporation of liquid will generate bubbles that will be driven by the temperature profile of the heated device

[6]. Therefore, understand the dynamics of bubble under temperature gradients is crucial for the operation of these devices in order to prevent counter-flow motion and trapping of bubbles that can compromise the operation of these devices leading to dry-out and consequently overheating. These bubbles can migrate in the fluid (FIG. 1.1a) due to thermal or concentration gradients, the so-called thermo-soluto-capillary effect. The first aspect this thesis considers is the migratory or counter-current propulsive behaviour of bubble motion submerged in a binary liquid mixture. Full two-phase direct numerical simulations (DNS) are performed, that are validated against rigorous experiments. The simulations (validated by experiments) reveal a full spectrum of bubble motion as a function of flowrates and temperature gradients.

Under prolonged phase change, at late times, the bubble grows large enough to occupy the entire micropipe - such that there is a residual thin layer of the binary liquid mixture around the bubble (FIG. 1.1b). The second aspect this thesis considers are the instabilities in evaporation liquid layers formed of this binary mixture. Linear stability analysis is performed to reveal behaviour in the linear regime and transient simulations to reveal non-linear behaviour during later times. Therefore, a full temporal stability analysis is performed on evaporating binary liquid mixtures.

For most liquids surface tension has a linearly decreasing relation with temperature and in this case, the thermocapillary effect drives the liquid around the bubbles in direction to cold temperatures while the bubble is propelled towards hot temperatures. However, a remarkably different behaviour happens in a specific type of binary mixtures composite of aqueous solutions of high-carbon alcohols, called ‘self-rewetting’ fluids, where surface tension has a parabolic dependence on temperature [7]. In this case, the bubbles are propelled towards the surface tension minimum and can be trapped around this minimum. If the bubbles are at low temperature regions where surface tension has a negative slope they are

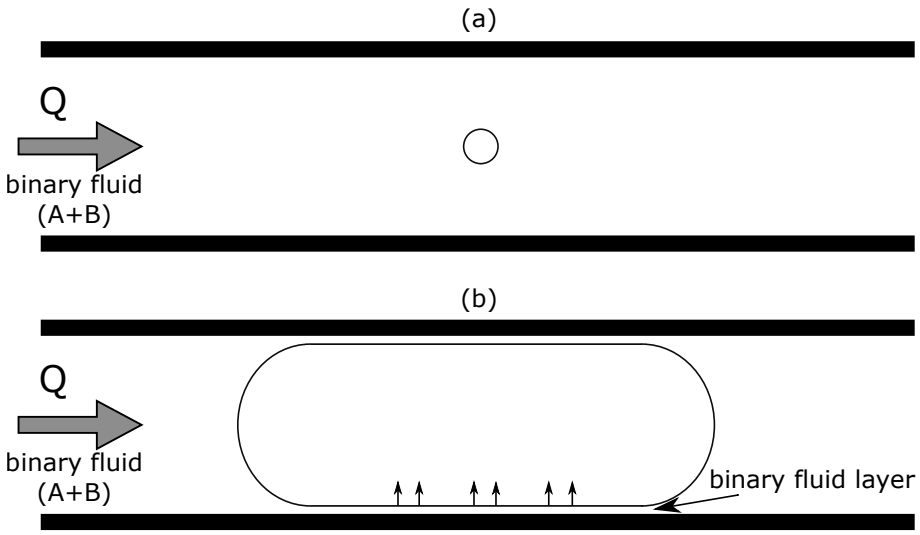

Figure 1.1: a) Chapters 3 and 4: counter-current propulsion and migration of small bubbles in early stages (in this regime, phase change is ignored), studied via Direct Numerical Simulations and experiments. b) Chapter 5: Bubble has grown to occupy most of the tube (late stages) due to phase change. Instabilities in evaporating binary fluid layer are studied via stability analysis and transient simulations.

propelled towards hot temperatures, while if the bubbles are at high temperature regions where surface tension has a positive slope they are propelled towards cold temperatures. The first part of this thesis (Chapters 3 and 4) considers binary mixtures with a parabolic dependence of surface tension on temperature, while the second part of this thesis (Chapter 5) considers binary mixtures with a linearly decreasing dependence of surface tension on temperature.

The solutocapillary effect plays an important role on liquid mixtures composite of components with different volatilities. The uneven evaporation of the components induces concentration variations resulting in surface tension gradients. The interplay between the thermocapillary and the solutocapillary effect can lead to different modes of instability in liquid layers. When the thermocapillary and solutocapillary effects enhance each other, a monotonic instability mode, where the perturbations at the interface simply grow until the liquid layer is ruptured, is observed. Whereas when the thermocapillary and solutocapillary effects compete with each other, an oscillatory instability mode is observed where the perturbations at the interface oscillate growing in amplitude. Thin film flows

have a variety of engineering applications including coating flows [8], paint layers [9] microfluidics [10, 11], and biophysical applications such as lung airways and linings [12], and tear-film flows [13].

This thesis presents a direct numerical simulation (DNS) model to study the thermocapillary propulsion of bubbles using a self-rewetting liquid within a tube with constant flow rate and constant temperature gradient. This study reveals for the first time, distinct bubble regimes under the range of the parameters investigated. The transition between these regimes is investigated and a mechanism for the sustained oscillations observed experimentally [2] is discussed. Experiments on the thermocapillary propulsion of non-confined bubbles in self-rewetting liquids are performed to support the numerical findings. Finally, linear stability analysis and transient simulations are performed in thin liquid layers comprising binary mixtures with linearly decreasing dependence of surface tension on temperature and the main mechanisms of the instabilities modes found are discussed.

1.1 Organization of this Thesis

The remainder of this thesis is organised as follows. An overview of the most relevant works for the subject of this investigation is presented in Chapter 2. This chapter is divided in two sections according to the physical phenomena investigated in subsequent chapters, namely thermocapillary migration of bubbles and instabilities in liquid layers. Chapter 3 presents a numerical investigation of the thermocapillary migration in self-rewetting liquids. A two-phase direct numerical simulations model is presented and the dynamics of bubbles is investigated for a wide range of flowrates and temperature gradients. Chapter 4 presents experimental work on thermocapillary migration of bubbles in self-rewetting liquids including validation of the numerical simulations in Chapter 3. The influence of the temperature gradient and the flow rate inside the channel is discussed. Chapter 5 is devoted to the investigation of instabilities in thin liquid layers comprising

binary mixtures of components with different volatilities and a linearly decreasing dependence of surface tension on temperature. A system of evolution equations is derived employing the long-wave approximation and a linear stability analysis is performed. A parametric study is performed to investigate the growth rate and type of the instabilities and the evolution of the interface during the evaporation process is analysed by means of transient simulations. Lastly, conclusions and future work are presented in Chapter 6.

Chapter 2

Literature Review

2.1 Thermocapillary Migration

The flow driven by variable surface tension along the liquid-gas interface in multi-phase systems is a mechanism of great importance to many industrial, biological and everyday applications. Non-uniformities in surface tension create stresses at the interface that may induce fluid motion on the surround fluid by viscous forces. This phenomena known as the Marangoni effect, can be induced either by temperature gradients, concentration gradients or both. The thermo/soluto-capillary effect is particularly important for the motion of bubbles and drops, because the fluid motion induced by the variation of surface tension along the interface may be exploited to propel bubbles and drops in the opposite direction to the surface tension gradient. In the past decades a variety of theoretical and experimental investigations have addressed this phenomenon; many of the fundamental aspects of this field has been summarized by Subramanian *et al.* [14].

2.1.1 Experiments

In a seminal paper, Young [1] demonstrated that the motion of bubbles in pure liquids can be controlled by a thermal gradient. Applying a negative vertical

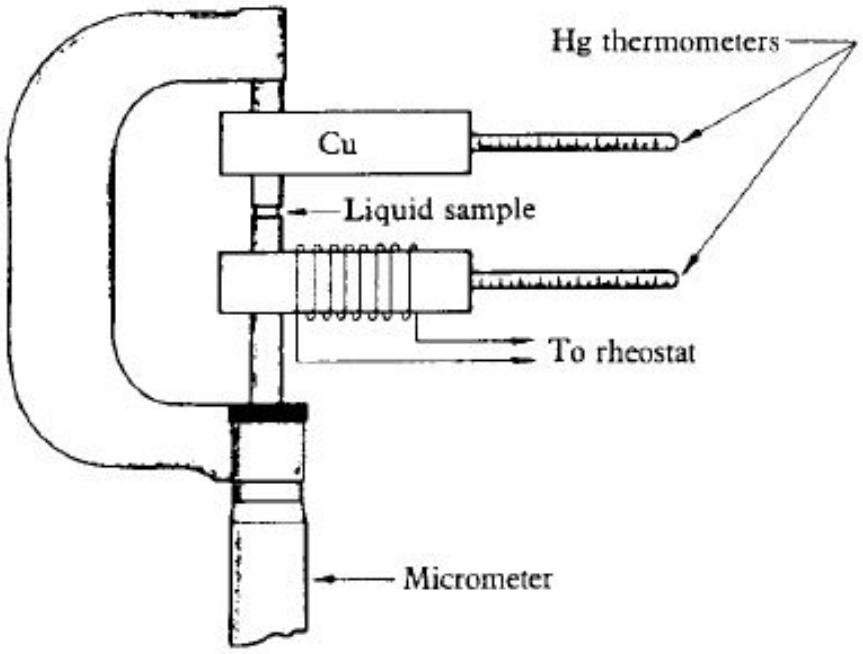

Figure 2.1: Schematic of the Young's experimental apparatus. This figure has been obtained from Young *et al.* [1].

temperature gradient in a viscous fluid, the authors showed that the buoyancy forces acting on an air bubble can be balanced by the thermocapillary forces. The bubble can thus be trapped within the bulk fluid, or even overcome the effect of gravity and move downwards. A schematic of the experimental apparatus used by Young is presented in FIG. 2.1. Young [1] also derived an analytical expression for the terminal velocity of a non-deformable spherical bubble in an ambient fluid under a vertical temperature gradient, for the limit of zero Reynolds (Re) and Marangoni (Ma) numbers, i.e. negligible inertia and thermal convection.

Many experimental studies have addressed this phenomenon in reduced gravity environments using rectangular test cells and maintaining different steady temperatures on the opposite walls of the cell along the long axis [15, 16, 17, 18, 19, 20, 21] as well as in normal gravity, using matched densities [22, 23, 24] and other techniques to reduce the effects of buoyancy [25]. In the above works, the fluid considered presents surface tension as a linearly decreasing function of temperature. In this thesis, we consider a carrier fluid that presents a surface

tension as a parabolic function of temperature. Also, we focus on experiments with thermocapillary propulsion of a single small bubble ($D_b \approx 0.2\ mm$) against flow in a tube ($D = 4\ mm$) under a temperature gradient. We focus on small bubbles to minimise the effect of buoyancy.

2.1.2 Theoretical approaches

Motivated by novel microgravity applications, a series of works [26, 27, 28, 29, 30, 31] extended Young's analysis to investigate the effects of thermal convection under the assumption of negligible buoyancy. Subramanian [26, 27] used the method of matched asymptotic expansions for solving the governing equations for small Ma and concluded that thermal convection may act to reduce the terminal bubble velocity. Balasubramaniam & Chai [28] extended the applicability of previous works showing that for small Ma the derived terminal velocity is an exact solution of the Navier-Stokes equation for arbitrary Re. Shankar & Subramanian [29] extended the limit of small Ma using improved series from the Euler transformation and showed that the scaled bubble velocity decrease with increasing Ma. Balasubramaniam & Subramanian [30, 31] investigated the effect of large Ma in the bubble migration velocity. The authors concluded that, in the limit of both small and large Re, the bubble terminal velocity reaches an asymptotic limit for large Ma.

2.1.3 Numerical modelling

On the numerical side, some authors have focused on studying the effects of thermal convection on the thermocapillary bubble migration under the assumption of non-deformable interface. Szymczyk & Siekmann [32] investigated by means of a finite difference method (FDM) the effect of energy convection for small Ma in the limit of creeping flow confirming the analytical results obtained by Subramanian and the classical solution by Young [1]. For large Ma with non-zero Re

the authors showed that for constant Prandtl (Pr) number the bubble speed can be represented as a function of Re. Shankar & Subramanian [29] investigated small ($Ma < 20$) and large ($20 < Ma < 200$) Marangoni numbers using FDM and showed that the scaled bubble velocity decreases with Ma and approaches an asymptotic value for large Ma. Balasubramaniam & Lavery [33] investigated the thermocapillary migration for a large range of Re ($10^{-7} < Re < 2000$) and Ma ($10^{-7} < Re < 1000$) and concluded that the bubble velocity is more influenced by Ma than Re. Ma *et al.* [34] investigated the convective transport inside a drop and, unlike previous results, they found that the terminal drop velocity initially decreases as Ma increases from zero, then attains a minimum, and finally increases with Ma when it is large.

Numerical studies considering other numerical strategies are also available in the literature. Haj-Hariri *et al.* [35] performed three-dimensional simulations using the level-set method to investigate the effects of shape deformations, momentum and energy convection during the thermocapillary migration. The authors found that the drop motion is slowed down by energy convection and shape deformations. Nas & Tryggvason [4] and Nas *et al.* [36] investigated the effect of Re and Ma on the interaction of multiple deformable bubbles/drops using front-tracking and FDM for two- and three-dimensional simulations. The authors found that bubbles and light drops line up perpendicular to the temperature gradient, while spacing themselves evenly across the channel. Yin *et al.* [37] investigated the effect of Re and Ma, and the density and specific heat ratios on spherical and non-deformable drops using an axisymmetric model with finite-difference front-tracking scheme. The authors found that fairly large Ma may lead to fluctuation in drop velocities before reachup the terminal velocity. Ma & Bothe [3] investigated the thermocapillary migration using the Volume of Fluid (VOF) method for high convective heat transfer covering a wide range of Ma ($Ma \leq 5000$) and achieved a good agreement with experimental data in the

regime of high convective heat transport. In the above models, the effect of confinement and flow on the thermocapillary migration has not been studied. This thesis focuses on numerically modelling propulsion of a single bubble in a tube of circular cross-section subject to temperature gradient. The size of bubble and the tube correspond to the experiments presented in the thesis. Bubble migratory/propulsion behaviour is analysed over a range of flow rates ($0.1 < Re < 10^4$) and temperature gradients ($10^{-5} < Ca < 10^{-1}$). A VOF approach using Basilisk [38] is employed for this purpose and axisymmetry is assumed.

2.1.4 Self-rewetting fluids

All the above approaches, however, have been concerned with liquids characterized by a linearly decreasing dependence of surface tension on temperature. Little analytical and numerical attention has been given to liquids whose surface tension evolves non-linearly with temperature; these are the so-called self-rewetting liquids. Abe *et al.* [7] coined this term to describe liquids with the ability to move towards hotter surfaces driven by the positive surface tension gradient. Mostly composed of non-azeotropic diluted aqueous solutions of high-carbon alcohols, these liquids are characterized by a *parabolic* dependence of surface tension on temperature with a well defined minimum, which leads to a positive surface tension gradient for a range of high temperatures [39] in contrast with the negative gradient found in common liquids.

The anomalous positive surface-tension gradient of self-rewetting liquids has caught the attention of scientists for heat transfer applications. Experiments have been carried to investigate critical heat flux in pool boiling [40, 41], heat transfer enhancement in heat pipes systems [42, 43], micro-oscillating heat pipes [44] and subcooled pool boiling [45]. In parallel, Vochten *et al.* [46] and Vochten & Petre [47] performed a thermodynamic study on the heat of reversible adsorption with self-rewetting liquids. More recently, droplet spreading driven by thermo-

capillarity using self-rewetting liquids was studied by Karapetsas *et al.* [48] by means of lubrication theory and a finite element method (FEM). The authors showed that when the surface tension minimum is located within the droplet, the thermocapillary stresses lead to rapid spreading. In addition, the rising bubble problem using self-rewetting liquids was investigated by Tripathi *et al.* [49] using a VOF model for a range of Bond and Galileo numbers, and different steepness of surface tension function. They demonstrated that the bubble motion can be reversed and then held stationary. In the Stokes flow limit, Tripathi *et al.* [49] proposed an analytical expression for the stationary position of the bubble, given by,

$$z_c = \left(\frac{\beta_1 \gamma_c}{2} + \frac{\rho_A R g}{3} \right) \frac{1}{\beta_2 \gamma_c^2} \tag{2.1}$$

where R is the initial radius of the bubble, g is the gravity acceleration, ρ_A is the liquid density, β_1 and β_2 are the first and second temperature coefficients of surface tension, respectively, and γ_c is the temperature gradient.

The counter-current thermocapillary migration of highly confined bubbles in self-rewetting liquids in high aspect ratio channels has been recently examined for the first time by Shanahan & Sefiane [2] by means of experiments and theory. The authors used a heated micro-channel containing 5 wt% water-butanol mixture, with a constant flow rate and subject to a thermal gradient parallel to the flow direction. The schematic of the experiment is presented in FIG. 2.2. For small bubbles, $R \simeq 0.35\, mm$, the authors observed that the bubble approaches asymptotically an equilibrium position close to the surface tension minimum, where the viscous and thermocapillary forces balance. Larger bubbles, $R \simeq 1.1\, mm$ however, lead to steady oscillations around the equilibrium position. The authors also presented a mathematical analysis to describe this phenomenon. Considering the net thermocapillary force of surface tension, the viscous forces associated to the surrounding liquid and the effect of inertia, they derived the bubble equilibrium position and the frequency of the oscillations. Unlike Sefiane & Shanahan [2],

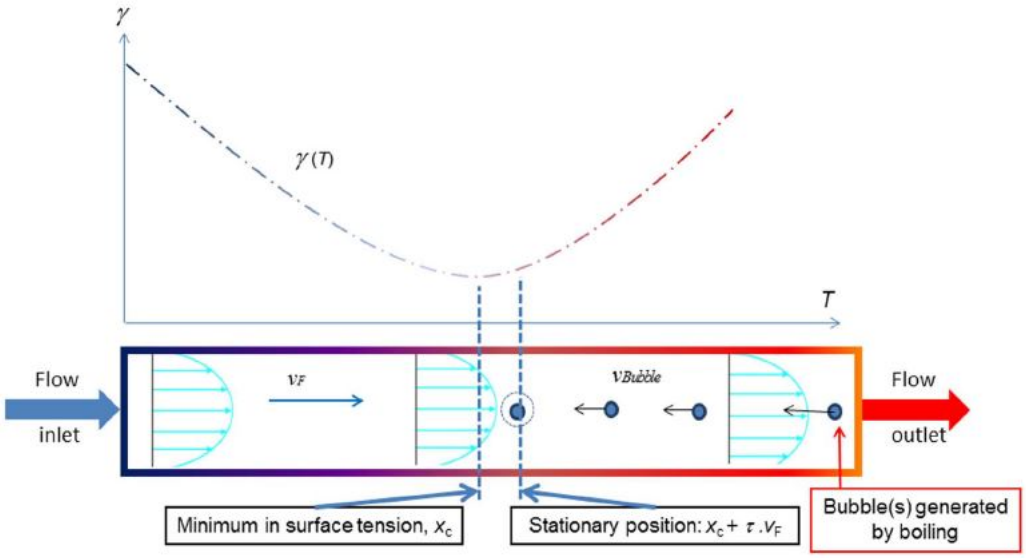

Figure 2.2: Schematic representation of Shanahan & Sefiane's experiment showing the variation of surface tension along the channel. This figure has been obtained from Shanahan & Sefiane [2].

who focus on large bubbles tightly confined in channels, the sizes considered in this thesis allow the bubble to be fully suspended in the tube.

2.2 Instabilities in Liquid Layers

The stability of thin liquid films was reviewed by Oron *et al.* [50] and Crester & Matar [51].

2.2.1 Heating without phase-change

The study on instabilities in liquids layers dates back to the work of Benard [52] who carried out an original experiment in which a horizontal liquid layer was resting in a open dish heat from below, and found a regular hexagonal cellular pattern (Bénard cells) with fluid rising at the centre and falling along the sides. Some years later Rayleigh [53] developed a theoretical study to explain this phenomenon via a driving force due to differential buoyancy in the bulk of the liquid. Only later it was discovered that the hexagon pattern resulted from surface ten-

sion instabilities caused by temperature fluctuations i.e. thermocapillarity on the interface (Pearson [54]).

Pearson [54] observed that drying paint films often display steady cellular circulatory flow similar to those examined by Bénard [52] in liquid layers heated from below. In the former case, the cellular pattern was observed even when the free surface was on the underside of the paint layer and the gravity vector was effectively reverted. Therefore, Pearson [54] concluded that density gradient cannot be the mechanism causing the instabilities in this case and proposed surface tension forces as the driving force of the cellular patterns. Pearson [54] performed a stability analysis on a liquid layer heated from below by means of small-disturbance theory, similar to that developed by Rayleigh [53]. In his analysis surface tension was assumed a linearly decreasing function of temperature, the interface was non-deformable and gravity was neglected. Pearson [54] derived critical values of the Marangoni number, referred by him as a dimensionless number B, corresponding to the case of convective instabilities. Pearson's [54] stability analysis was extended by Scriven & Sternling [55] by accounting for the possibility of shape deformations of the free surface. They found that there is no critical Marangoni number for the onset of stationary instability and that the limiting case of 'zero wave-number' (i.e. waves of very large wavelengths in a thin film) is always unstable. Scriven & Sternling [55] also provided a criterion to distinguish visually whether buoyancy or surface tension dominate cellular convection in liquid pools. While in surface tension driven instabilities, the flow is towards the free surface in shallow sections and away in deeper sections, this relationship is just the opposite in buoyancy-driven flows, as observed by Jeffreys [56]. In this thesis, we present a detailed linear stability analysis for an evaporating layer and further evaluate their late-stage non-linear behaviour using transient simulations.

2.2.2 Effect of long-range molecular forces

Long-range molecular forces become important for stability of the layers (films) when the thickness of the film is of order 1000 Å or lower. Sheludko [57] showed that, for layer thickness of the order of 100 Å, the instability is driven by long-range molecular forces due to van der Waals attractions and results in the rupture of the layer. The critical thickness at which a non-draining film becomes unstable due to van der Waals attractions was considered by Vrij [58]. He used a static stability analysis to calculate the marginally stable thickness at which small disturbances first start to grow. A dynamic linear stability theory for an isothermal film on a horizontal plate was developed by Ruckenstein & Jain [59], based on the Navier-Stokes equations modified with an extra body force due to van der Waals attractions. The theory shows that an initial disturbance periodic along the bounding plane has a critical wavelength much larger than the mean depth of the layer. The analyses above presume that the undisturbed liquid film is both non-draining and laterally unbounded. Gumerman & Homsy [60] examined the consequences of relaxing such restrictions. They used lubrication theory to calculate the film draining and examine the effects of the presence of sidewalls. They found the effect of sidewalls to be very important since the long-wave instabilities treated by Ruckenstein & Jain [59] are sensitive to these, while the effects of draining seem less important. Williams & Davis [61] posed a nonlinear stability theory based on the long-wave nature of the response. They derived a partial differential equation which describes the evolution of the interface shape subject to surface tension, viscous forces, and the van der Waals attractions. They found that the nonlinear measure of the rupture time is always smaller than the equivalent measure given by a linearized theory. Davis [62] discussed the generalization of the result to a non-volatile film on a heated plate, accounting for thermocapillary and gravity-wave effects. Most of the above work considers a single-component layer. In our theoretical model, we account for van der Walls

forces for evaporation of liquid layers comprising a binary mixture.

2.2.3 Effect of phase-change

When the plate that supports the film is heated, new modes of instability develop on the evaporating liquid surface. Hickman [63] noted that vapour recoil can induce hydrodynamic instability. Due to conservation of mass flux during phase change, a liquid particle at the interface accelerates greatly when it becomes vaporized, since the vapour particle has much lower density than does the liquid particle. The back reaction on the interface is called vapour recoil. A disturbance in the evaporating interface can result in a local increase in the evaporation rate at a surface depression or 'trough', producing a local increase in the normal force due to vapour recoil. The associated pressure gradient drives liquid towards the 'crests', amplifying the disturbance.

The effect of rapid evaporation on the stability of a liquid-vapour interface was analysed by Palmer [64] using linear stability analysis. He considered that the evaporation rate depends on the interfacial temperature and investigate the coupling between the 'differential vapour recoil' mechanism and the Marangoni effect. Palmer [64] showed that the rapidly evaporating liquid is unstable to local variations in evaporation rate, local surface depression being produced by stronger vapour recoil and sustained liquid flows being driven by the resultant shear exerted on the liquid surface by the vapour. If the depressed region experiences a local increase in surface temperature, then the induced gradient in surface tension induces a thermocapillary flow of warmer liquid from the trough to the cooler crests to amplify the disturbance. Palmer highlighted the existing competition between the destabilizing surface tension and vapour recoil mechanisms to determine the disturbance wavelength which will be most rapidly amplified.

2.2.4 Non-equilibrium effects

Burelbach *et al.* [65] extended the nonlinear theory developed by William & Davis [61] to include evaporative, thermocapillary, and non-equilibrium effects, in addition to disjoining pressures induced by van der Waals attractions. They derived long-wave evolution equations for the interface shapes that govern the stability of the layers subject to the above coupled mechanisms to investigate film instabilities and rupture. They show that increasing the degree of thermocapillarity decreases the time for rupture of the film. Goussis & Kelly [66] analysed the importance of the layer thickness on thermocapillary instabilities. In sufficiently thick layers instabilities can take the form of relatively short wavelengths which are of the order of the layer's depth, as Pearson [54] demonstrated. This instability is associated with the interaction of the basic temperature with the perturbation velocity field and effects of convection are important. For sufficiently thin films surface tension stabilizes short wavelengths so the instability takes the form of large wavelengths disturbances. This instability is associated with the modification of the basic temperature by the deformation of the free surface. The work presented in this thesis, accounts for the non-equilibrium thermodynamic effects during phase-change, in particular, when components in the liquid mixture layer exhibit competing volatilities.

2.2.5 Surfactant laden Layers

Most work comprising multicomponent liquid layers only consider the presence of surfactants (in addition to the liquid layer). These mainly consider the effect of surfactants on the behaviour of evaporating thin films [67, 68, 69, 70, 71, 72, 73]. For instance, Hatziavramidis [67] studied the stability of thin evaporating films including the flow effects arising from surface tension gradients due to temperature and concentration variations, in addition to van der Waals forces and surface tension. By means of linear stability analysis he shows that the flows driven by

surface tension gradients originating from surfactant concentration variations are in a direction opposite to that of similar flows originating from temperature variations. The former usually dominate and stabilize evaporating films. Danov *et al.* [68] generalized the work of Burelbach *et al.* [65] to account for the presence of a non-volatile dissolved surfactant. Here, the interfacial mass loss due to evaporation, the van der Waals attraction, the Marangoni effect due to thermal and concentration gradients, and the effect of interfacial viscosity on film stability were discussed. They found that increasing the initial surfactant concentration stabilizes the film only upt to the moment of reaching tangential immobbility of the interface due to the increase of its interfacial viscosity and elasticity. After that, the additional increase of surfactant concentration leads only to a decrease of interfacial tension, lowering the film stability. Mikishev & Nepomnyashchy [72] consider the effect of insoluble surfactant on the stability of evaporating liquid layer. They used long-wave approximation to derive a system of nonlinear equations. By means of linear stability analysis they found two modes of instabilities, a monotonic and an oscillatory intability mode, and analysed them in terms of the Marangoni number. This thesis illustrates a full temporal linear stability analysis for an evaporating liquid layer comprising of two miscible components with competing volatilities. Transient simulations are also performed to understand and analyse the non-linear instabilities.

Chapter 3

Numerical investigation of thermocapillary propulsion of bubbles in self-rewetting liquids

This chapter presents a Direct Numerical Simulation (DNS) model based on the two-phase conservation of mass, momentum and energy towards understanding the counter/co-current thermocapillary propulsion of bubbles inside a channel with constant flow rate and constant temperature gradient using self-rewetting liquids without phase change. In self-rewetting liquids, surface tension presents a peculiar non-monotonic dependence on temperature. This will result in a rather different behaviour of the thermocapillary migration of bubbles compared with liquids with a decreasing monotonic dependence of surface tension on temperature previously reported in the literature.

Direct numerical simulations (DNS) based on the volume-of-fluid (VOF) method using Basilisk [38] are performed in order to study the dynamics of bubbles in self-rewetting liquids. The model accounts for interface deformations and for the normal and tangential components of surface tension. The bubble behaviour observed is classified into regimes and the transition between the regimes, the effect

of the bubble deformation on its equilibrium position, and the amplitude and frequency of the observed oscillations are discussed.

3.1 Mathematical modelling

3.1.1 Problem statement

We consider the motion of an axisymmetric gas bubble with radius $\tilde{R}_o$ under the action of thermocapillary forces inside a cylindrical tube of length $\tilde{L}$ and inner radius $\tilde{H}$, as sketched in FIG. 3.1; the tilde denotes dimensional variables. A constant Poiseuille flow with average velocity $\tilde{u}_f$ is established in the tube while a temperature gradient in the flow direction $\tilde{\beta} = d\tilde{T}/d\tilde{z}$ is imposed along the channel walls. The liquid is a binary mixture comprising butanol (5 wt%) and water with properties as shown in Table 3.1 [2]. It must be pointed out that the liquid phase is treated as a single fluid while the gas phase is modelled as a saturated vapour bubble. Phase-change effects are thus neglected. Both fluids are considered incompressible, viscous and immiscible. The density, dynamic viscosity, specific heat capacity and thermal conductivity are denoted by $\tilde{\rho}_l$, $\tilde{\mu}_l$, $\tilde{c}_{pl}$, $\tilde{k}_l$ for the liquid, and $\tilde{\rho}_g$, $\tilde{\mu}_g$, $\tilde{c}_{pg}$, $\tilde{k}_g$ for the gas, respectively. The surface tension is defined by a parabolic function of temperature as,

$$\tilde{\sigma} = \tilde{\sigma}_o + \tilde{\gamma}(\tilde{T} - \tilde{T}_o)^2 \tag{3.1}$$

where $\tilde{T}_o$ is the temperature corresponding to the surface tension minimum $\tilde{\sigma}_o$, and $\tilde{\gamma} = (1/2)d^2\tilde{\sigma}/d\tilde{T}^2|_{\tilde{T}_o}$ is the second order temperature coefficient of surface tension. The variation of surface tension, related to the temperature along the channel wall, the position z_o, associated to the surface tension minimum, and the bubble equilibrium position z_e are shown schematically in FIG. 3.1.

$\rho\,[kg\,m^{-3}]$	967
$\mu\,[N\,s\,m^{-2}]$	0.43×10^{-3}
$\alpha\,[m^2\,s^{-1}]$	1.5×10^{-7}
$\sigma_o\,[N\,m^{-1}]$	30.62×10^{-3}
$\gamma\,[N\,m^{-1}\,K^{-2}]$	1.19×10^{-6}

Table 3.1: Properties for 5 wt.% butanol/water mixture at $70\,^oC$.

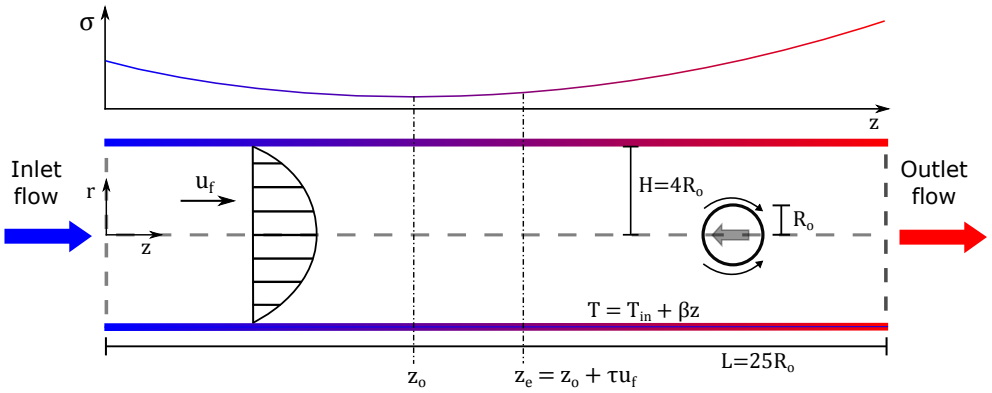

Figure 3.1: Schematic of the mathematical model and, on top, the surface tension coefficient related to the temperature along the channel wall.

3.1.2 Scaling

The current scaling defines the tube diameter $\tilde{D} = 2\tilde{H}$ as the length scale, the temperature difference between the temperature corresponding to the surface tension minimum and the inlet temperature $\Delta\tilde{T} = \tilde{T}_o - \tilde{T}_1$ as the temperature scale and the average flow velocity is taken as the reference velocity, $\tilde{U}_o = \tilde{u}_f$. Taking the liquid properties as reference, the resulting scaling reads:

$$\tilde{\mathbf{x}} = \tilde{D}\mathbf{x}, \qquad \tilde{\mathbf{u}} = \tilde{U}_o\mathbf{u}, \qquad \tilde{t} = \frac{\tilde{D}}{\tilde{U}_o}t, \qquad \tilde{p} = \tilde{\rho}_l\tilde{U}_o^2 p, \qquad \tilde{T} = \tilde{T}_1 + \Delta\tilde{T}T$$
$$\tilde{\rho} = \tilde{\rho}_l\rho, \qquad \tilde{\mu} = \tilde{\mu}_l\mu, \qquad \tilde{c}_p = \tilde{c}_{pl}c_p, \qquad \tilde{k} = \tilde{k}_l k, \qquad \tilde{\sigma} = \tilde{\gamma}(\Delta\tilde{T})^2\sigma \quad (3.2)$$

where $\tilde{\mathbf{x}} = (\tilde{z}, \tilde{r})$ is the longitudinal and radial coordinates, $\tilde{\mathbf{u}} = (\tilde{u}, \tilde{v})$ the velocity vector, $\tilde{t}$, $\tilde{p}$, and $\tilde{T}$ the time, pressure and temperature, respectively. The temperature gradient $\tilde{\beta}$ is scaled by $\Delta\tilde{T}/\tilde{D}$.

3.1.3 Governing equations

Applying the previous scaling to the conservation of mass, momentum and energy renders the following set of dimensionless equations respectively,

$$\nabla \cdot \mathbf{u} = 0 \tag{3.3}$$

$$\rho\left[\frac{\partial \mathbf{u}}{\partial t} + \nabla \cdot (\mathbf{u}\mathbf{u})\right] = -\nabla p + \frac{1}{Re}\nabla \cdot \left[\mu\left(\nabla \mathbf{u} + \nabla \mathbf{u}^T\right)\right] + \frac{1}{ReCa}\left(\sigma\kappa\hat{\mathbf{n}} + \nabla_s\sigma\right)\delta \tag{3.4}$$

$$\rho c_p\left[\frac{\partial T}{\partial t} + \nabla \cdot (T\mathbf{u})\right] = \frac{1}{Pe}\nabla \cdot (k\nabla T) \tag{3.5}$$

where $Re = \tilde{\rho}_l \tilde{U}_o \tilde{D}/\tilde{\mu}_l$ is the Reynolds number, $Ca = \tilde{\mu}_l \tilde{U}_o/\tilde{\gamma}(\Delta\tilde{T})^2$ the capillary number and $Pe = \tilde{U}_o\tilde{D}/\tilde{\alpha}_l$ the Peclet number. In the surface tension term at the r.h.s. of momentum equation, $\sigma\kappa\hat{n}$ is the normal stress at the interface and $\nabla_s\sigma$ the tangential stress. The interface curvature is defined as $\kappa = -\nabla_s \cdot \hat{\mathbf{n}}$, the unit vector normal to the interface as $\hat{\mathbf{n}} = \nabla c/|\nabla c|$, where c is the volume fraction of the liquid phase, the gradient operator tangent to the interface as $\nabla_s = \nabla - \hat{\mathbf{n}}(\hat{\mathbf{n}} \cdot \nabla)$, and a Dirac delta function as $\delta = |\nabla c|$ that has a positive finite value at the interface and zero elsewhere.

In order to model the two-phase system, the fluids are identified by the liquid volume fraction c, which takes 1 for the liquid phase, 0 for the gas phase and $0 < c < 1$ at the interface. The volume fraction is advected through the domain by the following conservation equation,

$$\frac{\partial c}{\partial t} + \nabla \cdot (c\mathbf{u}) = 0 \tag{3.6}$$

Since the gas volume fraction is simply $(1-c)$, one can use the so-called single-fluid formulation, in which the physical properties of both fluids are defined by a single set of scalar fields for the whole domain. In this formulation, the governing equations for both fluids can be solved as a single set of equations, where the

dimensionless fluid properties are given by an arithmetic average as,

$$\phi = c + (1 - c)\phi_r \tag{3.7}$$

where $\phi = \rho, \mu, c_p, k$ are the single fluid properties and ϕ_r are the properties ratios defined as $\rho_r = \rho_g/\rho_l$, $\mu_r = \mu_g/\mu_l$, $c_{pr} = c_{pg}/c_{pl}$ and $k_r = k_g/k_l$.

To close the set of equations the dimensionless surface tension takes the form,

$$\sigma = \sigma_{ref} + (T - 1)^2 \tag{3.8}$$

where $\sigma_{ref} = \tilde{\sigma_0}/\tilde{\gamma}(\Delta\tilde{T})^2$ is the dimensionless reference surface tension. For the parabolically-varing surface tension as defined here its gradient along the interface is given by $\nabla_s\sigma = 2(T-1)\nabla_s T$, which accounts for the thermocapillary tangential stress.

3.1.4 Boundary and initial conditions

The impermeable no-slip and fixed temperature boundary conditions are applied to the wall of the cylindrical channel, while the symmetry boundary conditions are imposed to the axis of the channel. Specifically,

$$\text{At} \quad r = H: \qquad u = 0, \qquad v = 0, \qquad T = T_{in} + Bz \tag{3.9}$$

$$\text{At} \quad r = 0: \qquad \frac{\partial u}{\partial r} = 0, \qquad v = 0, \qquad \frac{\partial p}{\partial r} = 0, \qquad \frac{\partial T}{\partial r} = 0 \tag{3.10}$$

where $B = (\tilde{D}/\Delta\tilde{T})\tilde{\beta}$ is the non-dimensional temperature gradient and T_{in} the inlet temperature of the flow.

At the inlet, we impose the Poiseuille flow velocity profile, which in dimensionless form is given by $u(r) = \frac{Re\Delta P}{4L}(H^2 - r^2)$, where $\Delta P = 8L/ReH^2$. Similarly, the inlet temperature is prescribed using Dirichlet boundary condition. At the outlet we define an open boundary with pressure equal to zero,

$$\text{At} \quad z = 0: \qquad u = u(r), \qquad \frac{\partial p}{\partial z} = 0, \qquad T = T_{in} \tag{3.11}$$

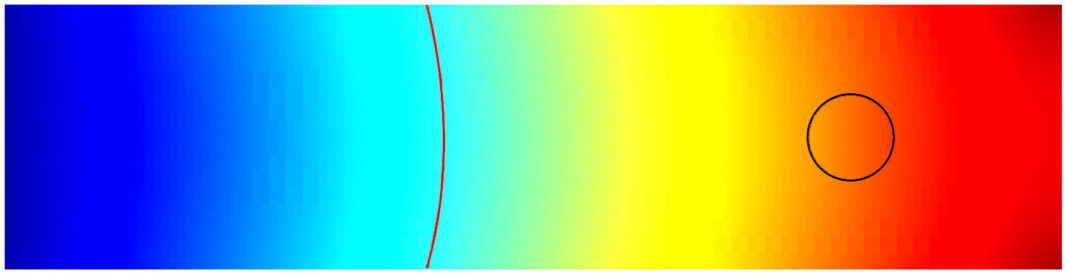

Figure 3.2: The temperature field at the moment that the bubble is introduced. The red line corresponds to the temperature referring to the surface tension minimum and the black circle is the interface of the bubble.

$$\text{At} \quad z = L: \qquad \frac{\partial u}{\partial z} = 0, \qquad p = 0, \qquad \frac{\partial T}{\partial z} = 0 \tag{3.12}$$

The initial conditions will be given by the Poiseuille velocity field and a linear temperature gradient along the flow direction. Note that these will later be affected by the presence of the bubble.

After the temperature field adjusts to the effect of convection, at $t = 10$, the bubble is introduced at the downstream side of the channel in the region of positive surface tension gradient, FIG. 3.2.

3.1.5 Numerical method

The axisymmetrical governing equations are solved using the open-source Basilisk code [38]. The code makes use of the finite volume method, the Bell-Colella-Glaz advection scheme [74] and an implicit viscosity solver. The interface is captured by the Volume of Fluid method [75] and the surface tension is calculated using the well-balanced continuum surface force model [76, 77] with the height-function method [78] to calculate the interface curvature. We use the capillary time restriction [76] given by $dt = \sqrt{\rho\Delta^3/\pi\sigma}$, where Δ is the smallest mesh size, to prescribe the time-step size, and ensure that convergence is achieved upon mesh refinement.

In what follows, we present results for the following set of base parameters: $\rho_r = 1/1000$, $\mu_r = 1/100$, $k_r = 1/30$, $c_{pr} = 1/4$, $\sigma_r = 5.732$, $B = 0.1$, and

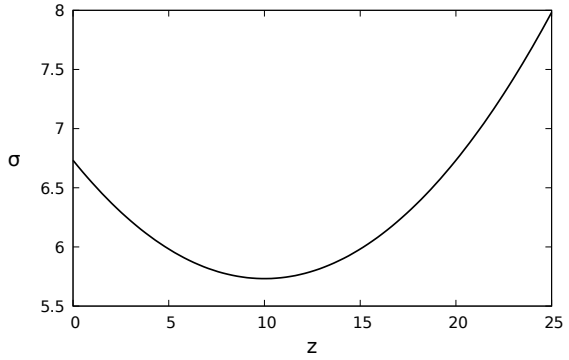

Figure 3.3: The variation of surface tension through the channel for a strong temperature gradient $B = 0.1$ and $\sigma_r = 5.732$.

$Pe = 0.1$; which represent the liquid-gas system in the experiments presented in Shanahan & Sefiane [2] in the presence of a strong temperature gradient and with a small Peclet number to avoid substantial thermal advection by the bulk fluid flow. FIG. 3.3 shows the variation of surface tension along the channel for the set of base parameters.

3.1.6 Tangential component of surface tension and validation

The tangential component of surface tension force was implemented in the Basilisk solver. To that end the tangential component is expressed as a function of the temperature and volume fraction gradients, written as,

$$[\nabla_s T]_i \delta = \left[\frac{\partial T}{\partial x_i} - \frac{1}{|\nabla c|^2}\left[\left(\frac{\partial c}{\partial x}\frac{\partial T}{\partial x}\right)\frac{\partial c}{\partial x_i} + \left(\frac{\partial c}{\partial y}\frac{\partial T}{\partial y}\right)\frac{\partial c}{\partial x_i} + \left(\frac{\partial c}{\partial z}\frac{\partial T}{\partial z}\right)\frac{\partial c}{\partial x_i}\right]\right]|\nabla c| \tag{3.13}$$

here the gradients of the volume traction c and the temperature T are computed at the centre of the cells using a central difference scheme. In accordance with the staggered grid formulation, after the forces are computed at the centre of the cells they are interpolated to the face of the cells and included in the momentum equation as velocity source terms.

This implementation is validated against a classical 2D problem of thermo-

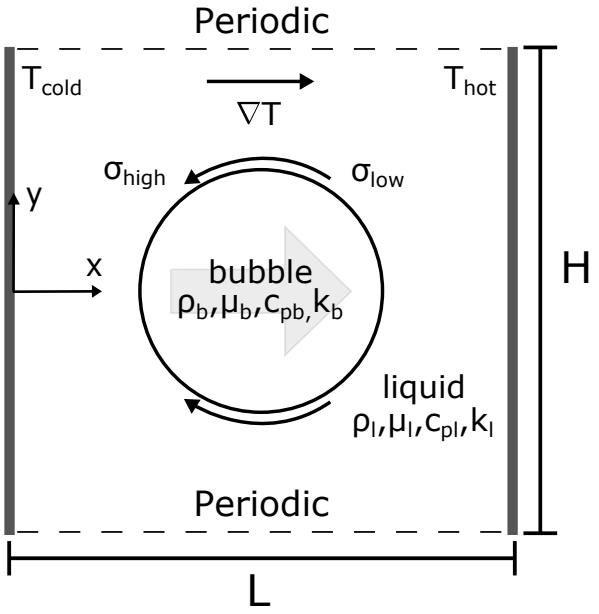

Figure 3.4: Schematic of the domain for the 2D problem used for the validation.

capillary migration reported in the literature [4, 3]. It considers the motion of a bubble with initial radius R_o, immersed in a quiescent liquid with an imposed temperature gradient ΔT in the horizontal direction, as sketched in FIG. 3.4.

The domain is a rectangular box of size $L \times H$ with periodic boundary conditions in the y-direction and bounded by rigid walls with no-slip condition in the y-direction and no penetration in the x-direction. The right wall is hot, the left wall is cold, and initially the temperature of the whole domain varies linearly in the x-direction. The bubble starts at the center of the box and it is surrounded by the bulk fluid. The fluid properties of the gas bubble are denoted by the subscript g while the properties of the liquid by the subscript l. Both fluids are incompressible, viscous and immiscible and governed by the same conservation equations as described by eqs. 3.3-3.6, with the Marangoni number, Ma, in the place of the Peclet number, Pe. For this case the surface tension is a decreasing linear function of temperature, written in dimensionless form as,

$$\sigma = 1 - CaT \tag{3.14}$$

where Ca is the capillary number, T is the temperature and the temperature

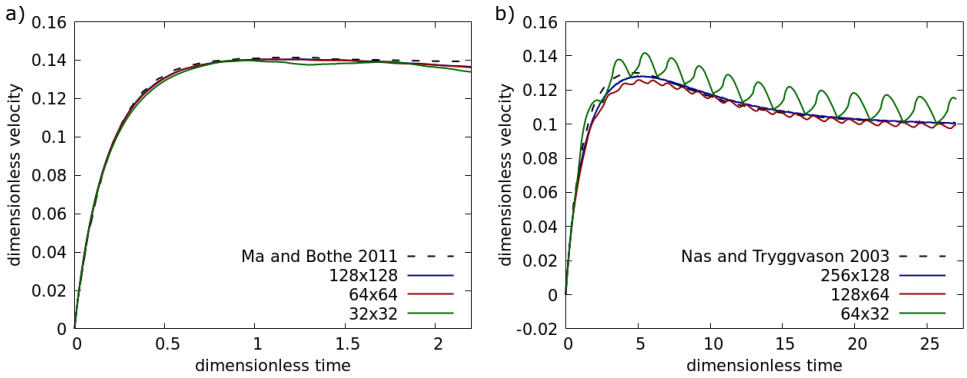

Figure 3.5: Validation of the numerical model. a) Comparison against the results presented in Ma & Bothe [3] for the set of parameters $Re = Ma = 0.72$ and $Ca = 0.0576$ and a domains size of $L = H = 4R$. b) Comparison against the results presented in Nas & Tryggvason [4] for the set of parameters $Re = 5$, $Ma = 20$ and $Ca = 0.01666$ and domains size of $L = 8R$ and $H = 4R$.

scale is given by $T = (T_{hot} - T)/(T_{hot} - T_{cold})$.

The results were compared against the set of parameters reported in Ma & Bothe [3] and Nas & Tryggvason [4]. For all sets of parameters the properties ratios are $\rho_r = \mu_r = \alpha_r = 0.5$. In FIG. 3.5a the results are compared against Ma & Bothe [3] using $Re = Ma = 0.72$ and $Ca = 0.0576$, and in FIG. 3.5b the results are compared against Nas & Tryggvason [4] using $Re = 5$, $Ma = 20$ and $Ca = 0.01666$. In both cases the velocity of the bubble presents the same behaviour as reported in the literature and converges upon mesh refinement.

3.2 Theoretical prediction

In the work by Shanahan & Sefiane [2] they proposed a theoretical explanation for the counter-current migration of bubbles in a channel with constant flow rate and constant temperature gradient along the flow for liquids with a parabolic dependence of surface tension on temperature. They consider the inertial term, the viscous drag on the bubble and the net force of surface tension, using the following form of the Navier-Stokes equation,

$$\frac{2}{3}\tilde{\rho}\pi\tilde{r}_o^3\frac{d^2\tilde{z}}{d\tilde{t}^2} + 4\pi\tilde{r}_o\tilde{\mu}\left(\frac{d\tilde{z}}{d\tilde{t}} - \tilde{v}_f\right) + \frac{16}{3}\pi\tilde{r}_o^2\tilde{\gamma}\tilde{\beta}^2(\tilde{z} - \tilde{z}_o) = 0 \tag{3.15}$$

where $\tilde{v}_f$ is the average flow velocity and $\tilde{z}_o$ is the position corresponding to the surface tension minimum.

After applying the scaling defined in Section 3.1.2, the Navier-Stokes equation becomes,

$$\rho r_o^2 \frac{d^2 z}{dt^2} + \frac{6\mu}{Re}\frac{dz}{dt} + \frac{8r\beta^2}{ReCa}\left(z - z_o - \frac{3\mu u_f}{4r_o\beta^2}Ca\right) = 0 \tag{3.16}$$

where Re and Ca are the same as defined before.

For the case of small bubbles where the inertial term can be neglected, the solution of eq. 3.16 presents decaying exponential behaviour and the bubble equilibrium position, presented here in dimensionless form, is given by,

$$z_e = z_o + \frac{3\mu u_f}{4r\beta^2}Ca \tag{3.17}$$

For the case with inertia the solution of eq. 3.16 involve exponentials with either real or imaginary arguments, the former corresponds to decaying exponential behaviour and the latter to oscillatory behaviour. The angular frequency associated with the oscillatory behaviour, in dimensionless forms, is given by,

$$w = \sqrt{\frac{8\beta^2}{ReCa} - \frac{9}{Re^2}} \tag{3.18}$$

The theoretical prediction for the bubble equilibrium position, z_e, and for the frequency of the oscillations, $f = w/2\pi$, will be used later to compare against the numerical results.

3.3 Results and Discussion

We start the discussion of our results by showing a typical case of counter-current thermocapillary migration of a bubble inside a channel with self-rewetting fluid and positive temperature gradient. FIG. 3.6 illustrates the time evolution of the centre of mass, z_b, and velocity, u_b, of the bubble together with a sequence of panels showing the bubble motion. Unlikely in more classic fluids, the bubble is

propelled against the flow towards the cold side until it comes to a halt at an equilibrium point located to the right of the surface-tension minimum. For simple fluids with a linear dependence of surface tension on temperature we would expect that the bubble migrates towards the hot side of the channel. This unusual behaviour is because the bubble is introduced in a region where the surface tension has a positive slope thereby making the thermocapillary stresses to drive the fluids surrounding the bubble towards the hot side while the bubble is propelled in the opposite direction against the flow. FIG. 3.6(b) shows that, the bubble first accelerates counter-current, reaches a maximum velocity, and then decelerates until its velocity goes to zero at the equilibrium position. As the bubble moves in direction to the surface tension minimum, the slope of surface tension gradient (driving force) becomes weaker because of the parabolic profile of surface tension, thereby reducing the thermocapillary forces acting on the bubble. The equilibrium position is that at which the thermocapillary forces balance the drag forces exerted by the flow. Note that the bubble can never reach the point of minimum surface tension since the Marangoni force vanishes there, and there is thus no force to oppose to the viscous drag. In the simulation we found an equilibrium position of $z_e = 12.38$ which is close to the equilibrium position predicted by eq. 1 $z_e = 12.08$, considering the set of base parameters, $Re = 16$ and $Ca = 1.15 \times 10^{-2}$, with the surface tension minimum located at $z_o = 10.36$ and the local flow velocity $u_f = 2$.

The influence of the confinement on the bubble motion was analysed by observing the effect of H on the bubble velocity while keeping Re constant. For $H < 3R$ a reduction on the bubble velocity was observed because of the increase in the drag force due to the proximity of the wall, while for $H > 4R$ a reduction on the bubble velocity was observed because of the deviation in the temperature gradient from linearity due to the thermal advection cause by the Poiseuille flow. Therefore, $H = 4R$ was chosen in order to not have influence from the proximity

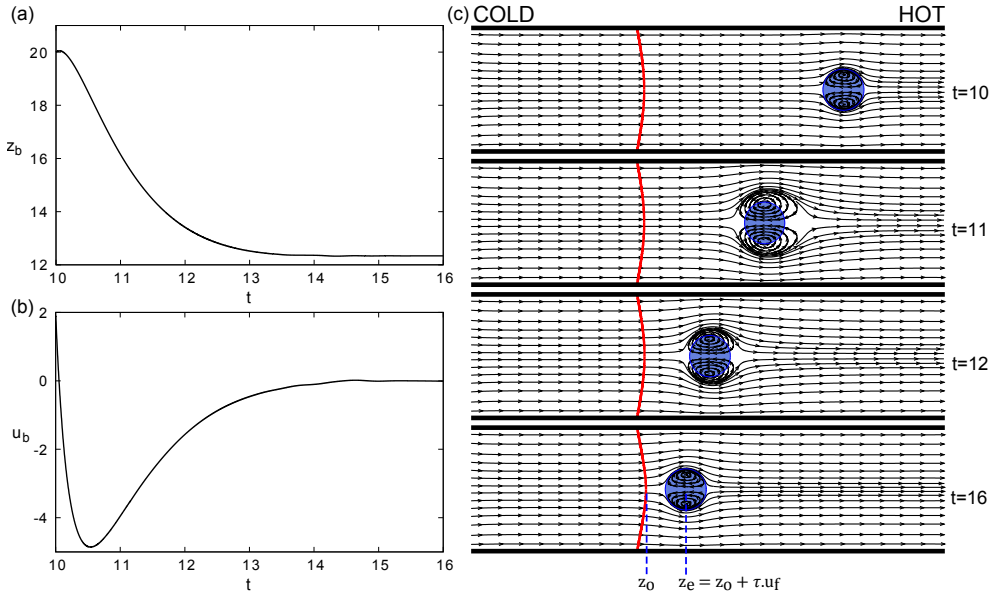

Figure 3.6: Time evolution of (a) the center of mass z_b and (b) velocity u_b of the bubble for the set of base parameters with $Re = 16$ and $Ca = 1.15 \times 10^{-2}$. At the right the panels showing the bubble motion with the streamlines (black lines), the bubble interface (blue line) and the isothermal line for $T = 1$ corresponding to the minimum in surface tension (red line).

of the wall neither from thermal advection on the bubble velocity. In this work the tube diameter was chosen as the length scale in order to have Re based on the flow.

3.3.1 Regime map

Based on the dynamics of the bubble during the thermocapillary migration we build a map on the parameter space of Re and Ca by running a series of simulations in the rage $0.1 < Re < 10^4$ and $10^{-5} < Ca < 10^{-1}$. This is illustrated in FIG. 3.7. In this map we clearly identify four different possible behaviours of bubble motion: i) 'counter-current propulsion' where the bubble migrates against the flow and asymptotically approaches a stable equilibrium position; ii) 'damped oscillations' where the bubble migrates against the flow and oscillate before it comes to a halt at a stable equilibrium position; iii) 'sustained oscillations' where the bubble presents steady oscillations around its equilibrium position; iv) 'co-current migration' where the channel flow is much stronger than thermocapillarity and

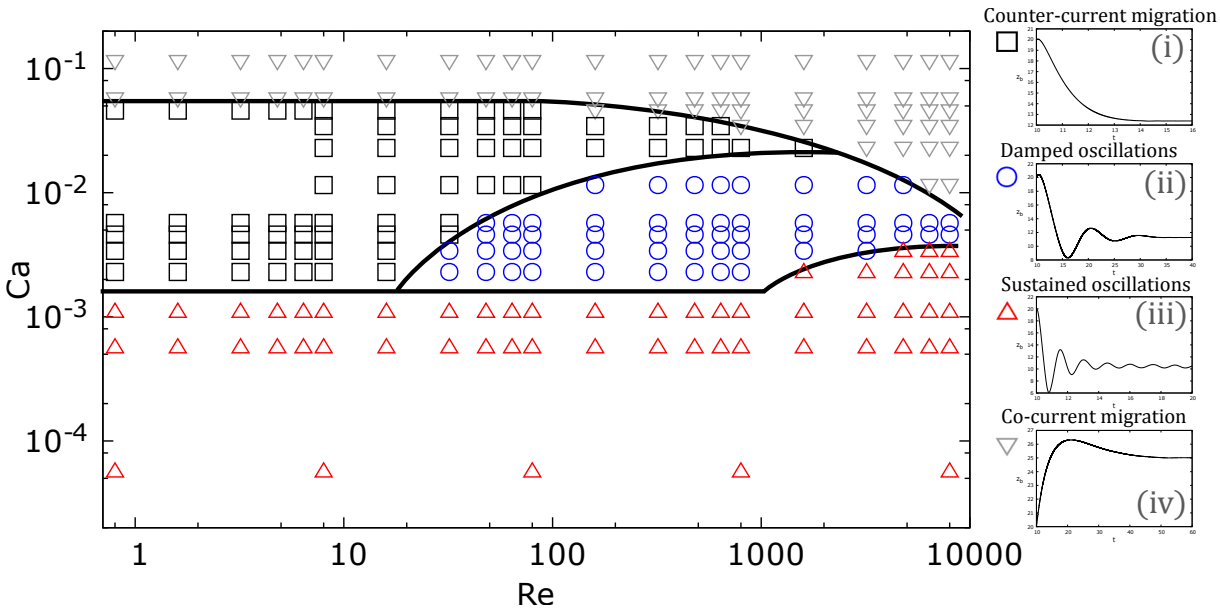

Figure 3.7: Map with the four bubble behaviours in the *Re vs Ca* parameters space. Region (i) is the counter-current propulsion, region (ii) the damped oscillations, region (iii) the sustained oscillations, and region (iv) the co-current migration.

the bubble is dragged away downstream.

In this map Re represents the ratio between inertia to viscous forces while Ca represents the ratio between viscous to thermocapillary forces. Re is controlled by the average flow velocity U_o and Ca is predominantly controlled by the temperature difference ΔT. The left region of the map is characterized by low inertia and as Re increase by increasing U_o and ΔT to make Ca constant, it goes to the region of high inertia in the right part of the map. For high Ca (low ΔT) the viscous forces dominate over the thermocapillary forces and the bubble is pushed by the fluid flow shifting the equilibrium position z_e downstream away from the location of the surface tension minimum. This is represented by the co-current migration regime in the upper region of the map. As Ca decreases by increasing ΔT the thermocapillary forces get stronger and the bubble starts to propel against the flow and z_e is shifted upstream in direction to the location of the surface tension minimum. This is represented by the counter-current propulsion (low inertia) and damped oscilations (high inertia) regimes in the middle region of the map. For low Ca (high ΔT) the thermocapillary forces are much stronger

than the viscous forces and z_e reaches very close to the location of the surface tension minimum and the bubble start to oscillate around z_e. The oscillations have high frequency and low amplitude in the low inertia region at the left side of the map and low frequency and high amplitude in the high inertia region at the right side. This is represented by the sustained oscillations regime in the lower part of the map.

While Shanahan & Sefiane's [2] experiments considered laterally confined bubbles, this work considers fully suspended bubbles in cylindrical tubes and reveals regimes of bubble motion for the first time. It also shows the dependency of Re and Ca on the flow regimes and how increasing the thermocapillary forces leads to the sustained oscillations.

3.3.2 Flow regimes

The role of Re and Ca on the bubble dynamics through four different regimes in the map is illustrated in FIG. 3.8. Here, the trajectory of the bubble's centre of mass, z_b, and the time evolution of aspect ratio, defined as the height by the width, $A_r = h/w$, for different values of Re and Ca are shown. FIG. 3.8(a,b) shows that as Ca is increased, z_e is shifted away from the location of the surface tension minimum that is around $z = 10$ due to a decrease in the thermocapillary forces in relation to the viscous force exerted by the bulk fluid. For $Re = 800$, z_e is shifted even more downstream because the bubble deformation becomes more relevant for high values of Re and Ca. For high values of Ca the bubble goes into the co-current migration regime where the thermocapillary forces are not strong enough to propel the bubble against the flow. In this regime the viscous forces dominate over the thermocapillary forces. At moderate values $Ca > O(10^{-3})$ and low Re the bubble presents a steady propulsion against the flow characterizing the counter-current propulsion regime. Increasing Re at moderate values $Ca > O(10^{-3})$, the bubble starts to be subject to damped oscillations due to the increase

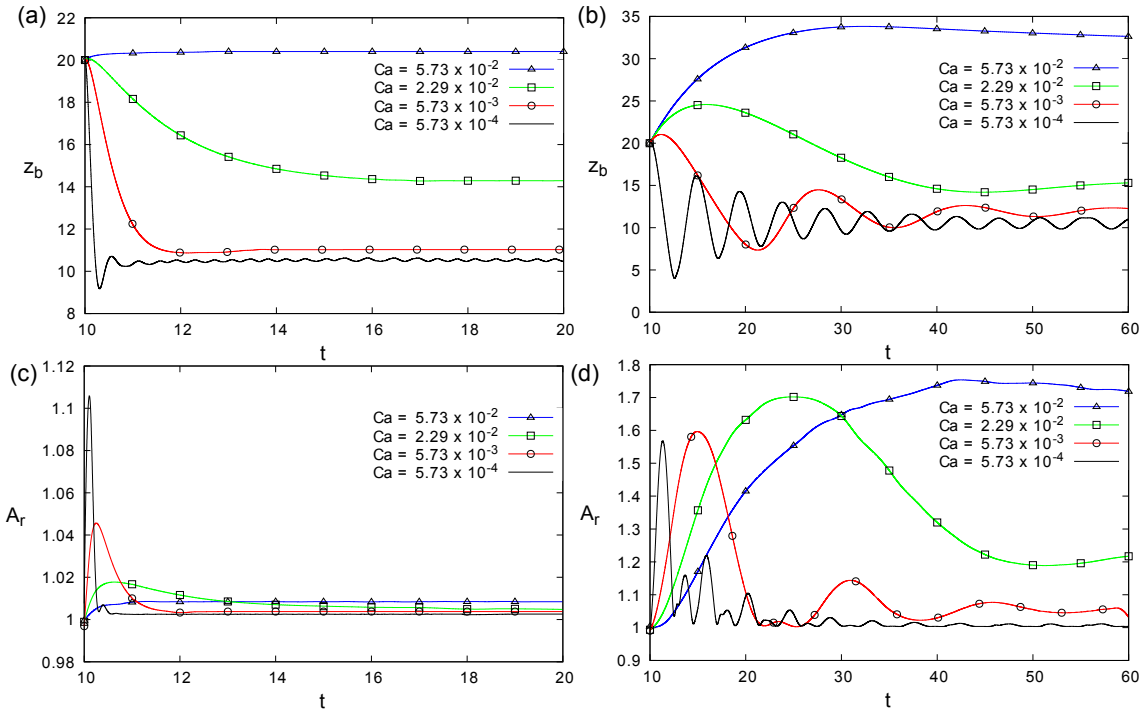

Figure 3.8: Time evolution of (a,b) the center of mass, z_b, and (c,d) the aspect ratio of the bubble for different capillary numbers with $Re = 8$ (left) and $Re = 800$ (right).

of inertia in relation to viscous forces. In these two regimes there is a competition between the viscous and thermocapillary forces. As we decrease Ca, z_e shifts upstream and the bubble starts to present sustained oscillations around z_e as can be seen with $Ca < 10^{-3}$. In this regime the thermocapillary forces dominate over the viscous forces.

The bubble deformation is analysed in FIG. 3.8(c,d). This figure shows that for the cases with co-current motion, where the bubble moves in the flow direction at high Ca, the bubble deformation increase monotonically as the bubble moves towards its equilibrium position. For the cases where the bubble migrates against flow, the bubble deformation has a peak of largest deformation when z_b reaches the maximum slope during the counter-current motion. For $Re = 8$ the largest deformation increases as we decrease Ca showing that in this case the bubble deformation is mainly dependent on the bubble velocity that increases by decreasing Ca. While for $Re = 800$ the largest deformation increases with Ca showing a transition where the bubble deformation is more sensitive to the

normal forces acting on the bubble that reduces by increasing Ca. For the case of sustained oscillations and high Re the deformations became smaller as the amplitude of the oscillations decrease reducing the maximum velocity achieved by the bubble at each oscillation. During the oscillations the co-current motion has smaller bubble deformation than the counter-current motion as the bubble experiences stronger viscous forces in the later case.

3.3.3 Transition regions

In FIG. 3.9 we analyse the transition from region (i) to region (ii) in the map. In this figure it is shown the trajectory of the bubble, z_b, and the aspect ratio A_r. FIG. 3.9(a) shows that, as we increase Re the bubble dynamics change from an asymptotically movement towards the equilibrium position to damped oscillations before coming to a halt at the equilibrium position. This is due to the increase in inertia that retards the action of the thermocapillary forces allowing the bubble to oscillate before halt at its equilibrium position. The amplitude of these oscillations increase as we increase Re. In the map we can see that as Ca increases the thermocapillary force is reduced and we need higher contribution of inertia (higher Re) to see the damped oscillations. FIG. 3.9(b) shows that increasing Re results in the largest deformation (first peak) and as the bubble oscillates more we can see a second small peak corresponding to the counter-

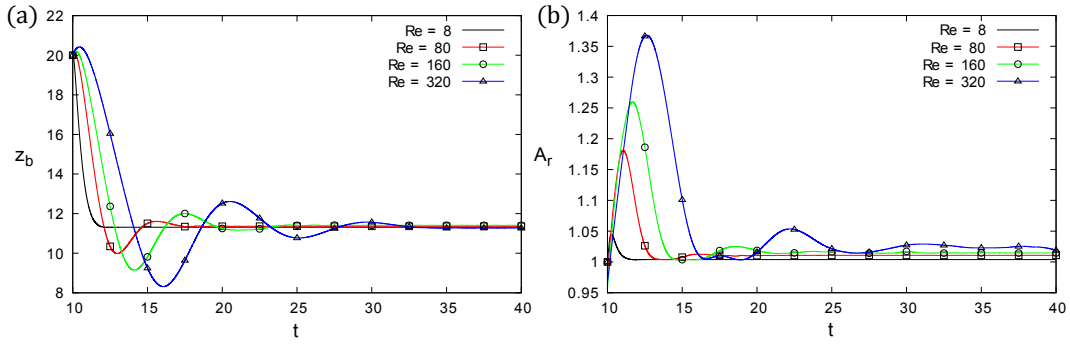

Figure 3.9: Time evolution of the bubble center of mass, z_b, showing the transition from region (I) to region (II) increasing the Reynolds number for $Ca = 5.73 \times 10^{-3}$.

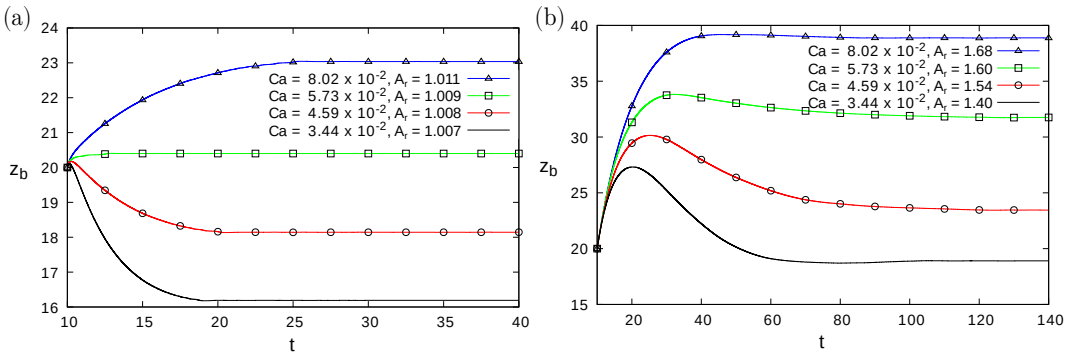

Figure 3.10: Time evolution of the bubble center of mass, z_b, and the aspect ratio A_r at the equilibrium position, showing the transition to region (IV) increasing the capillary number for (a) $Re = 8$ and (b) $Re = 800$.

current motion of the second oscillation.

The transition to region (iv) on the map is illustrated in FIG. 3.10. The co-current migration is characterized when the bubble equilibrium position is to the right side of its initial position, i.e. $z_e > 20$. Increasing Ca reduces the effect of the thermocapillary forces; at some point it is not strong enough to overcome the viscous forces of the bulk fluid and to propel the bubble counter-current. Therefore, the bubble is carried by the flow and as it moves away from the surface tension minimum, the thermocapillary forces increase, because of the increase in the slope of the surface tension curve, until it balances the viscous forces keeping the bubble in a stable equilibrium position. We can see in FIG. 3.10 that increasing Re makes z_e to be shifted more to the right because of the increase in the bubble deformation that indicates stronger inertial forces felt by

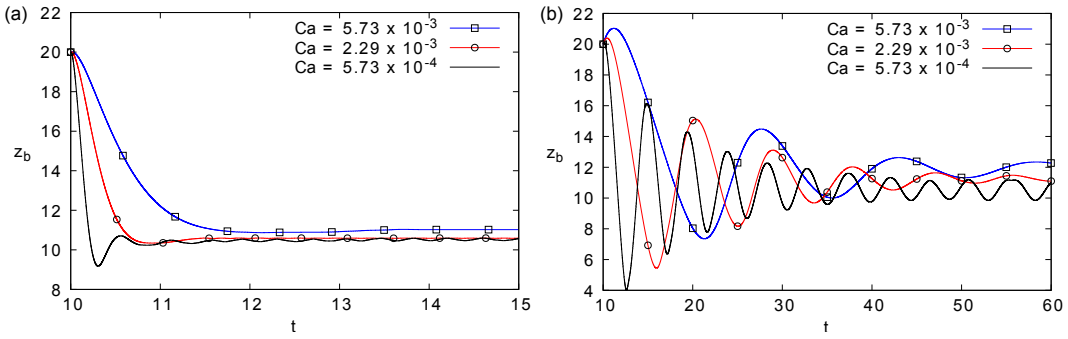

Figure 3.11: Time evolution of the bubble center of mass, z_b, showing the transition to region (III) decreasing the capillary number for (a) $Re = 8$ and (b) $Re = 800$.

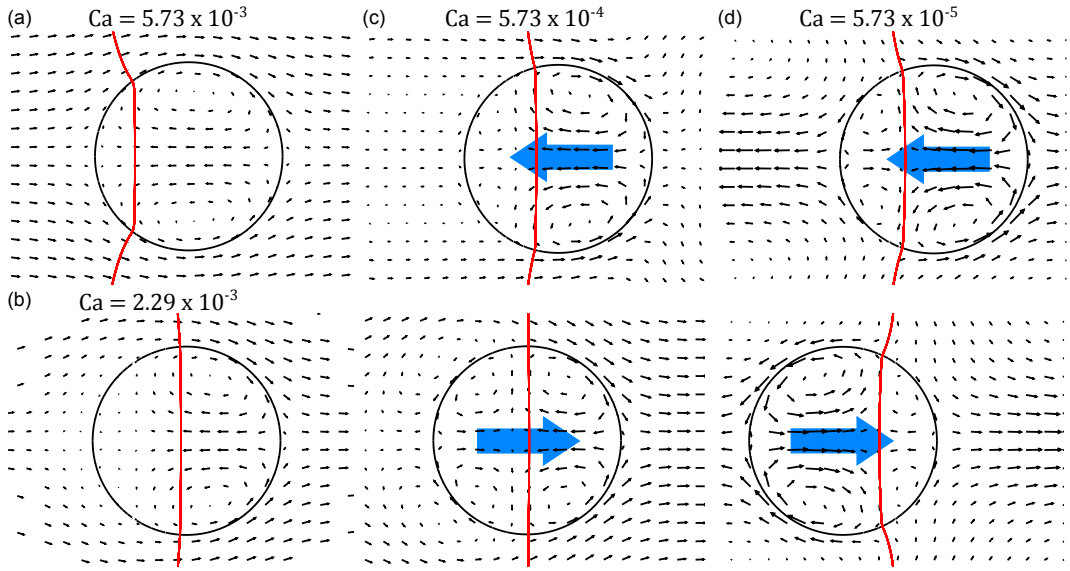

Figure 3.12: The vector field and the isothermal line corresponding to the surface tension minimum showing the transition to sustained oscillations for $Re = 8$. (a) and (b) are stable equilibrium positions showing how z_e moves in direction to the surface tension minima by decreasing Ca and (c) and (d) are the right most (top) and the left most (bottom) position during the oscillation around z_e that arise and increase their amplitude by decreasing Ca.

the bubble. This dependence of the equilibrium position on bubble deformation explains why the boundary to region (iv) drops down towards lower Ca as we increase Re.

The transition to sustained oscillations is illustrated in FIG. 3.11 and 3.12. The sustained oscillations arise when the thermocapillary forces are strong enough to bring z_e close to the surface tension minimum. This is characterized when the isothermal line corresponding to the surface tension minimum almost crosses the centre of the bubble, FIG. 3.12(b). After the bubble gets close enough to the location of the surface tension minimum the thermocapillary force almost balances against the flow inertia (ρU_o^2) causing the bubble to oscillate around z_e. The map shows that the transition to sustained oscillations depends only on Ca for most part of the map in agreement with the fact that this transition depends on the location of z_e considering that the theoretical equilibrium position does not depend on Re. Only for $Re > 1000$, where we have very high contributions of inertia the oscillations start to depend on Re as well.

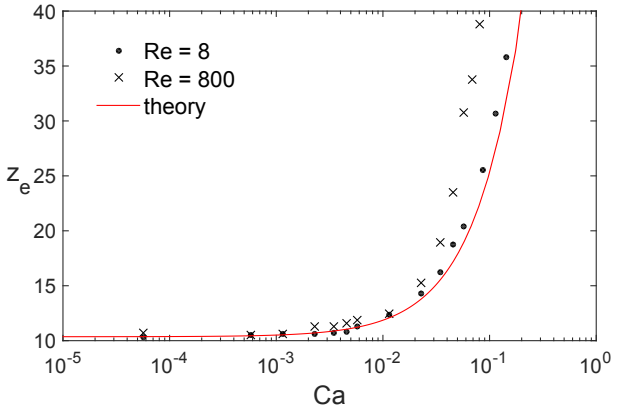

Figure 3.13: Comparison between the numerical bubble equilibrium position for $Re = 8$ and $Re = 800$, and the theoretical prediction.

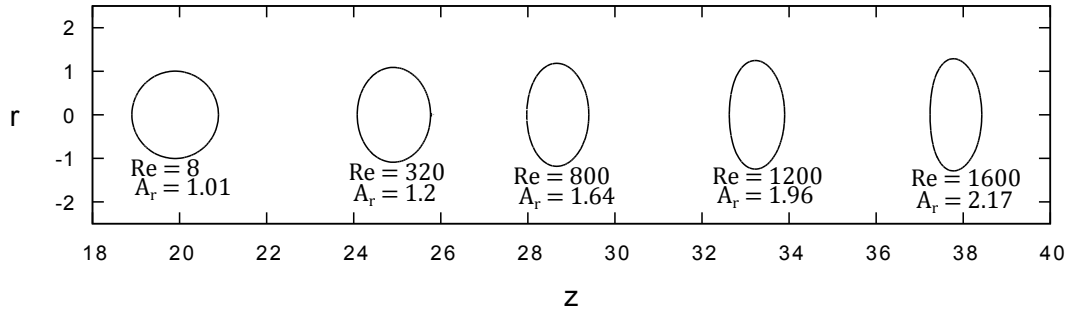

Figure 3.14: Bubble shape at the equilibrium position for different values of Re and $Ca = 5.73 \times 10^{-2}$.

3.3.4 Equilibrium position

The results are compared against the theoretical equilibrium position prescribed by eq. 3.17. In FIG. 3.13 we can see that z_e in the simulations follows the same trend as the theory and it has an exponential growth in the log scale indicating it grows linearly with Ca as predicted by theory. We can also see a good agreement for low capillary numbers, while for $Ca > 10^{-2}$ the numerical results start to deviate from theory. This deviation is because the theory does not account for bubble deformation that starts to be relevant for high Ca and Re. Comparing the equilibrium position for different Re we can see an even higher deviation for $Re = 800$, what is in agreement with the fact that this deviation is caused by the bubble deformation that increases with Re and Ca.

The effect of bubble deformation on z_e is illustrated in FIG. 3.14. In this

figure we analyse the change of the bubble aspect ratio in relation to Re for $Ca = 5.73 \times 10^{-2}$ and how it affects z_e. Increasing Re results in the bubble being more ellipsoidal. This ellipsoidal shape increase the drag force acting on the bubble by the fluid flow, thereby shifting z_e downstream in the channel. For $Ca = 5.73 \times 10^{-2}$ the equilibrium position predicted by eq. 3.17, that accounts only for spherical shape, was $z_e = 18.96$. FIG. 3.14 shows that the deviation of z_e in the numerical results from the theory increase as the bubble become more ellipsoidal.

3.3.5 Sustained oscillations

In FIG. 3.15(a) we compare the frequency of the oscillations for $Ca = 5.73 \times 10^{-4}$ against the theoretical prediction, eq. 3.18. The numerical results follow the same trend as the theory; the frequency is inversely proportional to Re. The frequency decreases with Re because of the increase of inertia in comparison to the thermocapillary forces. The discrepancy between the theory and the numerical results is because the theory does not account for the presence of the Poiseuille flow and the bubble deformations. In FIG. 3.15(b) it is shown the amplitude of the oscillations as a function of Re. As Re increases the inertia becomes stronger allowing the bubble to oscillate with higher amplitude. This figure also illustrates that the amplitude grows with an one-half power law with respect to Re.

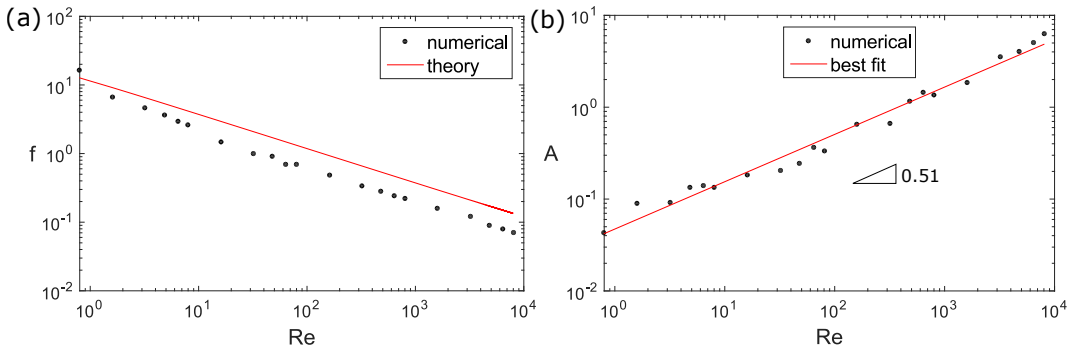

Figure 3.15: (a) Frequency and (b) amplitude of the oscillations in function of the Reynolds number for $Ca = 5.73 \times 10^{-4}$.

3.4 Conclusion

A numerical investigation by means of DNS on the thermocapillary propulsion of bubbles in non-isothermal self rewetting liquids was performed. The effect of the Reynolds and capillary numbers on the bubble dynamics was investigated and a map was built showing the regions of four distinct behaviours: i) 'counter-current propulsion' where the bubble moves against the flow and asymptotically approach the equilibrium position staying stationary; ii) 'damped oscillations' where the bubble moves against the flow and oscillates before stay stationary at the equilibrium position; iii) 'sustained oscillations' where the bubble presents steady oscillations around its equilibrium position after the transient counter-current motion; and iv) 'co-current migration' where the bubble moves in the flow direction and stop at an equilibrium position away from its initial position.

The results were compared against the theoretical prediction for the equilibrium position and the frequency of the oscillations. The results confirm the theoretical prediction showing that the equilibrium position increases linearly with the capillary number. Our results indicate that the transition to sustained oscillations depends only on the capillary number for a large part of the map and only for high Reynolds numbers it starts to depend on the Reynolds number as well. It was also observed that the frequency of theses oscillations is inversely proportional to the Reynolds number while its amplitude of the oscillations increase with an one-half power law with respect to the Reynolds number. Chapter 4 presents experiments that validate these results.

Chapter 4

Experiments on thermocapillary propulsion of bubbles in self-rewetting liquids

This chapter presents experiments on thermocapillary migration of bubbles in a horizontal heated channel with constant flow rate and constant temperature gradient using a self-rewetting liquid. Most previous experimental studies on thermocapillary migration of bubbles were performed using ordinary liquids where surface tension decreases linearly with temperature [15, 16, 17, 18, 19, 20, 21, 22, 23, 24, 25]. For that case the variation in surface tension drives the liquid around the bubble to cold temperatures while the bubble is propelled in the opposite direction towards hotter regions of the liquid. As for ordinary liquids, the variation of surface tension is fairly constant leading to a constant migration velocity of the bubble for a given bubble size and a temperature gradient. In the linear case the bubble reference velocity is given by,

$$v = \frac{\sigma_T \nabla T R}{\mu} \tag{4.1}$$

where σ_T is the temperature coefficient of surface tension, ∇T is the temperature gradient imposed in the liquid phase, R is the radius of the bubble, and μ is the dynamic viscosity of the liquid.

However, for self-rewetting liquids where the surface tension has a parabolic dependence on temperature with a well-defined minimum, a different behaviour may be expected. In the previous work by Shanahan & Sefiane [2] it was shown that bubbles generated by boiling in the hot side of a horizontal heated channel migrates against the flow towards cold temperatures in a self-rewetting liquid following an exponential motion decay. This observation is in contrast with the expected behaviour for thermocapillary migration of bubbles in ordinary liquids.

In order to gather experimental data on this problem, an experimental apparatus is designed to analyse the thermocapillary migration of bubbles in a self-rewetting liquid inside a horizontal channel with constant flow rate and constant temperature gradient. This allows to investigate the effect of the temperature gradient and the flow rate on the bubble dynamics. The results of these experiments are also used to support the findings of the numerical work presented in Chapter 3 of this Thesis.

4.1 Experimental Set-up

An experimental apparatus was designed to capture the thermocapillary motion of bubbles inside a horizontal circular channel with constant flow rate and a constant temperature gradient in the flow direction using a self-rewetting liquid which is a mixture of water and butanol. A schematic of the experimental set-up is presented in FIG. 4.1. The test section consists of a channel made of borosilicate glass and has dimensions of 4 mm diameter and 100 mm length. The exterior of the channel is coated with a transparent and conductive thin layer of tantalum that allows to generate the heat flux while maintaining the interior of the channel visible. The coated channel has an emissivity ε of approximately 0.78 [79]. Two

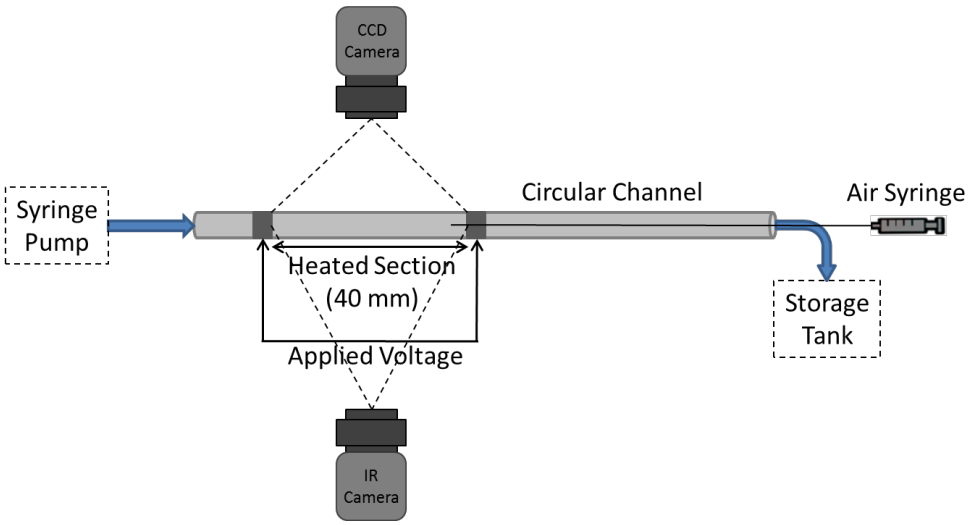

Figure 4.1: Schematic diagram of the test section.

crocodile clamps are attached to the surface of the channel with a distrance of 40 mm between each other and connected to a DC power supply (Kikusui PMX350-0.2A DC Power Supply), enabling heating the 40 mm section of the channel by passing a current through the resistive coating. The channel is connected to a syringe pump (Kd Scientific, KDS 100 LEGACY SYRINGE PUMP) by a plastic tube allowing to control the liquid flow rate and the exit of the channel is connected to a glass beaker where the working fluid is collected. To inject the bubbles, a very small plastic tube with 0.1 mm of interior diameter is placed in the downstream side of the channel and connected to a syringe controlled by a manual microinjector. Small air bubbles (D $\sim$ 0.2 mm) are injected in the downstream side of the channel (hot side) while a constant flow rate is maintained from left to right inside the channel and a constant temperature gradient in the same direction along the channel surface. The temperature gradient is the result of uniform heating of the wall and flow through the channel. The motion of bubbles is captured from the top by a CCD camera (USB3.0 Compact CMOS Camera STC-MBCM401U3V-NIR) and the temperature at the channel surface is captured from the side by an IR camera (FLIR, SC4000). The experimental apparatus is presented in FIG. 4.2. The working fluid used is a 5% wt. butanol/water mixture.

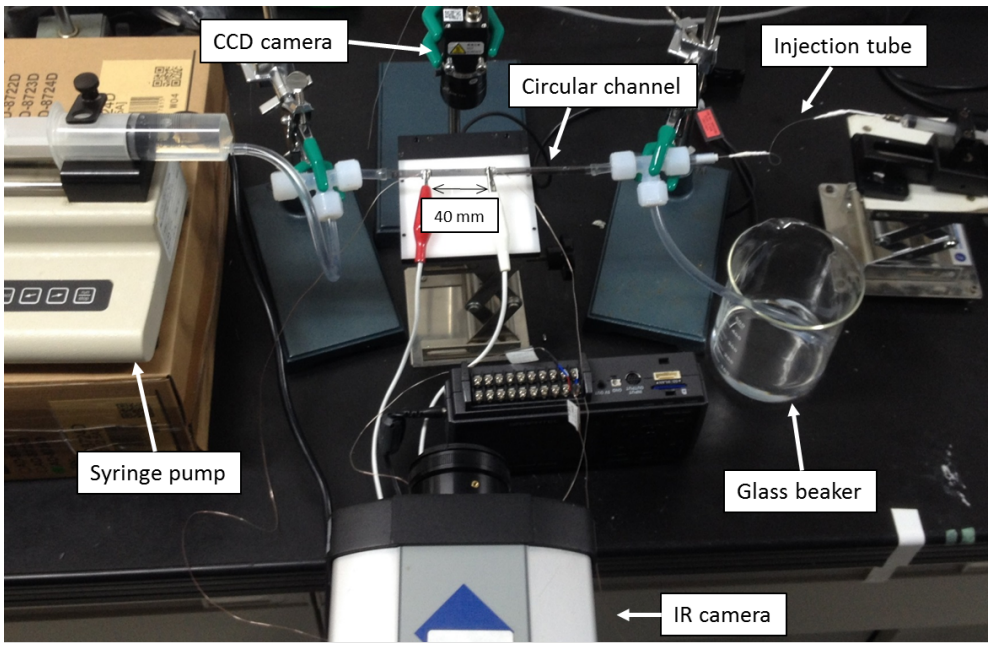

Figure 4.2: The experimental apparatus designed to analyse the motion of bubbles inside a heated circular channel with constant flow rate.

The accuracy of the equipments used in this experiment is presented in Table 4.1.

The bubble motion is captured by a CCD camera mounted above the channel facing downwards and it is recording at 25 frames per second. The CCD camera is connected to a dedicated computer and the images are recorded using the software StCamSWare. A cold light is placed below the channel to improve the video's contrast without affect the temperature of the channel. The records are analysed with ImageJ to measure the bubble position over time and the bubble size. The temperature of the channel is recorded from the side using an IR camera. The IR camera is connected to a computer and the images are recorded using the software ThermaCAM Researcher. After the temperature of the channel stabilise, a snapshot of the recording is taken and a CSV file containing the temperature at each pixel is saved to be post-processed in Matlab.

Equipament	Uncertainty
Syringe pump	$\pm 1\%$
IR-camera	$\pm 2\%$
Power supply	$\pm 2\%$

Table 4.1: Uncertainty of the equipments.

Before every new experimental run, the channel is completely emptied to remove all bubbles from inside glass surface and the liquid is slowly pumped inside the channel using the syringe pump in order to avoid the presence of any bubbles within the channel. After that, the DC power supply is turned on and the voltage is adjusted to obtain the desired temperature at the channel surface. During the first 3 minutes, the channel starts to heat up until the temperature along the channel stabilises and the temperature gradient is generated. Following this, further 5 minutes is allowed to make sure that the temperature in the liquid has stabilised. Then a snapshot of the temperature field is taken using the IR-camera, the CCD camera starts to record and then a single bubble is injected using the manual microinjector and its motion is recorded until it stops. This procedure is repeated for every experimental run.

4.2 Results

This section presents the results on thermocapillary propulsion of bubbles in self-rewetting liquids. First, a typical thermocapillary propulsion of a bubble is shown and then the trajectories of bubbles for different flow rates and temperature gradients is presented. The experimental data are superimposed on the map previously generated by simulations and finally the effects of flow rate and temperature gradient on bubble velocity are discussed.

4.2.1 Typical thermocapillary propulsion

The motion of bubbles inside a horizontal circular channel with constant flow rate flowing from left to right and constant temperature gradient in the same direction is investigated for different flow rates and temperature gradients using a 5% wt. butanol/water mixture, see Table 4.2. Under these conditions three main forces are acting on the bubble. The viscous drag force due to the liquid flow will be

pushing the bubble in the flow direction, the thermocapillary force will drive the bubble in the opposite direction of the local surface tension gradient and the buoyancy force will drive the bubble upwards. As pointed out by Bratukhin & Zuev [25] a necessary condition for bubble motion in the horizontal direction is the presence of a thin liquid film between the bubble and the top wall. This prevents the creation of a contact line that will make the bubble stick to the wall. To this end small bubbles are used in order to minimize the effect of gravity and reduce the buoyancy force acting on the bubble. The size of bubble diameter used in this experiment ranges from $D_b = 0.15\ mm$ to $D_b = 0.27\ mm$.

In ordinary fluids, surface tension has a linearly decreasing dependence on temperature. This makes the thermocapillary stresses drive the fluid around the bubble to cold temperatures while the bubble is propelled in the opposite direction towards the hot temperatures. However, in self-rewetting liquids surface tension has a parabolic dependence on temperature with a well defined minimum. Therefore, when the bubble is at temperatures higher than that corresponding to the surface tension minimum, the surface tension gradient is positive and the thermocapillary stresses drive the fluid around the bubble to the hot temperatures while the bubble is propelled to the cold temperatures towards the surface tension minimum. The reader should note that at the surface tension minimum, the surface tension gradient is zero and the thermocapillary forces acting on the bubble

Re	$Q(ml/min)$	$\Delta V(V)$	$\Delta T(^oC)$
5.96	0.5	70	~ 33
5.96	0.5	80	~ 35
11.93	1	80	~ 29
11.93	1	90	~ 37
11.93	1	100	~ 45
17.90	1.5	90	~ 32
17.90	1.5	100	~ 40
17.90	1.5	110	~ 48
23.86	2	110	~ 40
23.86	2	120	~ 48

Table 4.2: Experimental conditions.

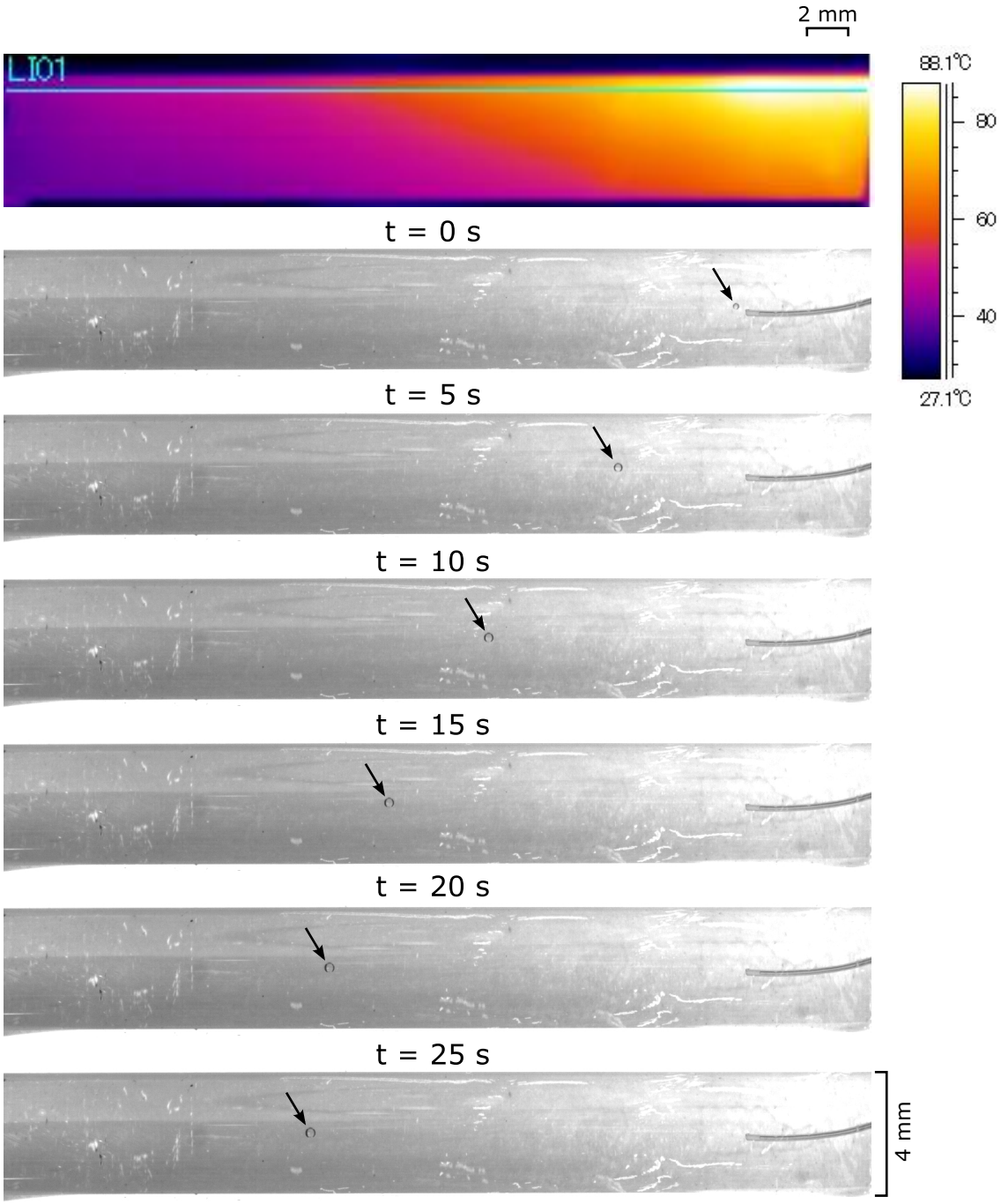

Figure 4.3: Sequence of images taken at every 5 s showing the motion of a bubble with initial diameter of 0.25 mm through a heated circular channel with constant flow rate, $Q = 1.5\ ml/min$, from left to right and constant temperature gradient, $\beta = 1.15\ K/mm$ ($\Delta T = 46\ ^oC$), in the same direction. On top it is shown the temperature along the channel wall taken by the IR-camera before the injection of the bubble.

vanish there. Therefore the bubble should stop as it approaches the surface tension minimum. Under current experimental conditions, the equilibrium position of the bubble will be one in which the fluid drag force and thermocapillary force balance.

A typical thermocapillary migration of a bubble under the conditions stated before is illustrated in FIG. 4.3. After the temperature gradient stabilises with a value of $\beta = 1.15K/mm(\Delta T = 46\ ^oC)$, the bubble is injected on the hot side where the surface tension gradient is positive and the wall temperature is around 83 ^oC (where the cold side is around 40 ^oC). The thermocapillary forces drive the bubble against the flow and it migrates until it stops near surface tension minimum at a wall temperature around 55 ^oC. In the literature, many studies measured surface tension of self-rewetting liquids as a function of the temperature using different techniques and for the 5% wt. water/butanol mixture some of these studies found a surface tension minimum around 70 ^oC (Vochten & Petre [47], Savino et. al. [43], Shanahan & Sefiane [2]), while others found it around 50 ^oC (Savino et. al. [42], Wu et. al. [80], Naresh et. al. [81]). The later case is in better agreement with our findings considering that the bubble should stop before reaching the surface tension minimum as beyond that point there are no forces to oppose the viscous drag force of the fluid flow.

The axial position of the bubble with respect to the liquid inlet over the time for different flow rates and temperature gradients are presented in FIG 4.4. It can be seen from this figure that for lower flow rates, $Q = 0.5\ (ml/min)$ and $Q = 1\ (ml/min)$, the bubble presents a linear motion while for higher flow rates, $Q = 1.5\ (ml/min)$ and $Q = 2\ (ml/min)$, the motion of the bubble follows an exponential decay. This is due to the fact that as the flow rate increases the temperature gradient deviates from linear and the slope becomes greater at high temperatures and lower at low temperatures. It can also be noted that as the flow rate is increased the bubble migrates to lower temperatures. This is because the

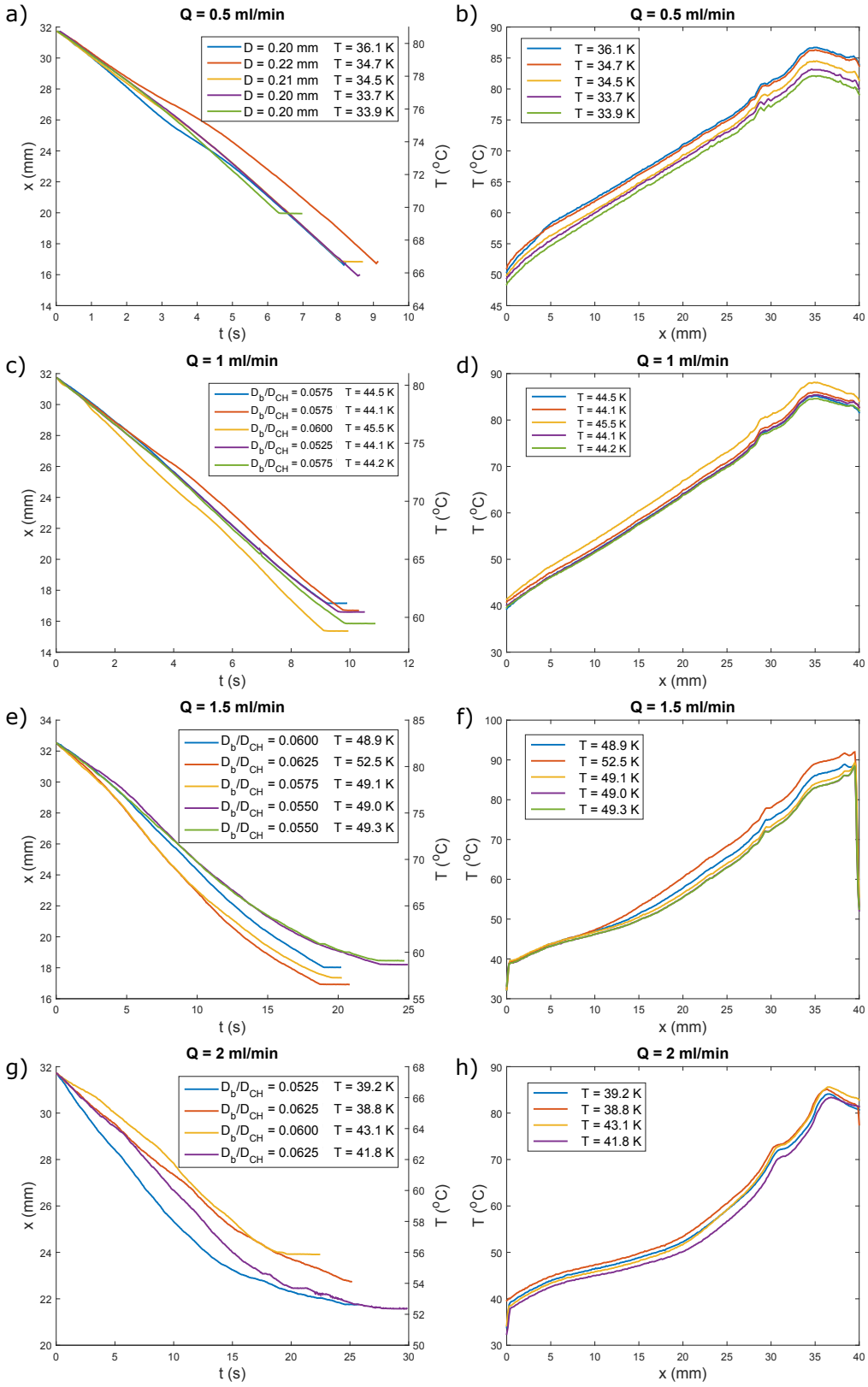

Figure 4.4: Time evolution of the bubble position (left) and temperature along the wall (right) for different flow rates and temperature gradients, where D_b/D_{CH} is the ratio between the bubble diameter and channel diameter and ΔT is the temperature difference between the inlet and outlet. The experimental error in the position is $\pm 0.02\ mm$ and in the temperature is $\pm 1\ ^oC$.

higher flow rates promote the existence of the thin liquid layer between the bubble and the wall allowing the bubble to reach closer to the surface tension minimum before adhering to the wall. In FIG. 4.5 it can be seen all the experimental data are superimposed on the map previously generated via simulations. All the data fall in the region where the simulations predict a counter-current motion followed by sustained oscillations. However no oscillations were observed in the experiments after the counter-current motion. A possible reason for this is the fact that only small bubbles, $D_b \sim 0.2\ mm$, were used in this experiment. In a previous work by Shanahan & Sefiane [2] these oscillations were only observed for big bubbles, $D > 2\ mm$.

4.2.2 Effect of temperature gradient

The temperature gradient is the main mechanism in the thermocapillary migration. It will define how fast the surface tension will change across the interface

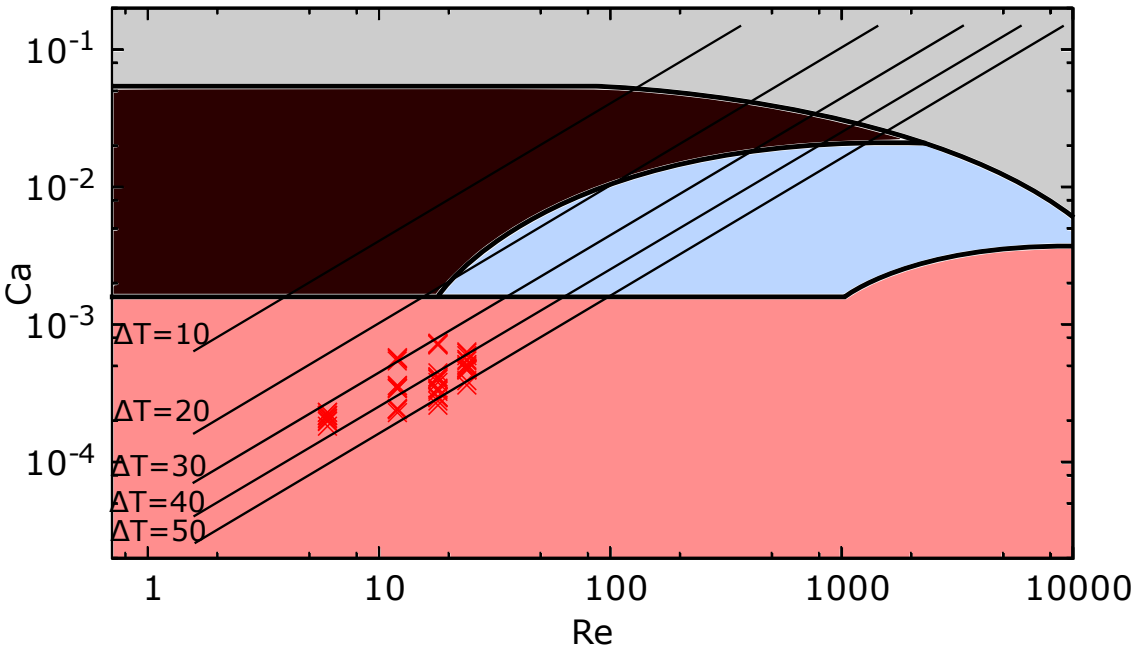

Figure 4.5: Experimental points for different flow rates and temperature gradients on the map generated via simulations with the different regimes of bubble motion: counter-current propulsion (balck), damped oscillations (blue), sustained oscillations (red), and co-current migration (gray).

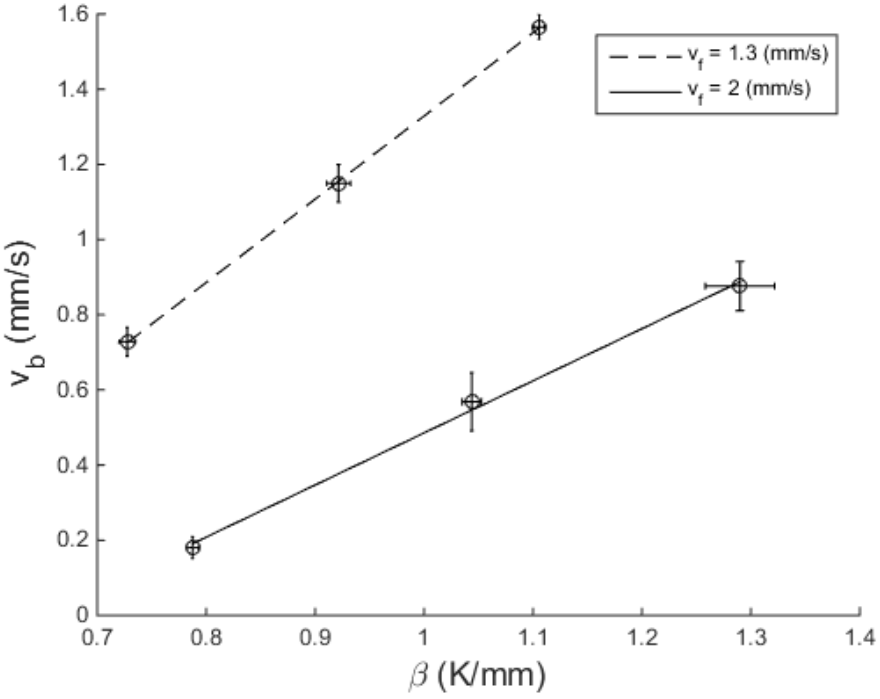

Figure 4.6: Bubble average velocity, v_b as a function of the temperature gradient, β, for $Q = 1\ ml/min$ ($v_f = 1.3\ mm/s$) and $Q = 1.5\ ml/min$ ($v_f = 2\ mm/s$), where v_f is the average flow velocity.

of the bubble and how strong will be the thermocapillary flow.

The effect of the temperature gradient on the average bubble velocity is analysed. The average bubble velocity is calculated taking the total distance travelled by the bubble divided by the time that it takes. In FIG. 4.6 the influence of the temperature gradient, β, on the average bubble velocity, v_b, for different average flow velocities, v_f, is presented, where the average flow velocity is defined as $v_f = Q/A$. The data points are averaged over five experiments and the error bars are calculated using the standard deviation. The figure shows that the average bubble velocity has a linear increase with the temperature gradient for two different flow rates considered, $Q = 1\ (ml/min)$ and $Q = 1.5\ (ml/min)$. It can be seen from FIG. 4.6 that for the lowest flow rate the average bubble velocities are higher due to the weaker viscous drag force and the slope of the the fitted line is also higher. It means that the effect of the temperature gradient on the average bubble velocity is reduced as flow rate is increased.

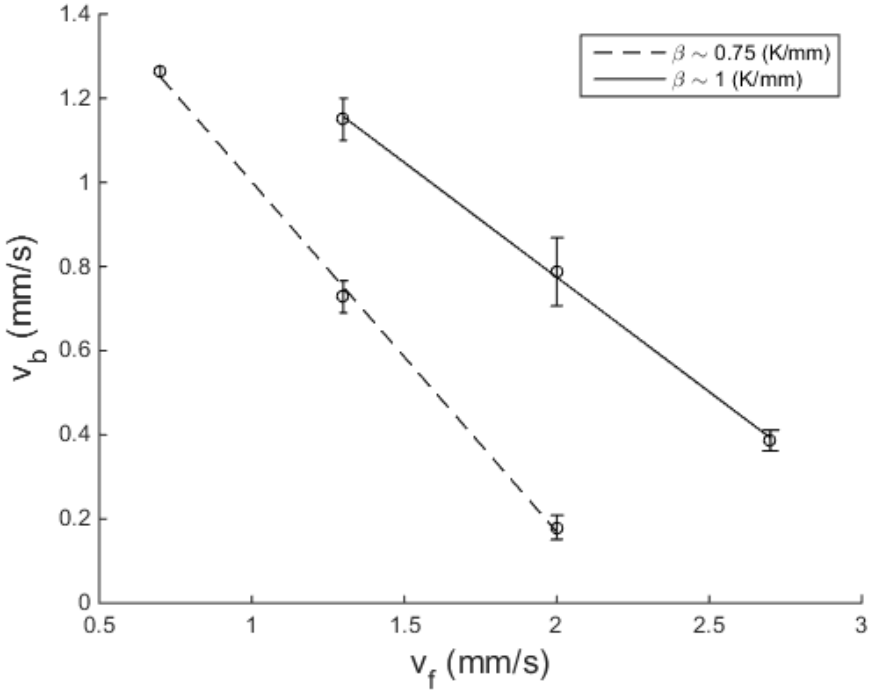

Figure 4.7: Bubble average velocity, v_b, as a function of the flow rate (average flow velocity, v_f) for two temperature gradients, $\beta = 0.75k/mm$ and $\beta = 1K/mm$.

4.2.3 Effect of flow rate

The flow rate is directly related to the viscous drag force acting on the bubble. As the flow rate increases the drag force also increases. Since the drag force is opposing the thermocapillary force in our experimental conditions, the increase in the drag force will slow down the bubble motion.

The effect of the flow rate on the average bubble velocity for two temperature gradients, $\beta \sim 0.75$ (K/mm) and $\beta \sim 1$ (K/mm), is presented in FIG. 4.7. The data points are averaged over five experiments and the error bars are calculated using the standard deviation. In this figure it can be seen that as the flow rate increases the average bubble velocity decreases linearly. The slope of the fitted line corresponding to the lower temperature gradient is higher compared to the higher temperature gradient. This indicates that, as the temperature gradient increases the average bubble velocity is less affected by the increase in the viscous drag force.

4.3 Conclusions

The thermocapillary migration of small bubbles inside a heated horizontal channel with constant flow rate and constant temperature gradient has been examined experimentally using a self-rewetting liquid. An experimental apparatus has been designed to capture the motion of the bubble using a CCD camera and the temperature along the channel wall using an IR-camera.

The results highlight the unusual behaviour of the thermocapillary migration of bubbles in self-rewetting liquids. For all the flow rates and temperature gradients considered in this experiment the bubble migrates against the flow to colder regions of the fluid. This is in contrast with the usual behaviour observed in ordinary fluids where the bubble migrates to higher temperatures.

Testing different flow rates and temperature gradients was possible to analyse how these parameters affect the bubble behaviour. A linear increase in the average bubble velocity when increasing the temperature gradient was observed. This increase in the average bubble velocity was higher for lower flow rates. It was also observed a linear decrease in the average bubble velocity when increasing the flow rate with a higher increase for lower temperature gradients. In this experiments no oscillations were observed after the counter-current motion possibly due to the small size of the bubbles.

Chapter 5

Evaporation of liquid layers comprising binary mixtures

This chapter an analytical model to investigate the stability and dynamics of the evaporation of an horizontal thin liquid layer composed of a binary mixture of volatile liquids heated from below is presented. The long-wave approximation is used to derive the evolution equations for the free interface and the concentration of the components that govern the two-dimensional stability of the layer. The effect of vapour recoil, thermo- and soluto-capillarity and the van der Waals interactions are considered. A linear stability analysis is performed to derive the growth rate of the instabilities for the case of quasi-equilibrium evaporation and non-equilibrium evaporation.

The liquid layer consider here is the one formed around the bubble after the bubble grows and occupies the whole cross section of the tube leaving a thin liquid layer around it.

The developed linear theory describes two modes of instabilities, a monotonic instability mode and an oscillatory instability mode. By means of transient simulations the dependence of these instabilities on the destabilising effects considered is analysed. The transient simulations also help investigate the dynamics in the non-linear regime.

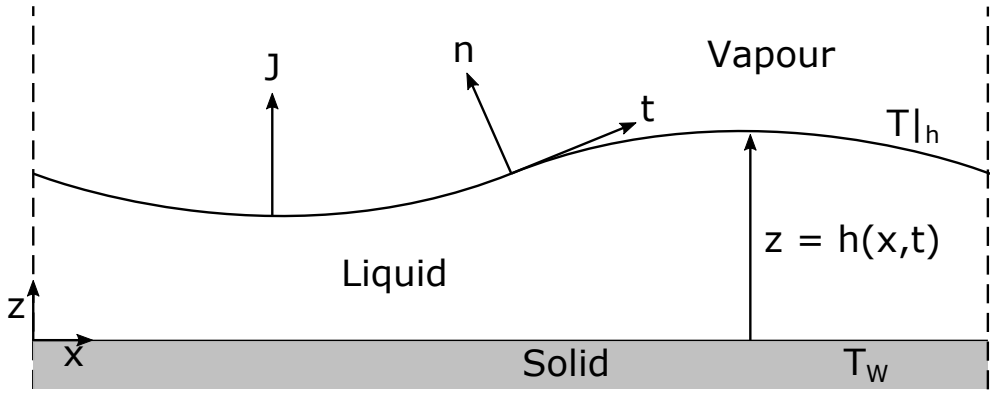

Figure 5.1: Schematic of the physical system describing an evaporating thin liquid film on top of a horizontal heated solid substrate in a periodic domain.

5.1 Problem formulation

The evaporation of a thin liquid layer which consists of a mixture of volatile liquids A and B is investigated. The volatilities of the components are dependent on their respective vapour (saturation) pressures, with the component with highest vapour pressure exhibiting the highest volatility. The mixture is assumed to be ideal while the liquid layer is considered to be Newtonian, with density $\tilde{\rho}$, specific heat capacity $\tilde{c}_p$, thermal conductivity $\tilde{\lambda}$, and viscosity $\tilde{\mu}$, which depend on the local concentration of the two volatile components; the tildes stand for dimensional quantities. The surface tension $\tilde{\sigma}$, also depends on the local concentration as well as the local temperature $\tilde{T}$ (as given by eq. 5.20). The liquid layer is the on top of a horizontal, uniformly heated solid substrate and is in contact with the vapour phase with average bulk temperature $\tilde{T}_g$; the gas consists of the vapour of the binary mixture. It is assumed that, initially, the liquid layer has thickness $\tilde{H}_o$ and width $\tilde{L}_o$. In the present work, it is considered a very thin liquid layer and therefore $\tilde{L}_o$ greatly exceed $\tilde{H}_o$ so that the ratio, $\epsilon = \tilde{H}_o/\tilde{L}_o$, is assumed to be very small. The latter assumption permits the use of lubrication theory, which will be employed below to derive a set of evolution equations that govern the evaporation process.

The Cartesian coordinate system, $(\tilde{x}, \tilde{z})$, is used to model the dynamics and

solve for the velocity field, $\tilde{\mathbf{u}} = (\tilde{u}, \tilde{w})$, where $\tilde{u}$ and $\tilde{w}$ correspond to the horizontal and vertical components of the velocity field, respectively, the temperature field $\tilde{T}$ and the concentration of component A, c; since we deal with a binary mixture the concentration of component B will be given by $1 - c$. The liquid-gas interface is located at $\tilde{z} = \tilde{h}(\tilde{x}, \tilde{t})$ whereas the liquid-solid interface is located at $\tilde{z} = 0$. A sketch of the physical system is presented in FIG. 5.1.

The flow is incompressible and governed by the mass, momentum, energy and concentration conservation equations given by,

$$\tilde{u}_{\tilde{x}} + \tilde{w}_{\tilde{z}} = 0 \tag{5.1}$$

$$\tilde{\rho}(\tilde{u}_{\tilde{t}} + \tilde{u}\tilde{u}_{\tilde{x}} + \tilde{w}\tilde{u}_{\tilde{z}}) = -\tilde{p}_{\tilde{x}} + (\tilde{\mu}\tilde{u}_{\tilde{x}})_{\tilde{x}} + (\tilde{\mu}\tilde{u}_{\tilde{z}})_{\tilde{z}} \tag{5.2}$$

$$\tilde{\rho}(\tilde{w}_{\tilde{t}} + \tilde{u}\tilde{w}_{\tilde{x}} + \tilde{w}\tilde{w}_{\tilde{z}}) = -\tilde{p}_{\tilde{z}} + (\tilde{\mu}\tilde{w}_{\tilde{x}})_{\tilde{x}} + (\tilde{\mu}\tilde{w}_{\tilde{z}})_{\tilde{z}} \tag{5.3}$$

$$\tilde{\rho}((\tilde{c}_p\tilde{T})_{\tilde{t}} + \tilde{u}(\tilde{c}_p\tilde{T})_{\tilde{x}} + \tilde{w}(\tilde{c}_p\tilde{T})_{\tilde{z}}) = (\tilde{\lambda}\tilde{T}_{\tilde{x}})_{\tilde{x}} + (\tilde{\lambda}\tilde{T}_{\tilde{z}})_{\tilde{z}} \tag{5.4}$$

$$c_{\tilde{t}} + \tilde{u}c_{\tilde{x}} + \tilde{w}c_{\tilde{z}} = \tilde{D}_A(c_{\tilde{x}\tilde{x}} + c_{\tilde{z}\tilde{z}}) \tag{5.5}$$

where $\tilde{p}$ is the pressure and $\tilde{D}_i$ is the diffusion coefficient of component i ($i = A, B$). The subscripts $\tilde{x}$, $\tilde{z}$ and $\tilde{t}$ denotes spatial and temporal partial differentiation, respectively.

The dependence of the properties of the liquid layer on the local concentration of the two components can be evaluated using the following rule of mixtures,

$$\tilde{\mu} = c\tilde{\mu}_A + (1 - c)\tilde{\mu}_B \tag{5.6}$$

$$\tilde{\lambda} = c\tilde{\lambda}_A + (1 - c)\tilde{\lambda}_B \tag{5.7}$$

$$\tilde{c}_p = c\tilde{c}_{p,A} + (1 - c)\tilde{c}_{p,B} \tag{5.8}$$

while the density is considered to be constant, $\rho \approx \rho_A \approx \rho_B$, under the assumption that the film is very thin, thus the gravitational effects are negligible.

Along the free surface ($\tilde{z} = \tilde{h}(\tilde{x}, \tilde{t})$), it is necessary to distinguish between the liquid mixture velocity, $\tilde{\mathbf{u}}$ and the velocity of the interface $\tilde{\mathbf{u}}_s = (\tilde{u}_s, \tilde{w}_s)$. If $\mathbf{n} = (-\tilde{h}_x, 1)/(1 + \tilde{h}_x^2)^{1/2}$ is the outward unit normal vector on the interface and

$\tilde{J}$ denotes the total evaporative flux defined as $\tilde{J} = \tilde{J}_A + \tilde{J}_B$ then,

$$\tilde{\mathbf{u}} = \tilde{\mathbf{u}}_s + \frac{\tilde{J}}{\tilde{\rho}}\mathbf{n} \tag{5.9}$$

whilst the tangential components of both velocities, $\tilde{\mathbf{u}}_\tau = \tilde{\mathbf{u}} - (\tilde{\mathbf{u}} \cdot \mathbf{n})\mathbf{n} = \tilde{\mathbf{u}}_s - (\tilde{\mathbf{u}}_s \cdot \mathbf{n})\mathbf{n}$, are the same. Moreover, at $\tilde{z} = \tilde{h}(\tilde{x}, \tilde{t})$ the velocity field satisfies the local mass, force and energy balance in the liquid and gas phase written as,

$$\tilde{J} = \tilde{\rho}(\tilde{\mathbf{u}} - \tilde{\mathbf{u}}_\mathbf{s}) \cdot \mathbf{n} = \tilde{\rho}_v(\tilde{\mathbf{u}}_\mathbf{v} - \tilde{\mathbf{u}}_\mathbf{s}).\mathbf{n} \tag{5.10}$$

$$\frac{\tilde{J}^2}{\tilde{\rho}_v} - \tilde{p} + \mathbf{n} \cdot \underline{\underline{\tilde{\tau}}} \cdot \mathbf{n} = 2\tilde{H}\tilde{\sigma} + \tilde{\Pi} - \tilde{p}_v + \mathbf{n} \cdot \underline{\underline{\tilde{\tau}_v}} \cdot \mathbf{n} \tag{5.11}$$

$$\mathbf{n} \cdot \underline{\underline{\tilde{\tau}}} \cdot \mathbf{t} = \tilde{\nabla}_s\tilde{\sigma} \cdot \mathbf{t} + \mathbf{n} \cdot \underline{\underline{\tilde{\tau}_v}} \cdot \mathbf{t} \tag{5.12}$$

$$\begin{aligned}\tilde{J}_A\tilde{L}_{v,A} + \tilde{J}_B\tilde{L}_{v,B} + \tilde{J}\left[\tfrac{1}{2}[(\tilde{u}_v - \tilde{u}_s) \cdot \mathbf{n}]^2 - \tfrac{1}{2}[(\tilde{u} - \tilde{u}_s) \cdot \mathbf{n}]^2\right] + \tilde{\lambda}\tilde{\nabla}\tilde{T} \cdot \mathbf{n} \\ -\tilde{\lambda}_v\tilde{\nabla}\tilde{T}_v \cdot \mathbf{n} + (\underline{\underline{\tilde{\tau}}} \cdot \mathbf{n}) \cdot (\tilde{\mathbf{u}} - \tilde{\mathbf{u}}_s) - (\underline{\underline{\tilde{\tau}}}_v \cdot \mathbf{n}) \cdot (\tilde{\mathbf{u}}_v - \tilde{\mathbf{u}}_s) = 0\end{aligned} \tag{5.13}$$

Here $\tilde{\rho}_v$, $\tilde{\lambda}_v$, $\tilde{\mathbf{u}}_v$, $\tilde{T}_v$, denote the density, thermal conductivity, velocity field and temperature in the vapour phase, respectively. $\underline{\underline{\tilde{\tau}}}$ denotes the stress tensor, $\tilde{J}_i$ and $\tilde{L}_{v,i}$ denote the evaporative flux and specific internal latent heat of vaporization, respectively, of component i ($i = A, B$). Also, $\mathbf{t} = (1, \tilde{h}_x)/(1 + \tilde{h}_x^2)^{1/2}$ denotes the unit tangential vector on the interface, $2\tilde{H}$ is the mean curvature of the free surface and $\tilde{\nabla}_s$ is the surface gradient operator, respectively defined as,

$$2\tilde{H} = -\tilde{\nabla}_s \cdot \mathbf{n}, \quad \tilde{\nabla}_s = (\mathbf{I} - \mathbf{nn}) \cdot \tilde{\nabla} \tag{5.14}$$

$\tilde{\Pi}$ denotes the disjoining pressure, which accounts for the van der Waals interactions, defined as,

$$\tilde{\Pi} = \frac{A}{6\pi\tilde{h}^3} \tag{5.15}$$

where A is the Hamaker constant.

Along the moving interface ($\tilde{z} = \tilde{h}(\tilde{x}, \tilde{t})$) it is also imposed the boundary condition for the concentration

$$-\tilde{D}_A(\mathbf{n} \cdot \tilde{\nabla}(\tilde{\rho}_A c))_{z=h} + \tilde{\rho}_A c(\tilde{\mathbf{u}} - \tilde{\mathbf{u}}_\mathbf{s}) \cdot \mathbf{n} = \tilde{J}_A \tag{5.16}$$

and the kinematic boundary condition,

$$\tilde{f}(x,z,t) = \tilde{z} - \tilde{h}(x,t), \quad \frac{D\tilde{f}}{D\tilde{t}} = 0 \tag{5.17}$$

$$\tilde{h}_t + \tilde{u}_s \tilde{h}_x - \tilde{w}_s = 0 \tag{5.18}$$

At the liquid-solid interface ($\tilde{z} = 0$), it is set,

$$\tilde{u} = \tilde{w} = 0, \quad \tilde{T} = \tilde{T}_w \tag{5.19}$$

where $\tilde{T}_w$ is the temperature of the heated solid substrate.

To complete the description, a constitutive equation that describes the dependence of the interfacial tension on the local concentration and interfacial temperature is required. To this end, it is employed the following constitutive equation,

$$\tilde{\sigma} = c\tilde{\sigma}_A + (1-c)\tilde{\sigma}_B \tag{5.20}$$

which assumes that the surface tension depends on the local concentration of the two components while we assume the following linear dependence on the temperature [5],

$$\tilde{\sigma}_A = \tilde{\sigma}_{A,o} + \frac{\partial \tilde{\sigma}_A}{\partial \tilde{T}}(\tilde{T}|_h - \tilde{T}_o) \tag{5.21}$$

$$\tilde{\sigma}_B = \tilde{\sigma}_{B,o} + \frac{\partial \tilde{\sigma}_B}{\partial \tilde{T}}(\tilde{T}|_h - \tilde{T}_o) \tag{5.22}$$

Here $\tilde{T}_o$ denotes a reference temperature and $\tilde{\sigma}_{i,o}$ is the surface tension of pure component i ($i = A, B$) at this temperature; we may assume $\tilde{T}_o = \tilde{T}_g$, where $\tilde{T}_g$ is the equilibrium vapour temperature.

Finally, we need to employ a constitutive equation for the evaporation fluxes, $\tilde{J}_i$. To this end, we use the linearized constitutive equation [65],

$$\tilde{J}_i = \tilde{\rho}_{v,i}\tilde{L}_{v,i}\left(\frac{M_i}{2\pi R_g \tilde{T}_g^3}\right)^{1/2}(\tilde{T}|_h - \tilde{T}_g) \tag{5.23}$$

It relates the mass flux $\tilde{J}_i$ of component $i = A, B$ at the interface to the local surface temperature $\tilde{T}|_h$, where M_i is the molecular weight and R_g is the universal

gas constant.

Assuming that the gas phase is an ideal gas it is possible to express the vapour density in terms of the partial pressure, $\tilde{\rho}_{v,i} = \tilde{p}_{v,i} M_i / R_g \tilde{T}_g$. Moreover, using Raoult's law the partial pressure can be related to the mole fraction of each component leading to $\tilde{p}_{v,i} = c_i \tilde{p}_i^o$. Using these relationships the evaporation fluxes can be expressed as,

$$\tilde{J}_i = c_i \tilde{p}_i^o \tilde{L}_{v,i} \left(\frac{M_i^3}{2\pi R_g^3 \tilde{T}_g^5} \right)^{1/2} (\tilde{T}|_h - \tilde{T}_g) \tag{5.24}$$

We assume that the density, viscosity, and thermal conductivity in the liquid phase are all much greater than in the vapour phase. Formally, we take the limits,

$$\frac{\tilde{\rho}_v}{\tilde{\rho}} \to 0, \qquad \frac{\tilde{\mu}_v}{\tilde{\mu}} \to 0, \qquad \frac{\tilde{\lambda}_v}{\tilde{\lambda}} \to 0 \tag{5.25}$$

However, we retain the vapour density in eq. 5.10, where it multiplies the vapour velocity, which may be large.

5.2 Scaling

For the non-dimensionalization of the problem, length is scaled by the initial mean film thickness $\tilde{H}_o$, the viscous scales are used for velocity, time and pressure, the equilibrium vapour temperature $\tilde{T}_g$ is taken as the reference temperature and the properties of component A are taken as reference. The resulting scaling reads,

$$(\tilde{x}, \tilde{z}) = \tilde{H}_o (x, z), \quad (\tilde{u}, \tilde{w}) = \frac{\tilde{\nu}_A}{\tilde{H}_o}(u, w), \quad \tilde{t} = \frac{\tilde{H}_o^2}{\tilde{\nu}_A} t, \quad \tilde{p} = \frac{\tilde{\rho}_A \tilde{\nu}_A^2}{\tilde{H}_o^2} p, \quad \tilde{h} = \tilde{H}_o h,$$

$$\tilde{T} = \tilde{T}_g + \Delta\tilde{T} T, \quad \tilde{J}_i = \frac{\tilde{\lambda}_A \Delta\tilde{T}}{\tilde{H}_o \tilde{L}_{vA}} J_i, \quad (\tilde{\tau}_{xz}, \tilde{\tau}_{ii}) = \frac{\tilde{\rho}_A \tilde{\nu}_A^2}{\tilde{H}_o^2} (\tau_{xz}, \tau_{ii})$$

$$\Delta\tilde{T} = \tilde{T}_w - \tilde{T}_g, \quad \tilde{\rho} \approx \tilde{\rho}_A \approx \tilde{\rho}_B, \quad \tilde{\mu} = \tilde{\mu}_A \mu, \quad \tilde{c}_p = \tilde{c}_{pA} c_p, \quad \tilde{\lambda} = \tilde{\lambda}_A \lambda, \quad \tilde{\sigma} = \tilde{\sigma}_{A,o} \sigma$$

here $\tilde{\nu}_A$ is the kinematic viscosity of component A.

This scaling renders the following non-dimensional system of governing equa-

tions,

$$u_x + w_z = 0 \tag{5.26}$$

$$u_t + uu_x + wu_z = -p_x + (\mu u_x)_x + (\mu u_z)_z \tag{5.27}$$

$$w_t + uw_x + ww_z = -p_z + (\mu w_x)_x + (\mu w_z)_z \tag{5.28}$$

$$Pr[(c_pT)_t + u(c_pT)_x + w(c_pT)_z] = (\lambda T_x)_x + (\lambda T_z)_z \tag{5.29}$$

$$c_t + uc_x + wc_z = Pe^{-1}(c_{xx} + c_{zz}) \tag{5.30}$$

where $Pr = \tilde{\nu}_A/\tilde{\kappa}_A$ is the Prandtl and $Pe = \tilde{\nu}_A/\tilde{D}_A$ the Peclet numbers. Here $\tilde{\kappa}_A$ is the thermal diffusivity of component A.

At the interface $z = h(x,t)$, the scaled mass, energy, normal stress and tangential stress balance are given by,

$$EJ = (-h_x(u - u_s) + w - w_s)(h_x^2 + 1)^{-\frac{1}{2}} \tag{5.31}$$

$$J_A + \Lambda J_B + \frac{E^2}{2\mathcal{L}D^2}J^3 + \lambda(-h_xT_x + T_z)(h_x + 1)^{-\frac{1}{2}} = 0 \tag{5.32}$$

$$p = p_v + \frac{E^2}{D}J^2 - \left(\frac{\delta}{Ca} + \frac{M_cc}{Pr} - \frac{M_T}{Pr}(\delta\Gamma + (1 - \delta\Gamma)c)T\right)\frac{h_{xx}}{(h_x^2 + 1)^{\frac{3}{2}}} - \frac{\mathcal{A}}{h^3} \tag{5.33}$$

$$\mu(2h_x(w_z - u_x) + (1 - h_x^2)(u_z + w_x)) = Ca^{-1}(h_x^2 + 1)^{\frac{1}{2}}(\sigma_x + h_x\sigma_z) \tag{5.34}$$

Here $J = J_A + J_B$ is the total mass flux, $E = \tilde{\lambda}_A\Delta\tilde{T}/\tilde{\rho}_A\tilde{\nu}_A\tilde{L}_{vA}$ is the non-dimensional parameter characterizing the evaporation rate, $\Lambda = \tilde{L}_{vB}/\tilde{L}_{vA}$ is the latent heat ratio of the components, $D = \tilde{\rho}_v/\tilde{\rho}$ is the ratio of vapour to liquid densities, $Ca = \tilde{\rho}_A\tilde{\nu}_A^2/\tilde{\sigma}_{A,o}H_o$ is the capillary number, $M_c = (\tilde{\sigma}_A - \tilde{\sigma}_B)\tilde{H}_o/\tilde{\rho}_A\tilde{\nu}_A\tilde{\kappa}_A$ is the solutal Marangoni number, $M_T = \tilde{\gamma}_A\Delta\tilde{T}\tilde{H}_o/\tilde{\rho}_A\tilde{\nu}_A\tilde{\kappa}_A$ is the thermal Marangoni number, $\mathcal{L} = \tilde{H}_o^2\tilde{L}_{vA}/\tilde{\nu}_A^2$ is a measure of the latent heat of component A, and $\mathcal{A} = A/6\pi\tilde{\rho}_A\tilde{\nu}_A^2\tilde{H}_o$ is the non-dimensional parameter related to the Hamaker constant A.

The scaled boundary condition for the concentration reads,

$$\frac{1}{Pe}\left[\frac{-h_xc_x + c_z}{(h_x^2 + 1)^{\frac{1}{2}}}\right]_{z=h} = E(cJ - J_A) \tag{5.35}$$

The scaled kinematic boundary condition is given by,

$$h_t + uh_x - w_s = 0 \tag{5.36}$$

Using the kinematic boundary condition the mass balance at the interface reads,

$$EJ = (w - h_t - uh_x)(h_x^2 + 1)^{-\frac{1}{2}} \tag{5.37}$$

The scaled constitutive equation for the evaporative flux J is written as,

$$KJ_A = cT \tag{5.38}$$

$$KJ_B = (1 - c)\alpha\beta^{\frac{3}{2}}\Lambda T \tag{5.39}$$

Here $\beta = M_B/M_A$ is the molar ratio of the components and $\alpha = \tilde{p}_B^o/\tilde{p}_A^o$ is the volatility ratio, where $\tilde{p}_i^o$ is the vapour pressure of component $i = A, B$. The parameter K measures the degree of non-equilibrium at the evaporating interface and is defined by [65],

$$K = \frac{\tilde{\lambda}_A}{\tilde{H}_o \tilde{L}_{vA}^2 \tilde{p}_A^o}\left(\frac{2\pi R_g^3 \tilde{T}_g^5}{M_A^3}\right)^{\frac{1}{2}} \tag{5.40}$$

For $K = 0$ it corresponds to the quasi-equilibrium limit, where the temperature at the interface is constant and equal to the equilibrium vapour temperature, $\tilde{T}_g$. For $K^{-1} = 0$ it corresponds to the non-volatile case in which the total evaporative flux J is equal to zero.

	Water	Ethanol
$\rho\,[kg\,m^{-3}]$	971.82	757
$\mu\,[N\,s\,m^{-2}]$	0.351×10^{-3}	0.432×10^{-3}
$\lambda\,[W\,m^{-1}\,K^{-1}]$	0.669	0.169
$c_p\,[J\,kg^{-1}\,K^{-1}]$	4.197×10^3	3.030×10^3
$L_v\,[J\,kg^{-1}]$	2.309×10^6	0.960×10^6
$\sigma\,[N\,m^{-1}]$	62.69×10^{-3}	17.3×10^{-3}
$\gamma\,[N\,m^{-1}\,K^{-1}$	0.17×10^{-3}	0.09×10^{-3}
$M\,[kg\,mol^{-1}]$	18.015×10^{-3}	46.07×10^{-3}
$D\,[m^2\,s^{-1}]$	7.53×10^{-9}	

Table 5.1: Properties for water and ethanol at $80\,^oC$.

$\tilde{H}_o$	$0.1\,\mu m$	$1\,\mu m$	$10\,\mu m$
K	1.543	0.1543	0.0154
Ca	2.02×10^{-2}	2.02×10^{-3}	2.02×10^{-4}
M_T	2.953	29.53	295.28
M_C	78.841	788.41	7.88×10^{3}
$\mathcal{A}$	4×10^{-4}	4×10^{-5}	4×10^{-6}
$\mathcal{L}$	1.77×10^{5}	1.77×10^{7}	1.77×10^{9}
Pr	2.2020		
Pe	47.96		
E	0.0083		
δ	0.276		
α	2.2858		
β	2.5573		
Λ	0.4158		
Γ	1.9184		
Γ_A	0.0271		
Γ_B	0.052		
μ_r	1.2308		
λ_r	0.2526		

Table 5.2: Dimensionless quantities for a 50% water/ethanol mixture.

The scaled surface tension coefficient is given by,

$$\sigma = \delta + (1-\delta)c - \Gamma_A(\delta\Gamma + (1-\delta\Gamma)c)T|_h \tag{5.41}$$

where $\delta = \tilde{\sigma}_{B,o}/\tilde{\sigma}_{A,o}$ is the ratio of the reference surface tension, $\Gamma = \Gamma_B/\Gamma_A$ and $\Gamma_i = \tilde{\gamma}_i/\tilde{\sigma}_{i,o}\Delta\tilde{T}$ is the non-dimensional parameter associated to the temperature coefficient of surface tension, $\tilde{\gamma}_i = -\partial\tilde{\sigma}_i/\partial\tilde{T}$; for the components $i = A, B$.

Table 5.1 shows the properties of water and ethanol at $80\,^oC$ and Table 5.2 shows the dimensionless quantities for a 50% water/ethanol mixture for different thicknesses of the liquid layer. The parameters derived from a liquid layer with $1\,\mu m$ thickness will be the set of base parameters used in this work.

5.3 Base state

In order to perform a linear stability analysis it is necessary to select a base state which will be perturbed with infinitesimal disturbances. As such we select a film

which retains its flat shape as evaporates slowly so that it is possible to consider that the base state is quasi-static. Therefore the base state is time-dependent since the heated film is evaporating; the base state quantities will be denoted by an overbar. As a quasi-static base state with a flat evaporating interface is considered, there is no dependence on the lateral coordinate x and the base state velocity field is zero. Under these assumptions the momentum, energy and concentration conservation equations become,

$$\bar{p}_z = 0 \tag{5.42}$$

$$Pr(c_p\bar{T})_t = (\lambda\bar{T}_z)_z \tag{5.43}$$

$$\bar{c}_t = \frac{\bar{c}_{zz}}{Pe} \tag{5.44}$$

At the interface $z = h(t)$ the energy and the normal stress balance become,

$$\bar{J}_A + \Lambda\bar{J}_B + \frac{E^2}{2\mathcal{L}D^2}\bar{J}^3 = -\lambda\bar{T}_z \tag{5.45}$$

$$\bar{p} - p_v - \frac{E^2\bar{J}^2}{D} + \frac{\mathcal{A}}{\bar{h}^3} = 0 \tag{5.46}$$

there is no shear stress in the base state. The concentration boundary condition becomes,

$$\frac{\bar{c}_z|_{z=\bar{h}}}{Pe} = E(\bar{c}J - J_A) \tag{5.47}$$

The kinematic boundary condition becomes,

$$E\bar{J} = -\bar{h}_t \tag{5.48}$$

while the constitutive equation for the evaporation flux is given by,

$$K\bar{J}_A = \bar{c}\bar{T} \tag{5.49}$$

$$K\bar{J}_B = (1-\bar{c})\alpha\beta^{\frac{3}{2}}\Lambda\bar{T} \tag{5.50}$$

At the solid boundary $z = 0$, the boundary condition is,

$$\bar{T} = 1 \tag{5.51}$$

Since we consider a slowly evaporating film, E is considered to be small and to retain the effect of mass loss in the kinematic boundary condition, time is rescaled on the evaporative scale,

$$t' = Et, \qquad z' = z \tag{5.52}$$

The total mass flux $\bar{J}(t')$ and the liquid temperature $\bar{T}(z', t')$ are considered to be of order unity, while pressure $\bar{p}(t')$ of order E^{-1}. These dependent variables are expanded in power of E,

$$\bar{J_A} = J_{Ao} + EJ_{A1} + E^2 J_{A2} + ... \tag{5.53}$$

$$\bar{J_B} = J_{Bo} + EJ_{B1} + E^2 J_{B2} + ... \tag{5.54}$$

$$\bar{T} = T_o + ET_1 + E^2 T_2 + ... \tag{5.55}$$

$$\bar{p} = E^{-1}(p_o + Ep_1 + E^2 p_2 + ...) \tag{5.56}$$

while the film thickness $\bar{h}(t')$ and the concentration $\bar{c}(t')$ are considered an unspecified order-one function.

We assume $\mathcal{L} \gg 1$ in order to neglect the kinetic energy in the energy balance. D is generally very small since it is simply the ratio of vapour density over the liquid density, thus we consider $D = \bar{D}E^3$ in order to keep the vapour recoil in the normal-stress balance, where $\bar{D}$ is an order one quantity.

Applying the time rescaling and substituting the expansions on the base state, in the small E limit the leading-order base state system becomes

$$p_{o,z'} = 0 \tag{5.57}$$

$$(\lambda T_{o,z'})_{z'} = 0 \tag{5.58}$$

$$\bar{c}_{o,t'} = \frac{\bar{c}_{1,z'}\big|_{z'=\bar{h}}}{\bar{h}} \tag{5.59}$$

$$\text{At } z' = h(t') \quad : \quad J_o = -\bar{h}_{t'} \tag{5.60}$$

$$J_{o,A} + \Lambda J_{o,B} = -\lambda T_{o,z'} \tag{5.61}$$

$$\frac{p_o}{E} = \frac{E^2}{D} J_o^2 \tag{5.62}$$

$$KJ_{o,A} = \bar{c}T_o \tag{5.63}$$

$$KJ_{o,B} = (1-\bar{c})\alpha\beta^{\frac{3}{2}}\Lambda T_o \tag{5.64}$$

$$\bar{c}_{1,z'}|_{z'=\bar{h}} = \bar{c}_o J_o - J_{A,o} \tag{5.65}$$

$$\text{At } z'=0 \qquad : \quad T_o = 1 \tag{5.66}$$

along with the initial condition

$$t' = 0, \qquad \bar{h} = 1 \tag{5.67}$$

The resulting leading-order base state solution is

$$\bar{h} = -\frac{\bar{\lambda}K}{\bar{\Lambda}_2} + \frac{1}{\bar{\Lambda}_2}\sqrt{(\bar{\lambda}K+\bar{\Lambda}_2)^2 - 2\bar{\lambda}\bar{\Lambda}_1\bar{\Lambda}_2 Et} \tag{5.68}$$

$$\bar{T} = 1 - \frac{\bar{\Lambda}_2 z}{\sqrt{(\bar{\lambda}K+\bar{\Lambda}_2)^2 - 2\bar{\lambda}\bar{\Lambda}_1\bar{\Lambda}_2 Et}} \tag{5.69}$$

$$\bar{J}_A = \frac{\bar{\lambda}\bar{c}}{\sqrt{(\bar{\lambda}K+\bar{\Lambda}_2)^2 - 2\bar{\lambda}\bar{\Lambda}_1\bar{\Lambda}_2 Et}} \tag{5.70}$$

$$\bar{J}_B = \frac{\bar{\lambda}(1-\bar{c})\alpha\beta^{\frac{3}{2}}\Lambda}{\sqrt{(\bar{\lambda}K+\bar{\Lambda}_2)^2 - 2\bar{\lambda}\bar{\Lambda}_1\bar{\Lambda}_2 Et}} \tag{5.71}$$

$$\bar{p} = \frac{E^2}{D}\frac{\bar{\Lambda}_2^2\bar{\lambda}^2}{[(\bar{\lambda}K+\bar{\Lambda}_2)^2 - 2\bar{\lambda}\bar{\Lambda}_1\bar{\Lambda}_2 Et]} \tag{5.72}$$

$$\bar{c} = 0.5 \tag{5.73}$$

where,

$$\bar{\lambda} = \bar{c} + (1-\bar{c})\lambda_r \tag{5.74}$$

$$\bar{\Lambda}_1 = \bar{c} + (1-\bar{c})\alpha\beta^{3/2}\Lambda \tag{5.75}$$

$$\bar{\Lambda}_2 = \bar{c} + (1-\bar{c})\alpha\beta^{3/2}\Lambda^2 \tag{5.76}$$

FIG. 5.2 shows the time evolution of the basic state quantities. For $K = 0$ the film thickness goes to zero at $t_D = \frac{\bar{\Lambda}_2}{2\bar{\lambda}\bar{\Lambda}_1 E}$, FIG. 5.2a. The evaporative flux of component A and B are initially $\bar{J}_A = \frac{\bar{\lambda}\bar{c}}{\bar{\Lambda}_2}$ and $\bar{J}_B = \frac{\bar{\lambda}(1-\bar{c})\alpha\beta^{\frac{3}{2}}\Lambda}{\bar{\Lambda}_2}$, respectively, and the most volatile component (component B) has a stronger evaporation flux during the evaporation process, FIG. 5.2b. Both go to infinity at the film dis-

appearance time, t_D, since for $K = 0$ the temperature difference between the interface and the heated substrate is constant during the evaporation process, see FIG. 5.2c. For $K \neq 0$ the film disappearance time is $t_D = \frac{2\bar{\lambda}K+\bar{\Lambda}_2}{2\bar{\lambda}\bar{\Lambda}_1 E}$. The evaporative flux is initially $\bar{J}_A = \frac{\bar{\lambda}\bar{c}}{\bar{\lambda}K+\bar{\Lambda}_2}$ and $\bar{J}_B = \frac{\bar{\lambda}(1-\bar{c})\alpha\beta^{\frac{3}{2}}\Lambda}{\bar{\lambda}K+\bar{\Lambda}_2}$ and increase to $\bar{J}_A = \frac{\bar{c}}{K}$ and $\bar{J}_B = \frac{(1-\bar{c})\alpha\beta^{\frac{3}{2}}\Lambda}{K}$ at the disappearance time. The temperature difference between the interface and the solid substrate is initially $T_W - \bar{T}|_h = \frac{\bar{\Lambda}_2}{\bar{\lambda}K+\bar{\Lambda}_2}$ and decreases to zero as the height of the film become smaller and the temperature at the interface approaches the substrate temperature.

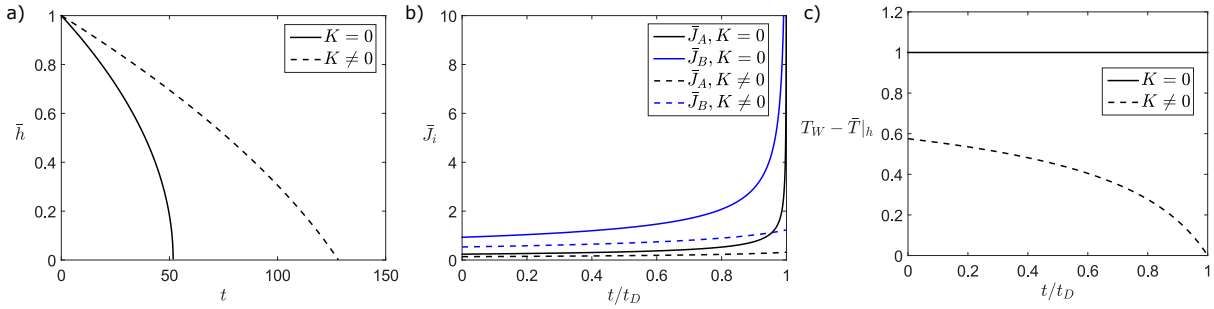

Figure 5.2: Time evolution of a) the height of the flat interface, b) the evaporative flux of components A and B, and c) the temperature difference between the solid substrate and the interface of the liquid layer, for $K = 0$ and $K \neq 0$.

5.4 Long-wave approach

Assuming that the evaporation is a slow process and the horizontal scale of the liquid layer is much larger than the vertical one the long-wave approximation can be applied. To that end the governing system of equations is rescaled using the small parameter $\varepsilon = \tilde{H}_o/\tilde{L}_o$ by writing,

$$X = \varepsilon x, \quad Z = z, \quad \tau = \varepsilon t \tag{5.77}$$

We assume that u, J_A, J_B, T are of order one while w is of order ε in order to preserve continuity and p is of order ε^{-1}. These dependent variables are expanded

in powers of ε,

$$u = U_o + \varepsilon U_1 + ... \tag{5.78}$$

$$w = \varepsilon(W_o + \varepsilon W_1 + ...) \tag{5.79}$$

$$J_A = J_{Ao} + \varepsilon J_{A1} + ... \tag{5.80}$$

$$J_B = J_{Bo} + \varepsilon J_{B1} + ... \tag{5.81}$$

$$T = T_o + \varepsilon T_1 + ... \tag{5.82}$$

$$p = \varepsilon^{-1}(P_o + \varepsilon P_1 + ...) \tag{5.83}$$

For the concentration profile in the vertical direction we consider the rapid diffusion approximation [82, 83, 84], in which the concentration, c, is decomposed into a z-averaged component and a small perturbation incorporating the z dependence,

$$c(X, Z, \tau) = C_o(X, \tau) + \varepsilon^2 Pe^* C_1(X, Z, \tau) \tag{5.84}$$

where $Pe^* = \varepsilon^{-1} Pe$. Since, $\varepsilon^2 Pe^* \ll 1$, the decomposition of c allows to consider a limit in which the vertical concentration gradients are negligible. In the small ε limit, we have the following leading order system of governing equations,

$$U_{o,X} + W_{o,Z} = 0 \tag{5.85}$$

$$P_{o,X} = (\mu U_{o,Z})_Z \tag{5.86}$$

$$P_{o,Z} = 0 \tag{5.87}$$

$$(\lambda T_{o,Z})_Z = 0 \tag{5.88}$$

$$C_{o,\tau} + U_o C_{o,X} = \frac{1}{Pe^*} C_{o,XX} + \frac{1}{h} C_{1,ZZ} \tag{5.89}$$

Along the interface ($Z = h(X, \tau)$), the boundary conditions become,

$$E^* J_o = W_o - h_\tau - U_o h_X \tag{5.90}$$

$$J_{o,A} + \Lambda J_{o,B} = -\lambda T_{o,Z} \tag{5.91}$$

$$P_o = p_v + \frac{E^{*2} J_o^2}{D^*} - \frac{\delta}{Ca^*} h_{XX} - \frac{\mathcal{A}^*}{h^3} \tag{5.92}$$

$$\mu U_{o,Z} = \frac{1}{Pr}[M_c^* C_{o,X} - M_T^*[(1-\delta\Gamma)C_{o,X}T + (\delta\Gamma + (1-\delta\Gamma)C_o)T_X]] \tag{5.93}$$

$$C_{1,Z}|_{Z=h} = E^*(C_o J_o - J_{o,A}) + \frac{h_X C_{o,X}}{Pe^*} \tag{5.94}$$

Since E is considered to be small we assume $E^* = \varepsilon^{-1}E$ to include mass loss in the kinematic boundary condition and $D^* = \varepsilon^{-3}D$ to retain vapour recoil in the normal stress balance. The kinetic energy in the energy balance is neglected by assuming $\mathcal{L} = O(\varepsilon^4)$. We assume $M_T^* = \varepsilon^{-1}M_T$ and $M_c^* = \varepsilon^{-1}M_c$ to retain the thermocapillary and solutal effect in the tangential stress balance. We also assume $Ca^* = \varepsilon^{-3}Ca$ and $\mathcal{A}^* = \varepsilon\mathcal{A}$ to retain the effect of surface tension and disjoining pressure in the normal stress balance, respectively.

At the wall ($Z = 0$), we have,

$$U_o = W_o = 0, \quad T_o = 1 \tag{5.95}$$

The constitutive equation at the leading order reads,

$$KJ_{o,A} = C_o T_o \tag{5.96}$$

$$KJ_{o,B} = (1-C_o)\alpha\beta^{\frac{3}{2}}\Lambda T_o \tag{5.97}$$

The leading order surface tension coefficient is given by,

$$\sigma = \delta + (1-\delta)C_o - \Gamma_A(\delta\Gamma + (1-\delta\Gamma)C_o)T_o|_h \tag{5.98}$$

First, we solve the energy conservation eq. 5.88, subject to the energy balance eq. 5.91 and the wall boundary conditions eq. 5.95 to find the liquid temperature field,

$$T_o = 1 - (J_{o,A} + \Lambda J_{o,B})\frac{Z}{\lambda} \tag{5.99}$$

To find the velocity, we solve x-component of the conservation of momentum eq. 5.86, subject to the tangential stress balance eq. 5.93, and the wall boundary

conditions eq. 5.95,

$$U_o = \frac{P_{o,X}}{\mu}\Big(\frac{Z^2}{2} - hZ\Big) + \frac{[M_c^* C_{o,X} - M_T^*[(1-\delta\Gamma)C_{o,X}T + (\delta\Gamma + (1-\delta\Gamma)C_o)T_X]]Z}{\mu Pr} \tag{5.100}$$

From the conservation of mass eq. 5.85, subject to the wall boundary conditions eq. 5.95, we have,

$$W_o = -\frac{P_{o,XX}}{\mu}\Big(\frac{Z^3}{6} - \frac{hZ^2}{2}\Big) + \frac{P_{o,X}h_X Z^2}{2\mu} - \frac{[M_c^* C_{o,X} - M_T^*[(1-\delta\Gamma)C_{o,X}T + (\delta\Gamma + (1-\delta\Gamma)C_o)T_X]]_X Z^2}{2\mu Pr} \tag{5.101}$$

From the kinematic boundary condition eq. 5.90, and integrating over Z the conservation of concentration, eq. 5.89, together with the boundary condition for the concentration eq. 5.94, we have the following evolution equations,

$$h_\tau = \Big(\frac{P_{o,X}h^3}{3\mu} - \frac{[M_c^* C_{o,X} - M_T^*[(1-\delta\Gamma)C_{o,X}T + (\delta\Gamma + (1-\delta\Gamma)C_o)T_X]]h^2}{2\mu Pr}\Big)_X - E^* J_o \tag{5.102}$$

$$C_{o,\tau} = \Big(\frac{P_{o,X}h^2}{3\mu} - \frac{[M_c^* C_{o,X} - M_T^*[(1-\delta\Gamma)C_{o,X}T + (\delta\Gamma + (1-\delta\Gamma)C_o)T_X]]h}{2\mu Pr}\Big)C_{o,X} + \frac{(hC_{o,X})_X}{hPe^*} + \frac{E^*(C_o J_o - J_{o,A})}{h} \tag{5.103}$$

Returning to the original scaling the evolution equations take the form,

$$h_t = \Big(\frac{p_x h^3}{3\mu} - \frac{[M_c C_x - M_T[(1-\delta\Gamma)C_x T + (\delta\Gamma + (1-\delta\Gamma)C)T_x]]h^2}{2\mu Pr}\Big)_x - EJ \tag{5.104}$$

$$C_t = \Big(\frac{p_x h^2}{3\mu} - \frac{[M_c C_x - M_T[(1-\delta\Gamma)C_x T + (\delta\Gamma + (1-\delta\Gamma)C_o)T_x]]h}{2\mu Pr}\Big)C_x + \frac{(hC_x)_x}{hPe} + \frac{E(CJ - J_A)}{h} \tag{5.105}$$

Next we use the following definitions,

$$\Lambda_1 = \alpha\beta^{3/2}\Lambda + (1 - \alpha\beta^{3/2}\Lambda)C \tag{5.106}$$

$$\Lambda_{1,x} = (1 - \alpha\beta^{3/2}\Lambda)C_x \tag{5.107}$$

$$\Lambda_2 = \alpha\beta^{3/2}\Lambda^2 + (1 - \alpha\beta^{3/2}\Lambda^2)C \tag{5.108}$$

$$\Lambda_{2,x} = (1 - \alpha\beta^{3/2}\Lambda^2)C_x \tag{5.109}$$

$$\delta_o = \delta + (1 - \delta)C \tag{5.110}$$

$$\delta_{o,x} = (1 - \delta)C_x \tag{5.111}$$

$$\Gamma_o = \delta\Gamma + (1 - \delta\Gamma)C \tag{5.112}$$

Using the expressions in Appendix A, the eqs. (5.104) and (5.105) can be written in terms of C and h,

$$h_t = \left[\frac{2\lambda^2E^2h^3}{3\mu D}\left(\frac{\Lambda_1\Lambda_{1,x}}{(\lambda K + \Lambda_2 h)^2} - \frac{\Lambda_1^2}{(\lambda K + \Lambda_2 h)^3}(\Lambda_{2,x}h + \Lambda_2 h_x)\right) - \frac{\delta h^3 h_{xxx}}{3\mu Ca} + \frac{\mathcal{A}h_x}{\mu h} - \frac{h^2}{2\mu Pr}\left(M_c C_x - M_T\left((1 - \delta\Gamma)C_x\left(1 - \frac{\Lambda_2 h}{\lambda K + \Lambda_2 h}\right) - \Gamma_o\left(\frac{\lambda K(\Lambda_{2,x}h + \Lambda_2 h_x)}{(\lambda K + \Lambda_2 h)^2}\right)\right)\right)\right]_x - \frac{E\lambda\Lambda_1}{\lambda K + \Lambda_2 h} \tag{5.113}$$

$$C_t = \left[\frac{2\lambda^2E^2h^2}{3\mu D}\left(\frac{\Lambda_1\Lambda_{1,x}}{(\lambda K + \Lambda_2 h)^2} - \frac{\Lambda_1^2}{(\lambda K + \Lambda_2 h)^3}(\Lambda_{2,x}h + \Lambda_2 h_x)\right) - \frac{\delta h^2 h_{xxx}}{3\mu Ca} + \frac{\mathcal{A}h_x}{\mu h^2} - \frac{h}{2\mu Pr}\left(M_c C_x - M_T\left((1 - \delta\Gamma)C_x\left(1 - \frac{\Lambda_2 h}{\lambda K + \Lambda_2 h}\right) - \Gamma_o\left(\frac{\lambda K(\Lambda_{2,x}h + \Lambda_2 h_x)}{(\lambda K + \Lambda_2 h)^2}\right)\right)\right)\right]C_x + \frac{(hC_x)_x}{hPe} + \frac{E\lambda}{h}\frac{(\Lambda_1 - 1)C}{(\lambda K + \Lambda_2 h)} \tag{5.114}$$

5.5 Linear stability analysis

5.5.1 Quasi-equilibrium evaporation ($K = 0$)

We consider first the quasi-equilibrium case, so the interfacial temperature is constant and equal to the equilibrium temperature. In this case there is no thermocapillary effect and the solutal Marangoni effect is the main mechanism of instability. For $K = 0$, eqs. 5.113 and 5.114 take the form,

$$h_t = \left[\frac{2\lambda^2 E^2}{3\mu D}\left(\frac{\Lambda_1\Lambda_{1,x}h}{\Lambda_2^2} - \frac{\Lambda_1^2}{\Lambda_2^3}(\Lambda_{2,x}h + \Lambda_2 h_x)\right) - \frac{\delta h^3 h_{xxx}}{3\mu Ca} + \frac{\mathcal{A}h_x}{\mu h} - \frac{h^2 M_c C_x}{2\mu Pr}\right]_x - \frac{E\lambda}{h}\frac{\Lambda_1}{\Lambda_2} \tag{5.115}$$

$$C_t = \left[\frac{2\lambda^2 E^2}{3\mu D}\left(\frac{\Lambda_1\Lambda_{1,x}}{\Lambda_2^2} - \frac{\Lambda_1^2}{\Lambda_2^3 h}(\Lambda_{2,x}h + \Lambda_2 h_x)\right) - \frac{\delta h^2 h_{xxx}}{3\mu Ca} + \frac{\mathcal{A}h_x}{\mu h^2} - \frac{hM_c C_x}{2\mu Pr}\right]C_x + \frac{(hC_x)_x}{hPe} + \frac{E\lambda}{h^2}\frac{(\Lambda_1 - 1)C}{\Lambda_2} \tag{5.116}$$

Considering the linear stability of this state, we perturb the base state in the following form,

$$h(x,\tau) = h_b(\tau) + H(\tau)e^{ikx} \tag{5.117}$$

$$C(x,\tau) = C_b + C_1(\tau)e^{ikx} \tag{5.118}$$

where k is the wavenumber. The base solution for h and C, eq. 5.68 and 5.73, can be written as,

$$h_b = \sqrt{1 - \frac{\Lambda_{1b}}{\Lambda_{2b}}2E\lambda t}, \qquad C_b = 0.5 \tag{5.119}$$

where $\Lambda_{1b} = \alpha\beta^{3/2}\Lambda + (1 - \alpha\beta^{3/2}\Lambda)C_b$ and $\Lambda_{2b} = \alpha\beta^{1/3}\Lambda^2 + (1 - \alpha\beta^{3/2}\Lambda^2)C_b$.

Substituting the perturbed solution, eqs. (5.117) and (5.118) into the system of equations, eqs. (5.115) and (5.116), we obtain the following linear system,

$$\begin{aligned}\dot{H} + \left[-\frac{E\lambda_b\Lambda_{1b}}{h_b^2\Lambda_{2b}} - \left(\frac{2\lambda_b^2E^2\Lambda_{1b}^2}{3\mu_b D\Lambda_{2b}^2} - \frac{\mathcal{A}}{\mu_b h_b}\right)k^2 + \frac{\delta h_b^3}{3\mu_b Ca}k^4\right]H \\ + \left[-\frac{E\lambda_b}{h_b}\left(\frac{\Lambda_{1b}(1-\alpha\beta^{\frac{3}{2}}\Lambda^2) - (1-\alpha\beta^{\frac{3}{2}}\Lambda)\Lambda_{2b}}{h_b\Lambda_{2b}^2}\right)\right. \\ \left. + \left(\frac{2\lambda_b^2E^2}{3\mu_b D}\left(\frac{\Lambda_{1b}(1-\alpha\beta^{\frac{3}{2}}\Lambda)h_b}{\Lambda_{2b}^2} - \frac{\Lambda_{1b}^2(1-\alpha\beta^{\frac{3}{2}}\Lambda^2)}{\Lambda_{2b}^3}\right) - \frac{h_b^2M_c}{2\mu_b Pr}\right)k^2\right]C_1 = 0\end{aligned} \tag{5.120}$$

$$\begin{aligned}\dot{C}_1 + \left[\frac{E\lambda_b 2(\Lambda_{1b}-1)C_b}{\Lambda_{2b}h_b^3}\right]H \\ + \left[\frac{E\lambda_b}{h_b^2}\left(\frac{(\Lambda_{1b}-1)C_b(1-\alpha\beta^{3/2}\Lambda^2)}{\Lambda_{2b}^2} - \frac{\Lambda_{1b}-1+(1-\alpha\beta^{3/2}\Lambda)C_b}{\Lambda_{2b}}\right) + \frac{k^2}{Pe}\right]C_1 = 0\end{aligned} \tag{5.121}$$

where $\mu_b = \mu_r + (1-\mu_r)C_b$, $\lambda_b = \lambda_r + (1-\lambda_r)C_b$ and $\delta_b = \delta + (1-\delta)C_b$, and μ_r and λ_r are the viscosity and thermal conductivity ratios, respectively.

Below we use the frozen interface approximation [], which assumes that the characteristic time of the change of the layer thickness is large compared to the development of the disturbances. This allows to disregard the dependence of h_b and τ considering it as a constant parameter. In this case, we consider the following disturbances,

$$H(\tau) = H(0)e^{r\tau}, \quad C_1(\tau) = C_1(0)e^{r\tau} \tag{5.122}$$

where r denotes the growth rate of the disturbances and $H(0)$, $C_1(0)$ the imposed disturbance, we get the following set of equations,

$$\begin{aligned}\left[r - \frac{E\lambda_b\Lambda_{1b}}{h_b^2\Lambda_{2b}} - \left(\frac{2\lambda_b^2E^2\Lambda_{1b}^2}{3\mu_bD\Lambda_{2b}^2} - \frac{\mathcal{A}}{\mu_bh_b}\right)k^2 + \frac{\delta h_b^3}{3\mu_bCa}k^4\right]H \\ + \left[-\frac{E\lambda_b}{h_b}\left(\frac{\Lambda_{1b}(1-\alpha\beta^{\frac{3}{2}}\Lambda^2) - (1-\alpha\beta^{\frac{3}{2}}\Lambda)\Lambda_{2b}}{h_b\Lambda_{2b}^2}\right)\right. \\ \left. + \left(\frac{2\lambda_b^2E^2}{3\mu_bD}\left(\frac{\Lambda_{1b}(1-\alpha\beta^{\frac{3}{2}}\Lambda)h_b}{\Lambda_{2b}^2} - \frac{\Lambda_{1b}^2(1-\alpha\beta^{\frac{3}{2}}\Lambda^2)}{\Lambda_{2b}^3}\right) - \frac{h_b^2M_c}{2\mu_bPr}\right)k^2\right]C_1 = 0\end{aligned} \tag{5.123}$$

$$\begin{aligned}&\left[\frac{E\lambda_b 2(\Lambda_{1b}-1)C_b}{\Lambda_{2b}h_b^3}\right]H \\ &+\left[r+\frac{E\lambda_b}{h_b^2}\left(\frac{(\Lambda_{1b}-1)C_b(1-\alpha\beta^{3/2}\Lambda^2)}{\Lambda_{2b}^2} - \frac{\Lambda_{1b}-1+(1-\alpha\beta^{3/2}\Lambda)C_b}{\Lambda_{2b}}\right)+\frac{k^2}{Pe}\right]C_1 = 0\end{aligned} \tag{5.124}$$

Taking the determinant of the Jacobian of the system equal to zero, renders the expressions for the growth rate r as a function of the wavenumber k, viz,

$$\begin{aligned}r_\pm = \frac{1}{2}\left[\frac{E\lambda_b\Lambda_{1b}}{h_b^2\Lambda_{2b}} + \left(\frac{2\lambda_b^2E^2\Lambda_{1b}^2}{3\mu_bD\Lambda_{2b}^2} - \frac{\mathcal{A}}{\mu_bh_b}\right)k^2 - \frac{\delta h_b^3}{3\mu_bCa}k^4\right. \\ \left. -\frac{E\lambda_b}{h_b^2}\left(\frac{(\Lambda_{1b}-1)C_b(1-\alpha\beta^{3/2}\Lambda^2)}{\Lambda_{2b}^2} - \frac{\Lambda_{1b}-1+(1-\alpha\beta^{3/2}\Lambda)C_b}{\Lambda_{2b}}\right) - \frac{k^2}{Pe}\right] \pm \frac{1}{2}\sqrt{\mathcal{D}_1}\end{aligned} \tag{5.125}$$

where,

$$\begin{aligned}\mathcal{D}_1 = \Bigg[&- \frac{E\lambda_b\Lambda_{1b}}{h_b^2\Lambda_{2b}} - \left(\frac{2\lambda_b^2E^2\Lambda_{1b}^2}{3\mu_bD\Lambda_{2b}^2} - \frac{\mathcal{A}}{\mu_bh_b}\right)k^2 + \frac{\delta h_b^3}{3\mu_bCa}k^4 \\ &+ \frac{E\lambda_b}{h_b^2}\left(\frac{(\Lambda_{1b}-1)C_b(1-\alpha\beta^{3/2}\Lambda^2)}{\Lambda_{2b}^2} - \frac{\Lambda_{1b}-1+(1-\alpha\beta^{3/2}\Lambda)C_b}{\Lambda_{2b}}\right) + \frac{k^2}{Pe}\Bigg]^2 \\ &- 4\Bigg[- \frac{E\lambda_b\Lambda_{1b}}{h_b^2\Lambda_{2b}} - \left(\frac{2\lambda_b^2E^2\Lambda_{1b}^2}{3\mu_bD\Lambda_{2b}^2} - \frac{\mathcal{A}}{\mu_bh_b}\right)k^2 + \frac{\delta h_b^3}{3\mu_bCa}k^4\Bigg] \\ &* \left[\frac{E\lambda_b}{h_b^2}\left(\frac{(\Lambda_{1b}-1)C_b(1-\alpha\beta^{3/2}\Lambda^2)}{\Lambda_{2b}^2} - \frac{\Lambda_{1b}-1+(1-\alpha\beta^{3/2}\Lambda)C_b}{\Lambda_{2b}}\right) + \frac{k^2}{Pe}\right] \\ &+ 4\left[\frac{E\lambda_b 2(\Lambda_{1b}-1)C_b}{\Lambda_{2b}h_b^3}\right] * \Bigg[- \frac{E\lambda_b}{h_b}\left(\frac{\Lambda_{1b}(1-\alpha\beta^{\frac{3}{2}}\Lambda^2) - (1-\alpha\beta^{\frac{3}{2}}\Lambda)\Lambda_{2b}}{h_b\Lambda_{2b}^2}\right) \\ &+ \left(\frac{2\lambda_b^2E^2}{3\mu_bD}\left(\frac{\Lambda_{1b}(1-\alpha\beta^{\frac{3}{2}}\Lambda)h_b}{\Lambda_{2b}^2} - \frac{\Lambda_{1b}^2(1-\alpha\beta^{\frac{3}{2}}\Lambda^2)}{\Lambda_{2b}^3}\right) - \frac{h_b^2M_c}{2\mu_bPr}\right)k^2\Bigg] \end{aligned} \quad (5.126)$$

The eq. 5.125 defines the type of instability during the evaporation process. There is two possibilities: a) Two real roots that correspond to the monotonic damping or growth (depending on the sign of the root) of the disturbances: the two roots correspond to the growth rate of the two different modes, i.e. the interfacial and the concentration mode. b) Two complex roots that correspond to the oscillatory instability: the real part of r gives the growth rate and the imaginary part the frequency of the instability.

FIG. 5.3a shows that without evaporation the solution given in eq. 5.125 has real eigenvalues and is stable. In this case the only mechanisms present are capillarity and diffusion which both have a stabilizing effect. With evaporation, FIG. 5.3b, the system has complex eigenvalues and is unstable. In this case the solutal Marangoni effect is present and it leads to an oscillatory instability mode.

5.5.2 Non-equilibrium evaporation ($K \neq 0$)

We now consider the non-equilibrium evaporation, where the interfacial temperature is not constant and depends on the evaporative fluxes.

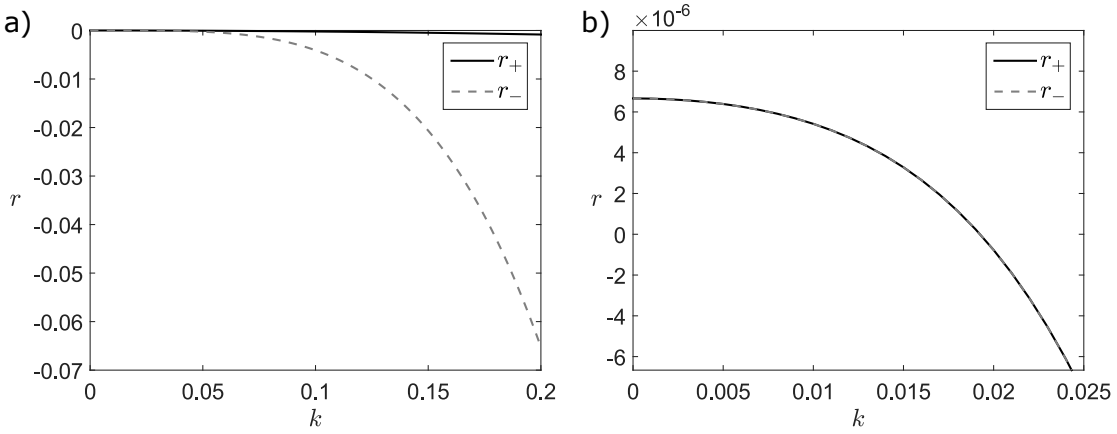

Figure 5.3: Behaviour of growth rates r_+ and r_- versus the wavenumber k, for $K = 0$, with a) $E = 0$ and b) $E = 10^{-5}$. Other parameters are the set of base parameters given in Table 5.2.

Applying the following perturbation,

$$h(x,t) = h_b(t) + H(t)e^{ikx} \tag{5.127}$$

$$C(x,t) = C_b + C_1(t)e^{ikx} \tag{5.128}$$

into the system of equations 5.113 and 5.114 and linearize it with respect to H and C_1, we obtain

$$\begin{aligned}\dot{H} + \Bigg[&- \frac{E\lambda_b\Lambda_{1b}\Lambda_{2b}}{(\lambda_b K + \Lambda_{2b}h_b)^2} - \frac{2\lambda_b^2 E^2 h_b^3 \Lambda_{1b}^2 \Lambda_{2b} k^2}{3\mu_b D(\lambda_b K + \Lambda_{2b}h_b)^3} \\ &+ \frac{\delta h_b^3 k^4}{3\mu_b Ca} + \frac{\mathcal{A}k^2}{\mu_b h_b} - \frac{h_b^2 M_T}{2\mu_b Pr}\frac{\Gamma_b\lambda_b K\Lambda_{2b}k^2}{(\lambda_b K + \Lambda_{2b}h_b)^2}\Bigg] H \\ &+ \Bigg[- \frac{E\lambda_b(\Lambda_{1b}(1-\alpha\beta^{3/2}\Lambda^2)h_b - (1-\alpha\beta^{3/2}\Lambda)(\lambda_b K + \Lambda_{2b}h_b))}{(\lambda_b K + \Lambda_{2b}h_b)^2} \\ &+ \frac{2\lambda_b^2 E^2 h_b^3}{3\mu_b D}\left(\frac{\Lambda_{1b}(1-\alpha\beta^{3/2}\Lambda)}{(\lambda_b K + \Lambda_{2b}h_b)^2} - \frac{\Lambda_{1b}^2 h_b(1-\alpha\beta^{3/2}\Lambda^2)}{(\lambda_b K + \Lambda_{2b}h_b)^3}\right)k^2 \\ &- \frac{h_b^2}{2\mu_b Pr}\left(M_c + M_T\left(-(1-\delta\Gamma)\left(1 - \frac{\Lambda_{2b}h_b}{\lambda_b K + \Lambda_{2b}h_b}\right) + \frac{\Gamma_b h_b \lambda_b K(1-\alpha\beta^{3/2}\Lambda^2)}{(\lambda_b K + \Lambda_{2b}h_b)^2}\right)\right)k^2\Bigg] C_1 = 0\end{aligned} \tag{5.129}$$

$$\dot{C}_1 + \left[E\lambda_b\left(\frac{(\Lambda_{1b}-1)C_b\Lambda_{2b}}{h_b(\lambda_b K + \Lambda_{2b}h_b)^2} + \frac{(\Lambda_{1b}-1)C_b}{h_b^2(\lambda_b K + \Lambda_{2b}h_b)}\right)\right] H$$

$$+\left[E\lambda_b\left(\frac{(\Lambda_{1b}-1)C_b(1-\alpha\beta^{3/2}\Lambda^2)}{(\lambda_bK+\Lambda_{2b}h_b)^2}-\frac{\Lambda_{1b}-1+(1-\alpha\beta^{3/2}\Lambda)C_b}{h_b(\lambda_bK+\Lambda_{2b}h_b)}\right)+\frac{k^2}{Pe}\right]C_1=0 \tag{5.130}$$

Applying the frozen interface approximation, $H(\tau)=H(0)e^{r\tau}$, $C_1(\tau)=C_1(0)e^{r\tau}$, we get the following set of equations,

$$\begin{aligned}&\left[r-\frac{E\lambda_b\Lambda_{1b}\Lambda_{2b}}{(\lambda_bK+\Lambda_{2b}h_b)^2}-\frac{2\lambda_b^2E^2h_b^3\Lambda_{1b}^2\Lambda_{2b}k^2}{3\mu_bD(\lambda_bK+\Lambda_{2b}h_b)^3}\right.\\&\qquad\left.+\frac{\delta h_b^3k^4}{3\mu_bCa}+\frac{\mathcal{A}k^2}{\mu_bh_b}-\frac{h_b^2M_T}{2\mu_bPr}\frac{\Gamma_b\lambda_bK\Lambda_{2b}k^2}{(\lambda_bK+\Lambda_{2b}h_b)^2}\right]H\\&\quad+\left[-\frac{E\lambda_b(\Lambda_{1b}(1-\alpha\beta^{3/2}\Lambda^2)h_b-(1-\alpha\beta^{3/2}\Lambda)(\lambda_bK+\Lambda_{2b}h_b))}{(\lambda_bK+\Lambda_{2b}h_b)^2}\right.\\&\qquad\left.+\frac{2\lambda_b^2E^2h_b^3}{3\mu_bD}\left(\frac{\Lambda_{1b}(1-\alpha\beta^{3/2}\Lambda)}{(\lambda_bK+\Lambda_{2b}h_b)^2}-\frac{\Lambda_{1b}^2h_b(1-\alpha\beta^{3/2}\Lambda^2)}{(\lambda_bK+\Lambda_{2b}h_b)^3}\right)k^2\right.\\&\left.-\frac{h_b^2}{2\mu_bPr}\left(M_c+M_T\left(-(1-\delta\Gamma)\left(1-\frac{\Lambda_{2b}h_b}{\lambda_bK+\Lambda_{2b}h_b}\right)+\frac{\Gamma_bh_b\lambda_bK(1-\alpha\beta^{3/2}\Lambda^2)}{(\lambda_bK+\Lambda_{2b}h_b)^2}\right)\right)k^2\right]C_1=0\end{aligned} \tag{5.131}$$

$$\begin{aligned}&\left[E\lambda_b\left(\frac{(\Lambda_{1b}-1)C_b\Lambda_{2b}}{h_b(\lambda_bK+\Lambda_{2b}h_b)^2}+\frac{(\Lambda_{1b}-1)C_b}{h_b^2(\lambda_bK+\Lambda_{2b}h_b)}\right)\right]H\\&+\left[r+E\lambda_b\left(\frac{(\Lambda_{1b}-1)C_b(1-\alpha\beta^{3/2}\Lambda^2)}{(\lambda_bK+\Lambda_{2b}h_b)^2}-\frac{\Lambda_{1b}-1+(1-\alpha\beta^{3/2}\Lambda)C_b}{h_b(\lambda_bK+\Lambda_{2b}h_b)}\right)+\frac{k^2}{Pe}\right]C_1=0\end{aligned} \tag{5.132}$$

Taking the determinant of the Jacobian of the system equal to zero, renders the expressions for the growth rate r as a function of the wavenumber k, viz,

$$\begin{aligned}r_\pm=\frac{1}{2}\Bigg[&\frac{E\lambda_b\Lambda_{1b}\Lambda_{2b}}{(\lambda_bK+\Lambda_{2b}h_b)^2}+\frac{2\lambda_b^2E^2h_b^3\Lambda_{1b}^2\Lambda_{2b}k^2}{3\mu_bD(\lambda_bK+\Lambda_{2b}h_b)^3}\\&-\frac{\delta h_b^3k^4}{3\mu_bCa}-\frac{\mathcal{A}k^2}{\mu_bh_b}+\frac{h_b^2M_T}{2\mu_bPr}\frac{\Gamma_b\lambda_bK\Lambda_{2b}k^2}{(\lambda_bK+\Lambda_{2b}h_b)^2}\\&-E\lambda_b\left(\frac{(\Lambda_{1b}-1)C_b(1-\alpha\beta^{3/2}\Lambda^2)}{(\lambda_bK+\Lambda_{2b}h_b)^2}-\frac{\Lambda_{1b}-1+(1-\alpha\beta^{3/2}\Lambda)C_b}{h_b(\lambda_bK+\Lambda_{2b}h_b)}\right)-\frac{k^2}{Pe}\Bigg]\pm\frac{1}{2}\sqrt{\mathcal{D}_1}\end{aligned} \tag{5.133}$$

where

$$\mathcal{D}_1=\Bigg[-\frac{E\lambda_b\Lambda_{1b}\Lambda_{2b}}{(\lambda_bK+\Lambda_{2b}h_b)^2}-\frac{2\lambda_b^2E^2h_b^3\Lambda_{1b}^2\Lambda_{2b}k^2}{3\mu_bD(\lambda_bK+\Lambda_{2b}h_b)^3}$$

$$
\begin{aligned}
&+\frac{\delta h_b^3 k^4}{3\mu_b Ca}+\frac{\mathcal{A}k^2}{\mu_b h_b}-\frac{h_b^2 M_T}{2\mu_b Pr}\frac{\Gamma_b\lambda_b K\Lambda_{2b}k^2}{(\lambda_b K+\Lambda_{2b}h_b)^2}\\
&+E\lambda_b\left(\frac{(\Lambda_{1b}-1)C_b(1-\alpha\beta^{3/2}\Lambda^2)}{(\lambda_b K+\Lambda_{2b}h_b)^2}-\frac{\Lambda_{1b}-1+(1-\alpha\beta^{3/2}\Lambda)C_b}{h_b(\lambda_b K+\Lambda_{2b}h_b)}\right)+\frac{k^2}{Pe}\Bigg]^2\\
&-4\Bigg[-\frac{E\lambda_b\Lambda_{1b}\Lambda_{2b}}{(\lambda_b K+\Lambda_{2b}h_b)^2}-\frac{2\lambda_b^2E^2h_b^3\Lambda_{1b}^2\Lambda_{2b}k^2}{3\mu_b D(\lambda_b K+\Lambda_{2b}h_b)^3}\\
&+\frac{\delta h_b^3 k^4}{3\mu_b Ca}+\frac{\mathcal{A}k^2}{\mu_b h_b}-\frac{h_b^2 M_T}{2\mu_b Pr}\frac{\Gamma_b\lambda_b K\Lambda_{2b}k^2}{(\lambda_b K+\Lambda_{2b}h_b)^2}\Bigg]\\
&*\left[E\lambda_b\left(\frac{(\Lambda_{1b}-1)C_b(1-\alpha\beta^{3/2}\Lambda^2)}{(\lambda_b K+\Lambda_{2b}h_b)^2}-\frac{\Lambda_{1b}-1+(1-\alpha\beta^{3/2}\Lambda)C_b}{h_b(\lambda_b K+\Lambda_{2b}h_b)}\right)+\frac{k^2}{Pe}\right]\\
&+4\left[E^*\lambda_b\left(\frac{(\Lambda_{1b}-1)C_b\Lambda_{2b}}{h_b(\lambda_b K+\Lambda_{2b}h_b)^2}+\frac{(\Lambda_{1b}-1)C_b}{h_b^2(\lambda_b K+\Lambda_{2b}h_b)}\right)\right]\\
&*\Bigg[-\frac{E\lambda_b(\Lambda_{1b}(1-\alpha\beta^{3/2}\Lambda^2)h_b-(1-\alpha\beta^{3/2}\Lambda)(\lambda_b K+\Lambda_{2b}h_b))}{(\lambda_b K+\Lambda_{2b}h_b)^2}\\
&+\frac{2\lambda_b^2E^2h_b^3}{3\mu_b D}\left(\frac{\Lambda_{1b}(1-\alpha\beta^{3/2}\Lambda)}{(\lambda_b K+\Lambda_{2b}h_b)^2}-\frac{\Lambda_{1b}^2h_b(1-\alpha\beta^{3/2}\Lambda^2)}{(\lambda_b K+\Lambda_{2b}h_b)^3}\right)k^2\\
&-\frac{h_b^2}{2\mu_b Pr}\left(M_c+M_T\left(-(1-\delta\Gamma)\left(1-\frac{\Lambda_{2b}h_b}{\lambda_b K+\Lambda_{2b}h_b}\right)+\frac{\Gamma_b h_b\lambda_b K(1-\alpha\beta^{3/2}\Lambda^2)}{(\lambda_b K+\Lambda_{2b}h_b)^2}\right)\right)k^2\Bigg]
\end{aligned}
\tag{5.134}
$$

In non-equilibrium evaporation, the interfacial temperature is not constant and the thermal Marangoni effect is present. Without evaporation the initial perturbation is promoted by the thermal Marangoni effect leading to a monotonic instability mode, as shown in FIG. 5.4a. With evaporation, the solutal Marangoni effect is also present and for the parameters considered here it competes with the thermal Marangoni effect leading the system to an oscillatory instability mode, as shown in FIG. 5.4b.

5.5.3 Mechanisms of the instability

A schematic of the main mechanisms of instability is shown in FIG. 5.5. First we discuss the instability for the case of the standard parameters present in Table 5.2 where the component A has lower volatility and higher surface tension than component B. When an initial perturbation is applied to the system the temperature of the interface becomes hotter at the trough due to the proximity

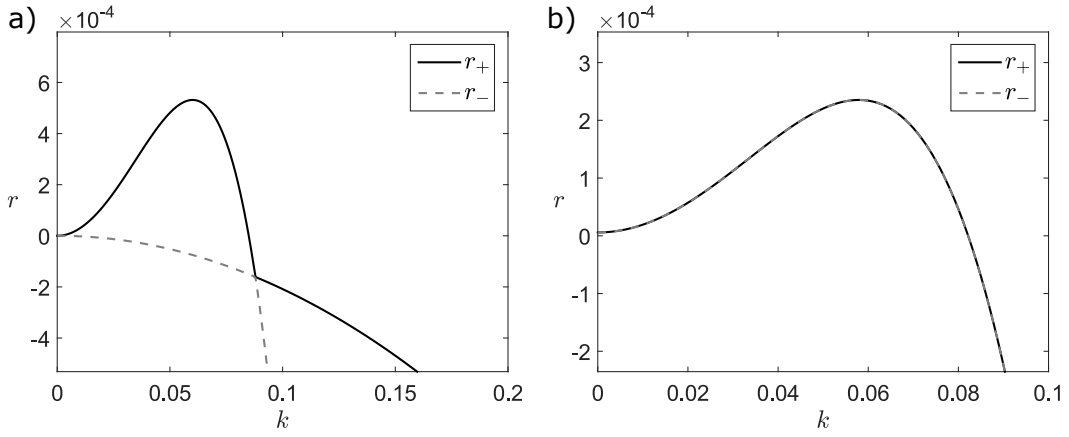

Figure 5.4: Behaviour of growth rates r_+ and r_- versus the wavenumber k, for $K \neq 0$, with a) $E = 0$ and b) $E = 10^{-5}$. Other parameters are the set of base parameters given in Table 5.2.

to the hot substrate. Therefore, the thermal Marangoni effect drives the liquid from the hotter trough in direction to the colder crest promoting the perturbation. However, due to the higher volatility of component B, it evaporates faster at the trough increasing the concentration of component A that has higher surface tension. As the concentration of component A increases at the trough, the solutal Marangoni effect becomes stronger and at some point it may overcome the thermal Marangoni effect and starts to drive the liquid in direction to the trough, as shown in FIG. 5.5a. As a consequence, the interface starts to level until the trough become a crest and the previous crests become troughs. This process repeat causing oscillations at the interface and the evaporation goes through an oscillatory instability mode. However, when component A has higher volatility and higher surface tension than component B the solutal Marangoni effect has the

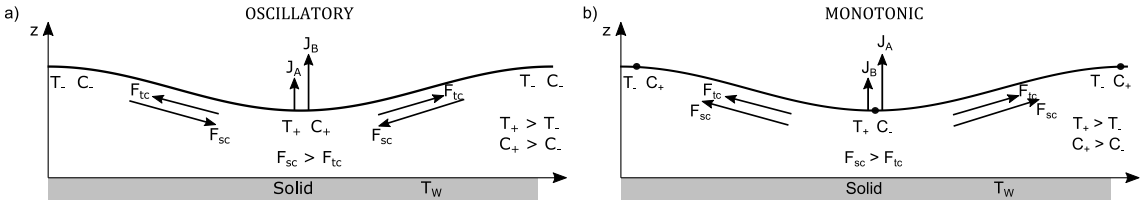

Figure 5.5: a) Schematic of the oscillatory instability for the case where component A is less volatile than B and has higher surface tension. b) Schematic of the monotonic instability for the case where component A is more volatile than B and has higher surface tension.

opposite behaviour. The concentration of component B increases at the trough due to the higher volatility of component A and the solutal Marangoni effect drives the liquid from the trough in direction of the crest, promoting the thermal Marangoni effect, as shown in FIG. 5.5b. In this case the evaporation goes through a monotonic instability mode. Therefore when there is competition between thermal and solutal Marangoni effects the oscillatory instability is possible only when the solutal Marangoni can overcome the effect of thermal Marangoni, while when the thermal and solutal Marangoni effects enhance each other, driving the flow in the same direction, the instability is always monotonic.

5.5.4 Parametric analysis

A parametric analysis on the stability of the evaporating thin liquid layer is performed for the case of $K \neq 0$ in the limit of small evaporation number, $E = 10^{-5}$. In the limit of small evaporation number the main mechanisms of instability during the evaporation are the thermal Marangoni effect and the solutal Marangoni effect. Therefore, the effect of the thermal Marangoni number and the solutal Marangoni number on the growth rate of the instabilities are analysed as well the effect of the volatility of the components.

FIG. 5.6 presents the effect of the thermal Marangoni number on the instability. For lower thermal Marangoni numbers the solutal Marangoni effect dom-

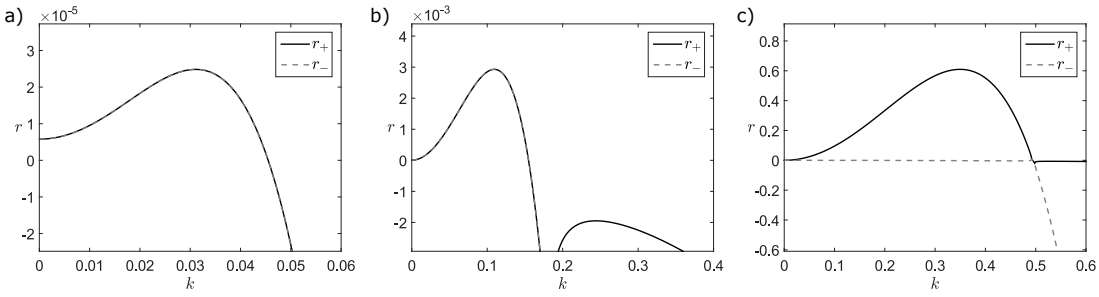

Figure 5.6: Growth rates r_+ and r_- versus the wavenumber k for $K \neq 0$. Oscillatory instability mode for a) $M_T = 10$ and b) $M_T = 100$. Monotonic instability mode for c) $M_T = 1000$.

inates as the concentration of component A increases and the perturbation that was initially promoted by the thermal Marangoni effect is reversed and evaporation process goes through an oscillatory instability mode, FIG 5.6a,b. However, for higher thermal Marangoni numbers the solutal Marangoni effect is not strong enough to reverse the initial perturbation. In this case the thermal Marangoni effect dominates, promoting the initial perturbation, and the evaporation process goes through a monotonic instability mode, FIG 5.6c.

The effect of the solutal Marangoni number on the instability is presented in FIG. 5.7. For lower solutal Marangoni numbers the thermal Marangoni effect dominates promoting the initial perturbation and the evaporation process goes through a monotonic instability mode for the most unstable wavenumber while the oscillatory mode is also unstable for longwave disturbances, see FIG. 5.7a. For higher solutal Marangoni numbers the solutal Marangoni effect dominates over the thermal Marangoni effect, reversing the initial perturbation, and the evaporation process goes through an oscillatory instability mode, FIG. 5.7b,c.

FIG. 5.8 presents the effect of volatility of the components on the instability. For $\alpha = 0.5$ the volatility of component A is higher, so it evaporates faster at the trough increasing the concentration of component B. As the component B has lower surface tension ($\delta = 0.276$) the surface tension at the trough is reduced and the solutal Marangoni effect drives the liquid away from the trough in direction to the crest that has higher concentration of component A, assisting the thermal

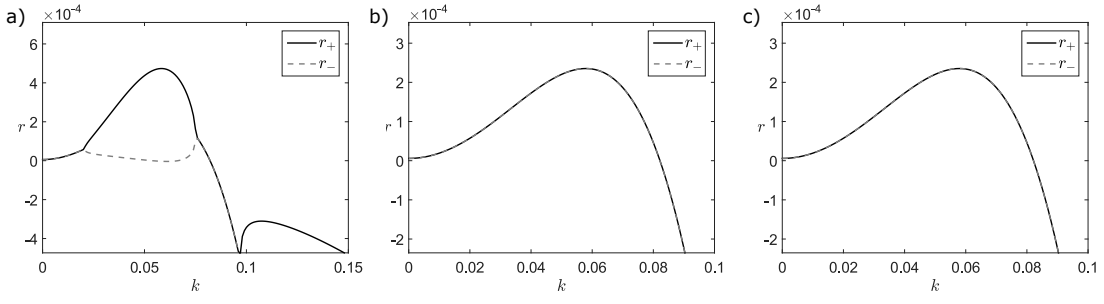

Figure 5.7: Growth rates r_+ and r_- versus the wavenumber k for $K \neq 0$. Monotonic instability mode for a) $M_c = 10$. Oscillatory instability mode for b) $M_c = 100$ and c) $M_c = 1000$.

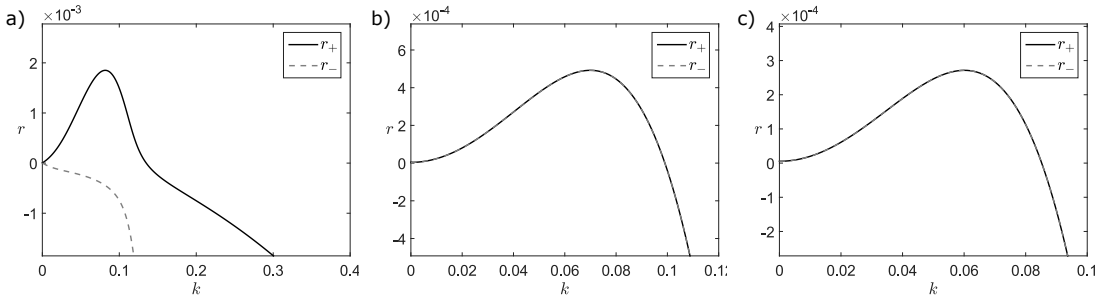

Figure 5.8: Growth rates r_+ and r_- versus the wavenumber k for $K \neq 0$. Monotonic instability mode for a) $\alpha = 0.5$. Oscillatory instability mode for b) $\alpha = 1$ and c) $\alpha = 2$.

Marangoni effect to promote the initial perturbation. In this case the evaporation process goes through a monotonic instability mode as shown in FIG. 5.8a. For $\alpha = 1$ both components has the same volatility, however, for the set of base parameters considered, the component B still have higher evaporation flux due to its dependence on the latent heat and molar weight. Therefore as for the case of $\alpha = 2$, where the component B is the most volatile, the component B will evaporate first, increasing the concentration of component A at the trough. This will increase the surface tension at the trough and the solutal Marangoni effect will lead to an oscillatory instability mode, FIG. 5.8b,c.

FIG. 5.10 and 5.11 presents maps with the regions of monotonic and oscillatory instability modes in the parameter space of the volatility ratio, α, and the ratio of solutal and thermal Marangoni numbers, M_c/M_T, for different values of the evaporation number, E, and the latent heat ratio Λ, respectively. FIG. 5.9 shows the regions of the map with respect to the properties of the components. For $M_c/M_T > 0$ the component A has higher surface tension and the solutal Marangoni effect drives the liquid in the direction of regions with higher concentration of component A. For $M_c/M_T < 0$ the component B has higher surface tension and the solutal Marangoni effect drives the liquid in direction to regions with higher concentration of component B. For $M_c/M_T = 0$ both components have the same surface tension and the solutal Marangoni effect is absent in that case.

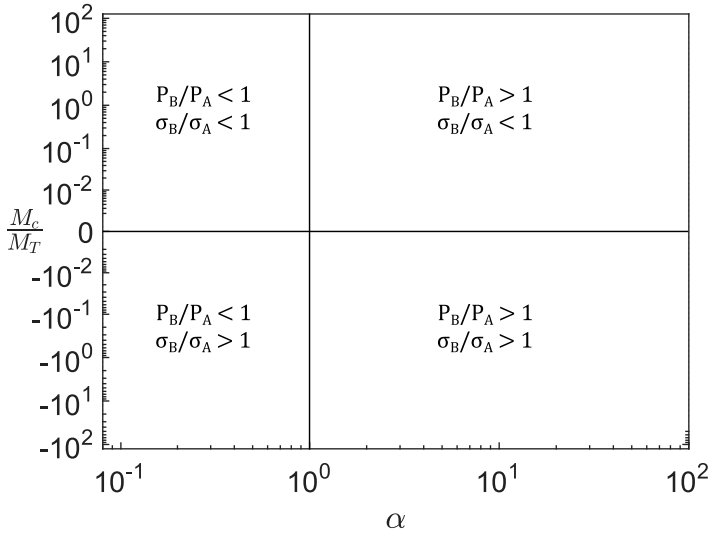

Figure 5.9: Regions of the map with respect to the volatility ratio and surface tension ratio in the parameter space of α versus M_c/M_T.

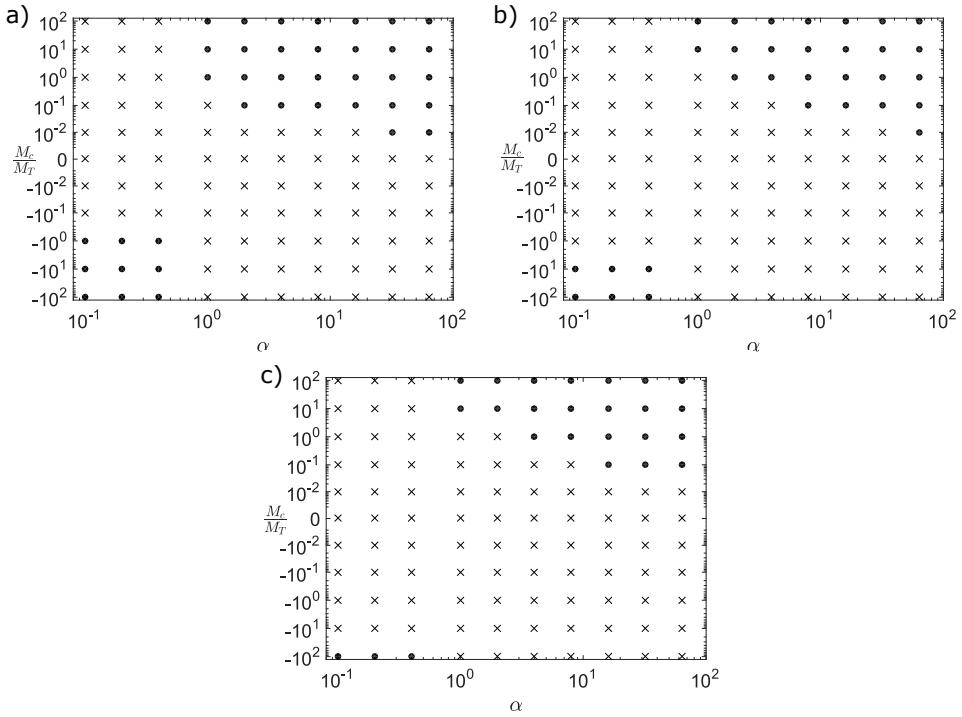

Figure 5.10: Map showing the regions of monotonic instability mode (crosses) and oscillatory instability mode (bullets) in the parameter space of α versus M_c/M_T for a) $E = 10^{-4}$, b) $E = 10^{-5}$ and c) $E = 10^{-6}$.

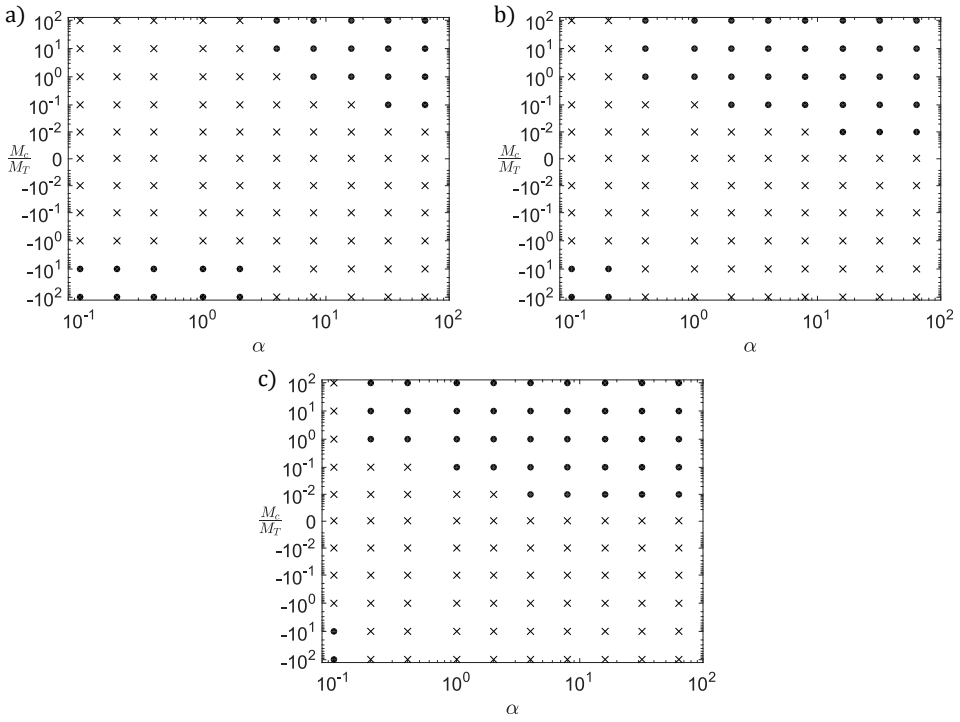

Figure 5.11: Map showing the regions of monotonic instability mode (crosses) and oscillatory instability mode (bullets) in the parameter space of α versus M_c/M_T for a) $\Lambda = 0.1$, b) $\Lambda = 1$ and c) $\Lambda = 2$.

In FIG. 5.10 it can be seen that for the case where the component A is less volatile, $\alpha > 1$, and has higher surface tension, $M_c/M_T > 0$, a smaller ratio between the solutal and thermal Marangoni numbers is needed to achieve the oscillatory instability mode as α increases. This is because the solutal Marangoni effect is proportional to how fast the lower surface tension component evaporates. Therefore increasing the volatility of the lower surface tension component requires a lower ratio between the solutal and thermal Marangoni number in order for the solutal Marangoni effect overcome the thermal Marangoni effect and lead the system to the oscillatory instability mode.

At the other end of the map, when the component B is the less volatile, $\alpha < 1$, and has higher surface tension, $M_c/M_T < 0$ the system also goes into an oscillatory instability mode as the ratio between the solutal and thermal Marangoni number become more negative. However, in that case it seems not to be affected by the volatility ratio, α, in the range of parameters investigated. In this figure it

also can be noted that as the evaporation number, E, decreases, the regions with the oscillatory instability mode are suppressed. This is because as the evaporation rate decreases it decreases the ratio of evaporation between the two components making the solutal Marangoni effect weaker, so a higher ratio between the solutal and thermal Marangoni number is needed to have an oscillatory instability mode.

FIG. 5.11 shows the effect of the latent heat ratio, Λ, on the different regimes of instability. In this figure it can be seen that the regions of oscillatory instability are shifted horizontally as the latent heat changes. This is because the evaporation flux of the components, eq. 5.24, is proportional to the vapour pressure, $\tilde{p}_i^o$, as well as the latent heat, $\tilde{L}_{v,i}$. Therefore as the latent heat ratio increases a lower volatility ratio is needed for the component B to evaporate faster than component A.

5.6 Linear regime: validation with numerics

The linear stability analysis is validated against the transient simulations presented in Section 5.7. The growth rates derived from the linear stability analysis and from the transient simulations are compared for the cases of monotonic instability mode and oscillatory instability mode. The growth rate of the initial perturbation in the transient simulations is calculated using the following expression for the monotonic and oscillatory case, respectively,

$$r_{mon} = \frac{\dot{A}}{A} \tag{5.135}$$

$$r_{osc} = \frac{\dot{A}_{max}}{A_{max}} \tag{5.136}$$

where in the monotonic case A is the amplitude of the instability and $\dot{A}$ is its time derivative, and in the oscillatory case A_{max} is the maximum amplitude of the oscillations and $\dot{A}_{max}$ is its time derivative.

First, we consider a case which exhibits a monotonic instability. In FIG.

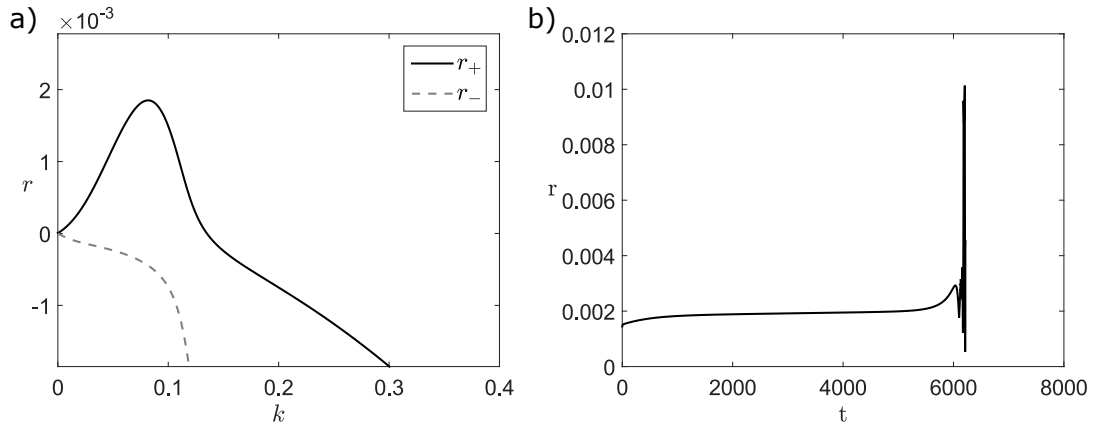

Figure 5.12: a) Growth rate versus the wavenumber derived from the linear stability analysis for the case of monotonic instability mode with $\alpha = 0.5$. b) Growth rate of the amplitude of the initial perturbation over time derived from the transient simulation.

5.12a we depict the dispersion curve where it is shown that the most unstable wavenumber is at $k = 0.082$ corresponding to a growth rate of $r = 1.85 \times 10^{-3}$. We perform a transient simulation for a domain with size that is equal to the wavelength of the most unstable mode and evaluate the growth rate in FIG. 5.12b. In the transient simulation the growth rate of the amplitude of the instability is approximately $r = 1.92 \times 10^{-3}$, showing a good agreement with the linear stability analysis.

In FIG. 5.13 the comparison of the growth rates for the oscillatory instability

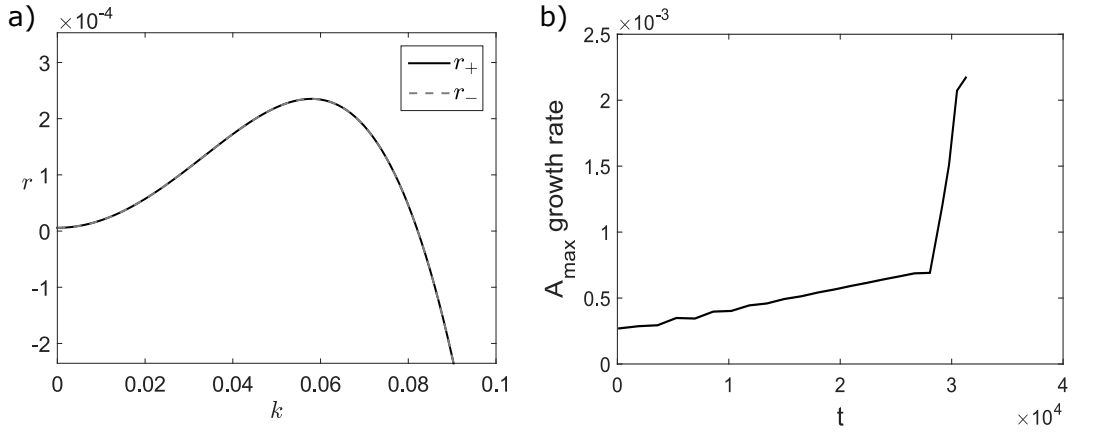

Figure 5.13: a) Growth rate versus the wavenumber derived from the linear stability analysis for the case of oscillatory instability mode with $\alpha = 2.28$. b) Growth rate of the maximum amplitude of the oscillations over time derived from the transient simulation.

mode is shown. In the linear stability analysis, FIG. 5.13a, the most unstable wavenumber is at $k = 0.058$ corresponding to a growth rate of $r = 2.35 \times 10^{-4}$. In the transient simulation, using a domain with size equal to the wavelength of the most unstable mode, the initial growth rate of the amplitude of the oscillations is $r = 2.7 \times 10^{-4}$, FIG. 5.13b, showing a good agreement with the linear stability analysis.

5.7 Non-linear regime: analysis and numerical results

The evolution of the system is solved numerically with a bespoke code using the finite element method. The weak formulation of the equations is presented in Appendix B. The computational domain is discretized in space using 100 elements and the solution is advanced in time using the implicit Euler method. The resulting set of nonlinear algebraic equations are solved in each time step using the Newton-Raphson method. Convergence was achieved upon mesh refinement. The size of the domain comprises the interval $0 < X < \pi/k_M$, where k_M is the most unstable wave number. Periodic boundary conditions are applied on the lateral endings and we use the following initial condition,

$$h(X, 0) = 1 + 5 \times 10^{-7} Cos(k_M X) \tag{5.137}$$

The time evolution of the interface of a thin liquid layer composed of a binary mixture heated from below using the set of base parameters presented in Table 5.2 and $\alpha = 0.5$ (FIG. 5.12) is presented in FIG. 5.14. For this set of parameters the component A has higher volatility and higher surface tension than component B. Initially a small perturbation, $O(10^{-6})$, is applied and it grows exponentially as the interface evaporates. When the perturbation is applied the temperature of the interface at the trough becomes hotter and the perturbation is promoted

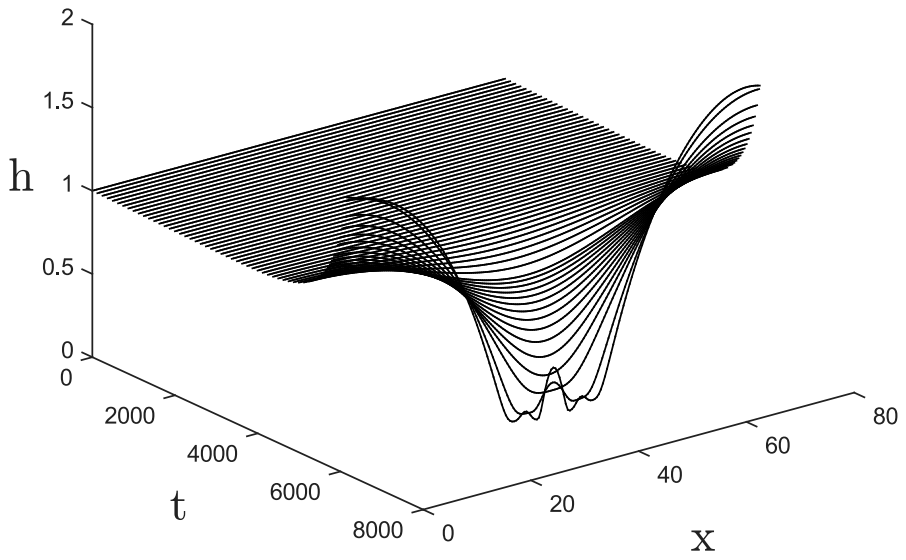

Figure 5.14: Time evolution of the interface for $\alpha = 0.5$ showing the monotonic instability mode.

by the vapour recoil at the trough, by the thermal Marangoni effect that drives the liquid away from the hotter trough, and by the solutal Marangoni effect due to the higher evaporation of component A at the trough that decreases the surface tension at that location. In this case the evaporation process presents a monotonic instability mode. The time taken for the rupture of the liquid layer was $t_R = 6.16 \times 10^3$.

FIG. 5.15 presents the time evolution of the interface for the set of base parameters present in Table 5.2 that corresponds to the oscillatory instability mode (FIG. 5.13). For this set of parameters the component A has lower volatility and higher surface tension than component B. In this case the initial perturbation, $O(10^{-6})$, is initially promoted by the vapour recoil and the thermal Marangoni effect due to the higher temperature at the trough. However, as the concentration of component A increases at the trough due to the higher volatility of component B, the solutal Marangoni effect become stronger and starts to drive the liquid

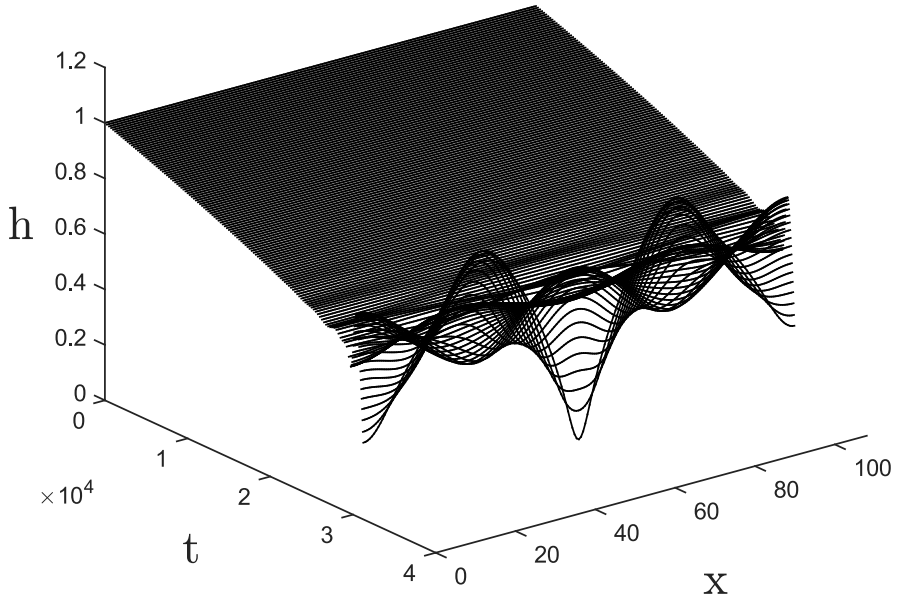

Figure 5.15: Time evolution of the interface for the parameters in Table 5.2 showing the oscillatory instability mode.

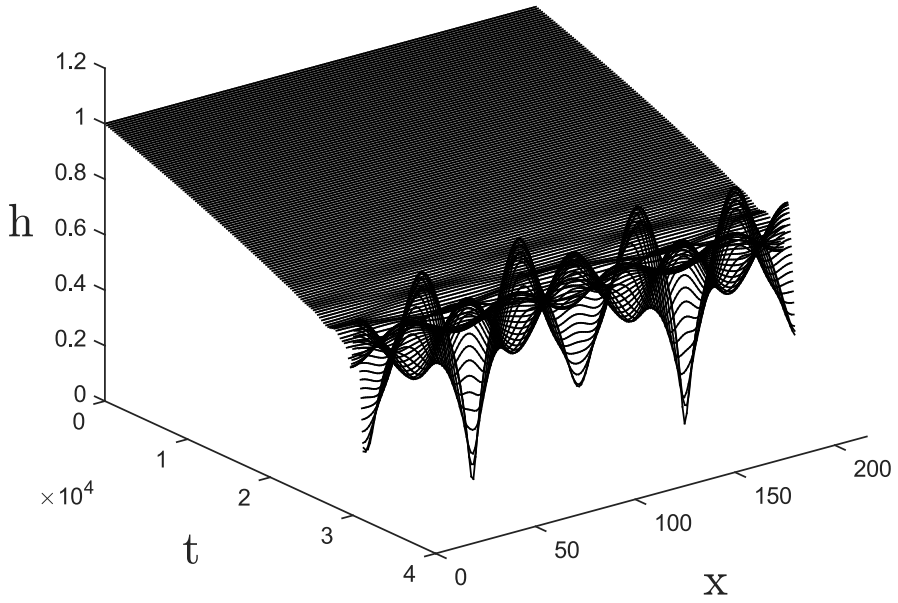

Figure 5.16: Time evolution of the interface for the parameters in Table 5.2 showing the oscillatory instability mode.

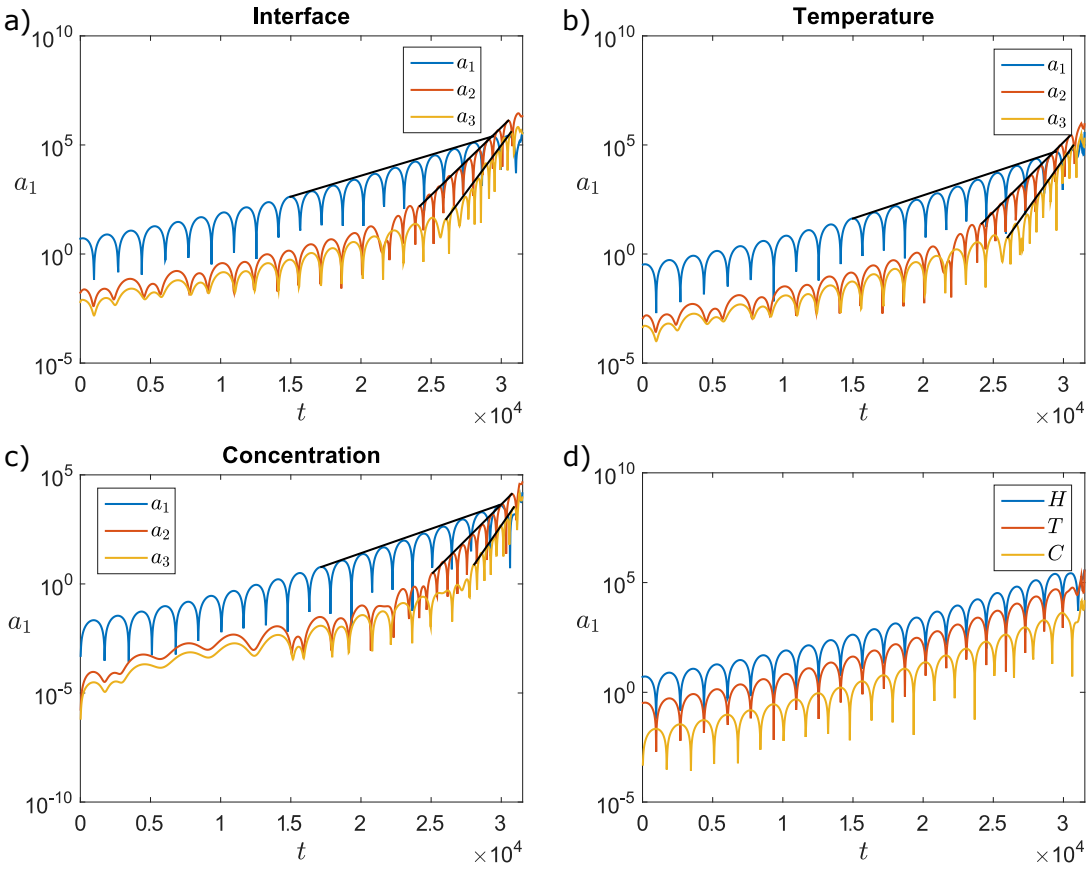

Figure 5.17: Modes of the Fourier transform of a) the interface ($s_1 = 2.21e-4$, $s_2 = 7.20e-4$, $s_3 = 9.92e-4$), b) the temperature ($s_1 = 2.44e-4$, $s_2 = 7.36e-4$, $s_3 = 1.04e-3$) and c) the concentration ($s_1 = 2.57e-4$, $s_2 = 7.40e-4$, $s_3 = 1.07e-3$). d) First mode of the Fourier transform of the interface (H), temperature (T) and concentration (C).

in the direction of the trough, reversing the amplitude of the initial perturbation. This process repeats at causing oscillations at the interface. The computed rupture time was $t_R = 3.15 \times 10^4$ that is much higher than in the monotonic case. In order to test the effect of the size of the domain, we consider this case with a double size domain, FIG. 5.16. The evolution of the interface presents the development of the same structures in both case showing no dependence on the size of the domain.

FIG. 5.17 shows the modes of the Fourier transform of the interface, temperature and concentration. Each subsequent mode which appears has a higher slope than the previous one. The ratio between the slope of the modes for the interface

deformation are $s_2/s_1 = 3.23$ and $s_3/s_1 = 4.49$, for temperature are $s_2/s_1 = 3.01$ and $s_3/s_1 = 4.24$, and for concentration $s_2/s_1 = 2.88$ and $s_3/s_1 = 4.16$. In FIG. 5.17d it can be seen that the first mode of the interface and temperature are in phase, while the concentration is out of phase. It means that the temperature changes instantaneously with the interface, increasing when the interface bends down and decreasing when it bends up, while the concentration has a minimum/maximum value when the amplitude of the interface and temperature is zero and increase/decrease when the interface bends down/up and the temperature is hotter/colder. This means that as the interface is enriched by the most volatile component, evaporation ensures local cooling of the interface - thereby leading to the conclusion that the interfacial and thermal fluctuations are bound to the soluto-Marangoni instability.

5.8 Conclusions

The stability of the evaporation of an horizontal thin liquid layer which consist of a binary mixture of volatile liquids heated from below has been investigated by means of linear stability analysis and transient simulations. To that effect, long-wave approximation has been employed to derive the evolution equations for the free interface and the concentration of the components. The linear stability analysis has been validated by comparing the solution for the growth rate of the instabilities against the transient simulations.

Two modes of instabilities have been described by the linear theory, i.e. a monotonic instability mode and an oscillatory instability mode. By performing a parametric analysis it was possible to identify how these modes depend on the ratio between the thermal and solutal Marangoni number and on the volatility ratio. When the most volatile component has the lower surface tension the thermal and solutal Marangoni effect compete with each other. In this case, when the solutal Marangoni effect dominates the system presents an oscillatory intability mode,

while when the thermal Marangoni effect dominates the system presents a monotonic instability mode. On the other hand, when the most volatile component has the higher surface tension both the thermal and the solutal Marangoni effect assist each other promoting the initial perturbation and leading to a monotonic instability mode.

The last section of this chapter presents the evolution of the interface computed numerically for the monotonic and oscillatory instability mode. The monotonic case considered was the one where the thermal and solutal Maragoni effect assist each other to promote the initial perturbation. In this case, the time for the liquid layer reaches the rupture was lower when compared to the oscillatory case where the thermal and solutal Marangoni effect compete with each other. In the oscillatory case it was observed that the oscillations in the temperature field are in phase with the oscillations at the interface, while the oscillations in the concentration is out of phase due to the time that it takes for the evaporation of the components to change the concentration.

Chapter 6

Conclusions and Future Work

This chapter presents an overview of the main findings from the thesis and suggest a few directions for future work.

6.1 Conclusions

The motion of bubbles driven by thermocapillary flows in self-rewetting liquids and the instabilities in evaporating thin liquid layers composed of a binary mixture under the influence of thermocapillary and solutocapillary flow was investigated in this thesis.

A two-phase DNS model based on the Volume-of-Fluid method has been developed to examine the thermocapillary propulsion of bubbles in self-rewetting liquids inside a channel with constant flow rate and constant temperature gradient in the flow direction (Chapter 3). The dynamics of the bubbles has been investigated over a range of flowrates (represented by Reynolds number, Re) and temperature gradients (represented by capillary number, Ca). The thesis reveals for the first time, distinct bubble regimes under the range of parameters investigated. At high capillary numbers (low temperature gradients) the thermocapillary flow is not strong enough to overcome the inertial forces of the liquid flow and the bubble is carried away with the flow. At moderate capillary num-

bers (moderate temperature gradients) thermocapillary forces propel the bubble against the liquid flow sometimes followed by halting at the equilibrium position (typically in the right side of the surface tension minimum) for low Reynolds numbers, and by damped oscillations for high Reynolds numbers. As the capillary number decreases (temperature gradient increases) the bubble equilibrium position is shifted in direction to the surface tension minima and after a critical value the bubble starts to present sustained oscillations around its equilibrium position. The numerical results for the bubble equilibrium position and frequency of the sustained oscillations were compared against the theoretical prediction presented by Shanahan & Sefiane [2] showing good agreement.

An experimental apparatus has been designed to investigate the thermocapillary propulsion of bubbles in self-rewetting liquids (Chapter 4). To this end a horizontal circular channel with constant flow rate and a constant temperature gradient along the flow direction was used. The motion of the bubbles was recorded by a CCD camera from the top and the temperature along the channel wall was captured by an infrared camera from the side. Different flow rates and temperature gradients were used and the counter-current propulsion of the bubbles was captured in the range of parameters investigated. During the counter-current motion the velocity of the bubbles presented a decreasing linear relationship with the flow rate due to the increase of the inertial force of the liquid flow, and a increasing linear relationship with the temperature gradient due to the increase the the thermocapillay flow propelling the bubble.

The last part of this thesis has been devoted to the study of instabilities in a evaporating horizontal thin liquid layer consisting of a binary mixture of volatile liquids heated from below. This was analysed by means of linear stability analysis (for early time, linear growth) and transient simulations (for late time, non-linear growth) (Chapter 5). The growth rates calculated from the transient simulations were cross-validated against those obtained from linear stability analysis and were

in good agreement. A parametric study on the growth rate of the instabilities was performed. The analysis revealed two modes of instabilities: a monotonic instability mode and an oscillatory instability mode. It was found that the instability modes depend on the interplay between the thermocapillary and solutocapillary effects. The evaporation process presents the monotonic instability mode when the thermocapillary and solutocapillary forces promote each other driving the flow in the same direction or when the instability is simply dominated by the thermocapillary forces. In this mode, the perturbations simply grow, leading to the rupture of the liquid. The oscillatory instability mode occurs when the thermocapillary and solutocapillary forces compete with each other presenting a periodic dominance between the two forces. In this mode, the perturbations at the liquid interface oscillates, growing in amplitude and eventually leading to the rupture of the liquid layer. The evolution of the interface was investigated by means of transient simulations for each mode and the growth rate of the instabilities was compared against the linear theory showing a good agreement. The transient simulations also revealed that the interfacial and thermal fluctuations at the interface are enslaved to the concentration gradients (in turn, driven by evaporation).

6.2 Future Work

The numerical model developed to investigate the thermocapillary migration of bubbles presented in Chapter 3 considered only the case of saturated vapour bubbles in a liquid with constant concentration field. This model can be extended to include the effects of phase change and variable concentration field to investigated the effects of the solutocapillary effect on the bubble motion. Also, the DNS model assumes axisymmetry which may be valid for low Re. But bubble fluctuations and behaviour in reality are not axisymmetric and hence a full 3D simulation study is needed. Also - the assumption of axisymmetry restricts the

model to only cylindrical geometries such as micro-pipes. However chips used for cooling are configured as square or rectangular channels, thus a full 3D modelling approach is needed towards mapping the full 3D temperature, flow and concentration fields.

In the analytical model to study evaporation of thin liquid layers composed of binary mixtures presented in Chapter 5 we considered only mixtures with a linearly decreasing relation of surface tension on temperature. This model can be modified to investigate the case of mixtures with a parabolic dependence of surface tension on temperature.

Appendix A

Linear stability analysis

Here we derive some expressions in terms of h and C used in Section 5.4. From eq. 5.99, the temperature is given by,

$$T = 1 - \frac{\Lambda_2 Z}{\lambda K + \Lambda_2 h} \tag{A.1}$$

From eq. 5.96 and 5.97, the evaporation fluxes reads,

$$J_A = \frac{\lambda C}{\lambda K + \Lambda_2 h} \tag{A.2}$$

$$J_B = \frac{\lambda (1 - C) \alpha \beta^{\frac{3}{2}} \Lambda}{\lambda K + \Lambda_2 h} \tag{A.3}$$

$$J = \frac{\lambda \Lambda_1}{\lambda K + \Lambda_2 h} \tag{A.4}$$

From eq. 5.98 surface tension and its derivatives takes the form,

$$\sigma = \delta + (1 - \delta) C - \Gamma_A (\delta \Gamma + (1 - \delta \Gamma) C) \left(1 - \frac{\Lambda_2 h}{\lambda K + \Lambda_2 h} \right) \tag{A.5}$$

$$\sigma_x = (1-\delta) C_x - \Gamma_A (1-\delta\Gamma) C_x \left(1 - \frac{\Lambda_2 h}{\lambda K + \Lambda_2 h} \right) + \Gamma_A (\delta\Gamma + (1-\delta\Gamma) C) \left(\frac{\lambda K (\Lambda_{2,x} h + \Lambda_2 h_x)}{(\lambda K + \Lambda_2 h)^2} \right) \tag{A.6}$$

$$\sigma_Z = 0 \tag{A.7}$$

From eq. 5.92 the pressure and its derivative reads,

$$p = p_v + \frac{E^2}{D} \left(\frac{\lambda \Lambda_1}{\lambda K + \Lambda_2 h} \right)^2 - \frac{\delta h_{xx}}{Ca} - \frac{\mathcal{A}}{h^3} \tag{A.8}$$

$$p_x = \frac{2\lambda^2 E^2}{D}\left[\frac{\Lambda_1\Lambda_{1,x}}{(\lambda K+\Lambda_2 h)^2} - \frac{\Lambda_1^2}{(\lambda K+\Lambda_2 h)^3}(\Lambda_{2,x}h+\Lambda_2 h_x)\right] - \frac{\delta h_{xxx}}{Ca} + \frac{3\mathcal{A}h_x}{h^4} \tag{A.9}$$

Appendix B

Weak formulation

Here the finite element method weak formulation is derived. First the Karman-Pohlhausen approximation is applied to eqs. 5.85-5.89. From mass balance, momentum, energy and concentration equation we get,

$$h_t = -EJ - \frac{\partial f}{\partial x} \tag{B.1}$$

$$hp_x - (\mu U_z)|_0^h = 0 \tag{B.2}$$

$$C_t + \frac{f}{h}C_x = \frac{1}{hPe}(hC_x)_x + \frac{E}{h}(CJ - J_A) \tag{B.3}$$

Next we derive the weak formulation. For the continuity equation we have,

$$\int \left[h_t + EJ + \frac{\partial f}{\partial x}\right]\phi_i dx = 0 \tag{B.4}$$

$$\int \left[(h_t + EJ)\phi_i - f\frac{\partial \phi_i}{\partial x}\right]dx + [f\phi_i]_0^{L_o} = 0 \tag{B.5}$$

For the normal stress balance we have,

$$\int \left[\left(p - p_v - \frac{E^2J^2}{D} + \frac{\mathcal{A}}{h^3}\right)\frac{Ca}{\sigma}\phi_i - h_x\frac{\partial \phi_i}{\partial x}\right]dx + [h_x\phi_i]_0^{L_o} = 0 \tag{B.6}$$

For the momentum equation we have,

$$\int \left[hp_x - (\mu U_z)|_0^h\right]\phi_i dx = 0 \tag{B.7}$$

For the evaporative flux we have,

$$\int [KJ_A - CT]\phi_i dx = 0 \tag{B.8}$$

$$\int [KJ_B - (1-C)\alpha\beta^{3/2}\Lambda T]\phi_i dx = 0 \tag{B.9}$$

For the concentration equation we have,

$$\int \left[C_t + \frac{f}{h}C_x - \frac{1}{hPe}(hC_x)_x - \frac{E^*}{h}(CJ - J_A)\right]\phi_i dx = 0 \tag{B.10}$$

$$\int \left[(hC_t + fC_x - E(CJ - J_A))\phi_i + \frac{1}{Pe}hC_x\frac{\partial\phi_i}{\partial x}\right]dx - \frac{1}{Pe}[hC_x\phi_i]_0^{L_o} = 0 \tag{B.11}$$

The temperature reads,

$$T = T_W - (J_A + \Lambda J_B)\frac{z}{\lambda} \tag{B.12}$$

The velocity is given by,

$$u = \frac{p_x}{\mu}\left(\frac{z^2}{2} - hz\right) + \frac{\sigma_x}{\mu Ca}z \tag{B.13}$$

The mass flux $f = \int_0^h u dz$ reads,

$$f = -\frac{p_x h^3}{3\mu} + \frac{\sigma_x h^2}{2\mu Ca} \tag{B.14}$$

Bibliography

[1] N. O. Young, J. S. Goldstein, and M. J. Block. The motion of bubbles in a temperature gradient. *Journal of Fluid Mechanics*, 6:350–356, 1959.

[2] M. E. R. Shanahan and K. Sefiane. Recalcitrant bubbles. *Scientific Reports*, 4(1):4727, 2014.

[3] C. Ma and D. Bothe. Direct numerical simulation of thermocapillary flow based on the Volume of Fluid method. *International Journal of Multiphase Flow*, 37(9):1045–1058, 2011.

[4] S. Nas and G. Tryggvason. Thermocapillary interaction of two bubbles or drops. *International Journal of Multiphase Flow*, 29(7):1117–1135, 2003.

[5] L. E. Scriven and C. V. Sternling. The marangoni effects. *Nature*, 187:186–188, July 1960.

[6] Dario Bogojevic. *Flow Boiling and Two-Phase Flow Instabilities in Silicon Microchannel Heat Sinks for Microsystems Cooling*. PhD thesis, The University of Edinburgh.

[7] Y. Abe, A. Iwasaki, and K. Tanaka. Microgravity experiments on phase change of self-rewetting fluids. In *Annals of the New York Academy of Sciences*, volume 1027, pages 269–285, 2004.

[8] Steven J. Weinstein and Kenneth J. Ruschak. Coating flows. *Annual Review of Fluid Mechanics*, 36(1):29–53, 2004.

[9] S. D. Howison, J. A. Moriarty, J. R. Ockendon, E. L. Terrill, and S. K. Wilson. A mathematical model for drying paint layers. *Journal of Engineering Mathematics*, 32(4):377–394, Nov 1997.

[10] H.A. Stone, A.D. Stroock, and A. Ajdari. Engineering flows in small devices: Microfluidics toward a lab-on-a-chip. *Annual Review of Fluid Mechanics*, 36(1):381–411, 2004.

[11] Todd M. Squires and Stephen R. Quake. Microfluidics: Fluid physics at the nanoliter scale. *Rev. Mod. Phys.*, 77:977–1026, Oct 2005.

[12] James B. Grotberg. Respiratory fluid mechanics and transport processes. *Annual Review of Biomedical Engineering*, 3(1):421–457, 2001.

[13] Francois M Udaykumar HS N'dri N Tran-Son-Tay R Shyy, W. Moving boundaries in micro-scale biofluid dynamics. *Applied Mechanics Reviews*, 54(5):405–454, 2001.

[14] R. S. Subramanian, R. Balasubramaniam, and G. Wozniak. Fluid mechanics of bubbles and drops. *Physics of Fluids in Microgravity*, (ed. R. Monti):149–177, 2002.

[15] G. Wozniak. On the thermocapillary motion of droplets under reduced gravity. *Journal of colloid and interface science*, 141(1):1–9, 1990.

[16] B. Braun, C. Ikier, H. Klein, and D. Woermann. Thermocapillary migration of droplets in a binary mixture with miscibility gap during liquid/liquid phase separation under reduced gravity. *Journal of Colloid and Interface Science*, 159:515–516, 1993.

[17] R. Balasubramaniam, C. E. Lacy, G. Woniak, and R. S. Subramanian. Thermocapillary migration of bubbles and drops at moderate values of the Marangoni number in reduced gravity. *Physics of Fluids*, 8(4):872–880, 1996.

[18] P. H. Hadland, R. Balasubramaniam, G. Woniak, and R. S. Subramanian. Thermocapillary migration of bubbles and drops at moderate values of the Marangoni number in reduced gravity. *Experiments in Fluids*, pages 240–248, 1999.

[19] J. C. Xie, H. Lin, J. H. Han, X. Q. Dong, W. R. Hu, A. Hirata, and M. Sakurai. Experimental investigation on Marangoni drop migrations using drop shaft facility. *International Journal of Heat and Mass Transfer*, 41(14):2077–2081, 1998.

[20] J. C. Xie, H. Lin, P. Zhang, F. Liu, and W. R. Hu. Experimental investigation on thermocapillary drop migration at large Marangoni number in reduced gravity. *Journal of Colloid and Interface Science*, 285(2):737–743, 2005.

[21] Q. Kang, H. L. Cui, L. Hu, and L. Duan. On-board experimental study of bubble thermocapillary migration in a recoverable satellite. *Microgravity Science and Technology*, 20(2):67–71, 2008.

[22] M. Hähnel, V. Delitzsch, and H. Eckelmann. The motion of droplets in a vertical temperature gradient. *Physics of Fluids A*, 1(9):1460–1466, 1989.

[23] N. Rashidnia and R. Balasubramaniam. Thermocapillary migration of liquid droplets in a temperature gradient in a density matched system. *Experiments in Fluids*, 11(2-3):167–174, 1991.

[24] Y. S. Chen, Y. L. Lu, Y. M. Yang, and J. R. Maa. Surfactant effect on the motion of a droplet in thermocapillary migration. *Int. J. Multiphase Flow*, 23(2):325–335, 1997.

[25] Y. K. Bratukhin, K. G. Kostarev, A. Viviani, and A. L. Zuev. Experimental study of Marangoni bubble migration in normal gravity. *Experiments in Fluids*, 38(5):594–605, 2005.

[26] R. S. Subramanian. Slow migration of a gas bubble in a thermal gradient. *AIChE Journal*, 27(4):646–654, 1981.

[27] R. S. Subramanian. Thermocapillary migration of bubbles and drops. *Advances in Space Research*, (5):161–166, 1983.

[28] R. Balasubramaniam and An-Ti Chai. Thermocapillary migration of droplets: An exact solution for small marangoni numbers. *Journal of Colloid And Interface Science*, 119(2):531–538, 1987.

[29] N. Shankar and R. S. Subramanian. The Stokes motion of a gas bubble due to interfacial tension gradients at low to moderate Marangoni numbers. *Journal of Colloid And Interface Science*, 123(2):512–522, 1988.

[30] R. Balasubramaniam and R. S. Subramanian. Thermocapillary bubble migration - Thermal boundary layers for large Marangoni numbers. *International Journal of Multiphase Flow*, 22(3):593–612, 1996.

[31] R. Balasubramaniam and R. S. Subramanian. The migration of a drop in a uniform temperature gradient at large Marangoni numbers. *Physics of Fluids*, 12(2000):733, 2000.

[32] J. Szymczyk and J. Siekmann. Numerical calculation of the thermocapillary motion of a bubble under microgravity. *Chemical Engineering Communications*, 69(1):129–147, 1988.

[33] R. Balasubramaniam and J. E. Lavery. Numerical simulation of thermocapillary bubble migration under microgravity for large Reynolds and Marangoni numbers. *Numerical Heat Transfer; Part A: Applications*, 16(2):175–187, 1989.

[34] X. Ma, R. Balasubramaniam, and R. S. Subramanian. Numerical simulation of thermocapillary drop motion with internal circulation. *Numerical Heat Transfer; Part A: Applications*, 35(3):291–309, 1999.

[35] H. Haj-Hariri, Q. Shi, and A. Borhan. Thermocapillary motion of deformable drops at finite Reynolds and Marangoni numbers. *Physics of Fluids*, 9(4):845–855, 1997.

[36] S. Nas, M. Muradoglu, and G. Tryggvason. Pattern formation of drops in thermocapillary migration. *International Journal of Heat and Mass Transfer*, 49(13-14):2265–2276, 2006.

[37] Z. Yin, P. Gao, W. Hu, and L. Chang. Thermocapillary migration of non-deformable drops. *Physics of Fluids*, 20(8):1–21, 2008.

[38] Stéphane Popinet. An accurate adaptive solver for surface-tension-driven interfacial flows. *Journal of Computational Physics*, 228(16):5838–5866, 2009.

[39] G. Petre and M. A. Azouni. Experimental evidence for the minimum of surface tension with temperature at aqueous alcohol solution/air interfaces. *Journal of Colloid And Interface Science*, 98(1):261–263, 1984.

[40] W. R. McGillis and V. P. Carey. On the role of Maragoni effects on the critical heat flux for pool boiling of binary mixtures. *J Heat Transfer*, 118:103–109, 1996.

[41] S. Ahmed and V. P. Carey. Effects of surface orientation on the pool boiling heat transfer in water / 2-propanol mixtures. *Journal of Heat Transfer*, 121(February 1999):80–88, 1999.

[42] R. Savino, A. Cecere, and R. Di Paola. Surface tension-driven flow in wickless heat pipes with self-rewetting fluids. *International Journal of Heat and Fluid Flow*, 30(2):380–388, 2009.

[43] R. Savino, R. Di Paola, A. Cecere, and R. Fortezza. Self-rewetting heat transfer fluids and nanobrines for space heat pipes. *Acta Astronautica*, 67(9-10):1030–1037, 2010.

[44] Y. Hu, T. Liu, X. Li, and S. Wang. Heat transfer enhancement of micro oscillating heat pipes with self-rewetting fluid. *International Journal of Heat and Mass Transfer*, 70:496–503, 2014.

[45] Y. Hu, S. Zhang, X. Li, and S. Wang. Heat transfer enhancement of subcooled pool boiling with self-rewetting fluid. *International Journal of Heat and Mass Transfer*, 83(2015):64–68, 2015.

[46] R. Vochten, G. Petre, and R. Defay. Study of the heat of reversible adsorption at the air-solution interface. *Journal of Colloid and Interface Science*, 42(February):320–327, 1973.

[47] R. Vochten and G. Petre. Study of the heat of reversible adsorption at the air-solution interface. II. Experimental determination of the heat of reversible adsorption of some alcohols. *Journal of Colloid And Interface Science*, 42(2):320–327, 1973.

[48] G. Karapetsas, K. C. Sahu, K. Sefiane, and O. K. Matar. Thermocapillary-driven motion of a sessile drop: Effect of non-monotonic dependence of surface tension on temperature. *Langmuir*, 30(15):4310–4321, 2014.

[49] M. K. Tripathi, K. C. Sahu, G. Karapetsas, K. Sefiane, and O. K. Matar. Non-isothermal bubble rise: non-monotonic dependence of surface tension on temperature. *Journal of Fluid Mechanics*, 763(2015):82–108, 2015.

[50] Alexander Oron, Stephen H. Davis, and S. George Bankoff. Long-scale evolution of thin liquid films. *Rev. Mod. Phys.*, 69:931–980, Jul 1997.

[51] R. V. Craster and O. K. Matar. Dynamics and stability of thin liquid films. *Rev. Mod. Phys.*, 81:1131–1198, Aug 2009.

[52] H. Bénard. The cellular whirlpools in a liquid sheet transporting heat by convection in a permanent regime. *Annales de Chimie et de Physique*, 23:62–101, 1901.

[53] L. Rayleigh. On convection currents in a horizontal layer of fluid, when the higher temperature is on the under side. *Philosophical Magazine*, 32:529–546, 1916.

[54] J. R. A. Pearson. On convection cells induced by surface tension. *Journal of Fluid Mechanics*, 4(5):489–500, 1958.

[55] C. V. Sternling, L. E. Scriven, and C. V. Sternling. On cellular convection driven by surface-tension gradients: effects of mean surface tension and surface viscosity. *Journal of Fluid Mechanics*, 19(3):321–340, 1964.

[56] H. Jeffreys. The surface elevation in cellular convection. *The Quarterly Journal of Mechanics and Applied Mathematics*, 4(3):283–288, 1951.

[57] A. Sheludko. Thin liquid films. *Advances in Colloid and Interface Science*, 1(4):391 – 464, 1967.

[58] A. Vrij. Possible mechanism for the spontaneous rupture of thin, free liquid films. *Discuss. Faraday Soc.*, 42:23–33, 1966.

[59] Eli Ruckenstein and Rakesh K. Jain. Spontaneous rupture of thin liquid films. *J. Chem. Soc., Faraday Trans. 2*, 70:132–147, 1974.

[60] Gumerman Raymond, J. and M. Homsy George. The stability of radially bounded thin films. *Chemical Engineering Communications*, 2(1):27–36, 1975.

[61] Malcolm B Williams and Stephen H Davis. Nonlinear theory of film rupture. *Journal of Colloid and Interface Science*, 90(1):220 – 228, 1982.

[62] S. Davis. Rupture of thin liquid films. In Richard E. Meyer, editor, *Publications of the Mathematics Research Center, University of Wisconsin-Madison*, pages 291–302. Academic Press Inc, 12 1983.

[63] K. Hickman. Studies in high vacuum evaporation. part iii - surface behaviour in the pot-still. pages 1892–1902. Ind. Eng. Chem., 1952.

[64] Harvey J. Palmer. The hydrodynamic stability of rapidly evaporating liquids at reduced pressure. *Journal of Fluid Mechanics*, 75(3):487–511, 1976.

[65] J. P. Burelbach, S. G. Bankoff, and S. H. Davis. Nonlinear stability of evaporating/condensing liquid films. *Journal of Fluid Mechanics*, 195:463–494, 1988.

[66] D.A. Goussis and R.E. Kelly. On the thermocapillary instabilities in a liquid layer heated from below. *International Journal of Heat and Mass Transfer*, 33(10):2237 – 2245, 1990.

[67] D. Hatziavramidis. Stability of thin evaporating/condensing films in the presence of surfactants. *International Journal of Multiphase Flow*, 18(4):517 – 530, 1992.

[68] Krassimir D. Danov, Norbert Alleborn, Hans Raszillier, and Franz Durst. The stability of evaporating thin liquid films in the presence of surfactant. i. lubrication approximation and linear analysis. *Physics of Fluids*, 10(1):131–143, 1998.

[69] Oleg E. Shklyaev and Eliot Fried. Stability of an evaporating thin liquid film. *Journal of Fluid Mechanics*, 584:157–183, 2007.

[70] Stergios G. Yiantsios and Brian G. Higgins. A mechanism of marangoni instability in evaporating thin liquid films due to soluble surfactant. *Physics of Fluids*, 22(2):022102, 2010.

[71] Stefania K. Serpetsi and Stergios G. Yiantsios. Stability characteristics of solutocapillary marangoni motion in evaporating thin films. *Physics of Fluids*, 24(12):122104, 2012.

[72] Alexander B. Mikishev and Alexander A. Nepomnyashchy. Instabilities in evaporating liquid layer with insoluble surfactant. *Physics of Fluids*, 25(5):054109, 2013.

[73] Alexander Mikishev and Alexander A Nepomnyashchy. The influence of evaporation on long-wavelength instabilities in liquid layer with insoluble surfactant. *Fluid Dynamics Research*, 46(4):041420, 2014.

[74] John B Bell, Phillip Colella, and Harland M Glaz. A Second-Order Incompressible Projection Method for the Navier-Stokes Equations. *Journal of computational physics*, 283(85):257–283, 1989.

[75] C W Hirt and B. D. Nichols. Volume of fluid (VOF) method for the dynamics of free boundaries. *Journal of Computational Physics*, 39(1):201–225, 1981.

[76] J. U. Brackbill, D. B. Kothe, and C. Zemach. A continuum method for modeling surface tension. *Journal of Computational Physics*, 100(2):335–354, 1992.

[77] Marianne M. Francois, Sharen J. Cummins, Edward D. Dendy, Douglas B. Kothe, James M. Sicilian, and Matthew W. Williams. A balanced-force algorithm for continuous and sharp interfacial surface tension models within a volume tracking framework. *Journal of Computational Physics*, 213(1):141–173, mar 2006.

[78] Sharen J. Cummins, Marianne M. Francois, and Douglas B. Kothe. Estimating curvature from volume fractions. *Computers and Structures*, 83(6-7):425–434, 2005.

[79] Dimitrios Mamalis. *Phase change and complex phenomena in drops and bubbles of pure and binary fluids*. PhD thesis, The University of Edinburgh.

[80] Shen-Chun Wu, Tien-Ju Lee, Wei-Jhih Lin, and Yau-Ming Chen. Study of self-rewetting fluid applied to loop heat pipe with ptfe wick. *Applied Thermal Engineering*, 119:622 – 628, 2017.

[81] Y. Naresh, K. Shri Vignesh, and C. Balaji. Experimental investigations of the thermal performance of self-rewetting fluids in internally finned wickless heat pipes. *Experimental Thermal and Fluid Science*, 92:436 – 446, 2018.

[82] O. E. Jensen and J. B. Grotberg. The spreading of heat or soluble surfactant along a thin liquid film. *Physics of Fluids A: Fluid Dynamics*, 5(1):58–68, 1993.

[83] M.R.E. Warner, R.V. Craster, and O.K. Matar. Surface patterning via evaporation of ultrathin films containing nanoparticles. *Journal of Colloid and Interface Science*, 267(1):92 – 110, 2003.

[84] Matar O. K. Sefiane K. Craster, R. V. Pinning, retraction, and terracing of evaporating droplets containing nanoparticles. *Langmuir*, 25(6):3601–3609, 2009.